

High Energy Next Generation Electrode for Li-ion Batteries

Aysen Zerey

Department of Chemical and Biological Engineering

Faculty of Engineering

The University of Sheffield

Supervisor: Professor Serena A. Cussen
September 2023

Declaration

The thesis is submitted in consideration for the award of Doctor of Philosophy. It is believed to be completely original, except where references have been made.

Coronavirus pandemic impact statement

My PhD research began in October 2019, with lab work starting in January 2020. The UK government lockdown was announced in March 2020 and I could not access laboratory facilities for 5 months as a result of the lockdown. A second lockdown, beginning in November 2020, and a third lockdown in January 2021 both hindered my access to the laboratory. The return to laboratories was limited to meet social distancing rules. A backlog of training, as well as other PhD students who were close to their submission dates, resulted in further delays in accessing lab equipment and necessary training. My project is one that is heavily synthetically based so this had a significant effect on my progress. Despite this, I have produced some exciting results in my thesis and I established several collaborations with external partners to facilitate obtaining further results (e.g. total scattering and muon spectroscopy). The examiners should be aware of these delays during my PhD and the delay these have put on my publishing of my results.

Aysen Zerey

29/09/2023

wonderful to be true,		few experiments. Nothing is too laws of nature; and in such things
us uns experiment is	the best test of such consi	Michael Faraday
		,,,,,,,,,,,,,,,,,,,,,,,,,,,,,,,,,,,,,,,
		,

To my Dad and Mom...

Abstract

This thesis focuses on the synthesis and characterization of manganese based cation disordered rock salt cathodes for lithium-ion battery applications. Manganese based cation disordered rock salt cathodes are synthesized by mechanosynthesis and then structurally and electrochemically analysed. Chapter 1 provides a general overview of lithium-ion batteries and a detailed reading of their working principles and the cathode materials used. Chapter 2 presents detail the methods used to obtain and analyse the materials synthesized in this thesis, as well as the fundamental principles for understanding the main techniques used to investigate their properties. Chapter 3 focuses on the mechanochemical synthesis of Li₂MnO_{3-x}F_x, which involves the partial substitution of fluorine into oxygen. The mechanochemical synthesis of the Li₂MnO₃-_xF_x (x=0, 0.2, 0.8, 1, 1.2) compositions were examined, along with muon-spin spectroscopy. Chapter 4 focuses on Li₂MnO₂F cation disordered rock salt cathode. This includes the optimization of parameters such as ball milling duration and selection of starting materials to achieve the desired capacities, alongside comprehensive analysis of the structural, morphological, and electrochemical properties of the synthesized material. Also, it involved the careful selection of binder particle size and the optimization of electrode ratio to improving capacity and enhancing stability during cycling. Chapter 5 presents to demonstrate the mechanochemical synthesis of Li₂Mn₁₋ _yZr_yO₂F, doping the Zr-cation in place of some manganese. The crystal structure was studied by X-ray diffraction (XRD) prior to electrochemical analysis where coin cells were assembled and galvanostatic cycling performed. Chapter 6 gives a general overall conclusion and future work. **Chapter 7** includes the Appendix information.

Acknowledgements

First and foremost, I would like to thank my supervisor, Professor Serena A. Cussen for giving me this opportunity and for always believing in me, providing support within our group. It has been an exciting and unforgettable experience for me. Your knowledge, your experience and your advice always motivated me to complete this process. I am really thankful to have a supervisor like you. I am sure that the experiences you shared with us will enlighten my path for the rest of my life. I would also like to acknowledge Professor Eddie Cussen as the second supervisor of this thesis for always being supportive and understanding towards me.

I would like to thank all the academic and student members of the Cussen Group; it was a pleasure to work with you. I would like to express my eternal gratitude to Dr Samuel Booth for always answering my questions and providing scientific support during the three years. I would like to thank Dr Innes McClelland for Muon data processing and analysis. I would like to thank Dr Xiao Hua for PDF data processing. Thanks especially to Heather Grievson for the technical lab support and training during my PhD journey.

My sincere thanks to the Turkish Government for funding my PhD education. This journey would not have been possible without your support.

Finally, I would like to express my deepest gratitude to my family members. You know it has been a long journey and I could never have come this far without your support from day one. Thank you for believing in me and supporting me. Zeynep Sare'm, sen hep benim minnosumsun © And dear fiancé Burkycim, you will stay with me forever as the most precious memory of this journey.. Thank you for making everything better, love you.

Table of Contents

Abstra	act	V
Ackno	wledgements	.vi
Table	of Contents	vii
List of	Table	.х
List of	Figures	.xi
Abbre	viations	ίx
1	Introduction	1
1.1.	The need for Li-ion Batteries	2
1.2.	An operating Lithium-ion Battery	5
1.3.	Designing high energy density cathodes materials for Li-ion Battery	10
1.3.1.	Layered structure cathode materials for Li-ion Battery	11
1.3.2.	Spinel structure cathode materials for Li-ion Battery	12
1.3.3.	Olivine structure cathode materials for Li-ion Battery	12
1.4.	Development of Ni-rich cathode materials for Li-ion Battery	13
1.5.	Exploration of Lithium excess cathodes based on manganese	15
1.6.	Li migration in disordered rocksalt	18
1.7.	Synthetic approach to disordered rocksalt materials	20
1.7.1.	Solid-State synthesis	20
1.7.2.	Mechanosynthesis	20
1.8.	Main challenges facing wider uptake of disordered materials	22
1.8.1.	Oxygen based charge compensation mechanism for cation-disorder	ed
	rocksalt Li-ion cathodes	23
1.8.2.	Fluorination for cation-disordered rocksalt Li-ion cathodes	23
1.9.	Aims and objectives of this work	25
2	Experimental Methods	27
2.1.	Introduction	27
2.2.	Materials	27
2.3.	Synthetic Methodologies	27
2.3.1.	Solid State Synthesis	27

2.3.1.	1. Synthesis of Li ₂ MnO ₃ from Li ₂ CO ₃ and MnCO ₃ precursors	27
2.3.1.	2. Synthesis of Li ₂ MnO ₃ from Li ₂ CO ₃ and Mn ₂ O ₃ precursors	28
2.3.1.	3. Thermal decomposition of Mn (II)CO ₃ to Mn ₂ O ₃	28
2.3.2.	Mechanosynthesis	. 28
2.3.2.	1. Synthesis of Li₂MnO₃ via Mechanosynthesis	28
2.3.2.	2. Synthesis of Li ₂ MnO ₂ F via Mechanosynthesis- [one step]	29
2.3.2.	3. Synthesis of Li ₂ MnO ₂ F via Mechanosynthesis- [two step]	. 29
2.3.2.	4. Synthesis of Zr-doped Li ₂ MnO ₂ F via Mechanosynthesis- [one step]	29
2.3.2.	5. Synthesis of Zr-doped Li ₂ MnO ₂ F via Mechanosynthesis- [two step]	30
2.4.	Characterization Techniques	30
2.4.1.	Crystal structure characterizations	30
2.4.1.	Powder X-ray diffraction (PXRD)	30
2.4.1.	2. Rietveld Refinement	. 32
2.4.2.	Scanning Electron Microscopy (SEM)	. 32
2.4.3.	Energy dispersive X-ray spectroscopy (EDX)	33
2.4.4.	Pair distribution function (PDF)	33
2.4.5.	Muon spin relaxation spectroscopy	33
2.5.	Electrochemical Characterization	36
2.5.1.	Galvanostatic cycling with potential limitation (GCPL)	. 36
2.5.2.	Electrode Preparation	37
3	Manganese based cation-disordered rock salt cathode materials	via
	mechanochemical synthesis	. 40
3.1.	Introduction	40
3.2.	Result and Discussion.	. 41
3.2.1.	Mechanosynthesis of manganese-based cation-disordered rock	salt
	$Li_2MnO_{3-x}F_x$ (x=0, 0.2, 0.8, 1, 1.2) oxyfluoride cathodes for Li	-ion
	batteries	41
3.2.2.	Electrochemical performances of manganese-based cation-disordered r	ock:
	salt $Li_2MnO_{3-x}F_x$ (x=0, 0.2, 0.8, 1, 1.2) oxyfluoride cathodes for Li	-ion
	batteries prepared using a mechanochemical synthesis	47
3.2.3.	Local lithium diffusion studies on manganese-based cation disordered r	ock:
	salt $Li_2MnO_{3-x}F_x$ (x=0, 0.2, 0.8, 1, 1.2) oxyfluoride cathodes by muon s	spin
	spectroscopy	. 53
3.3.	Conclusion.	62

4	Optimising the synthesis and electrochemical performance of Li ₂ MnO	J ₂ ⊦
	cation disordered rock salt cathodes	64
4.1.	Introduction	. 64
4.2.	Result and Discussion	. 64
4.2.1.	Optimising ball milling time for Li ₂ MnO ₂ F synthesis	64
4.2.2.	Optimising starting materials for Li ₂ MnO ₂ F synthesis	.72
4.2.3.	Selecting binder particle size for Li ₂ MnO ₂ F cycling performance	.79
4.2.4.	Optimising carbon/binder/active material ratio for cycling performance	of
	Li ₂ MnO ₂ F	81
4.3.	Conclusion	.88
5	Targeting electrochemical stability through Zr-cation doping in Li ₂ MnO ₂ F	=
	(Li ₂ Mn _{1-y} Zr _y O ₂ F)	90
5.1.	Introduction	90
5.2.	Result and Discussion	90
5.2.1.	Synthesis of Zr-doped Li ₂ MnO ₂ F	90
5.2.2.	Electrochemical testing of $Li_2Mn_{1-y}Zr_yO_2F$ (y=0.03, 0.06, 0.10, 0.	15)
	cathodes	.93
5.2.3.	Optimising mechanochemical synthesis time for $\text{Li}_2\text{Mn}_{0.97}\text{Zr}_{0.03}\text{O}_2\text{F}$	97
5.2.4.	Optimising mechanochemical synthesis for $\text{Li}_2\text{Mn}_{1\text{-y}}\text{Zr}_y\text{O}_2\text{F}$ (y=0.03 a	and
	0.10)	102
5.3.	Conclusion1	107
6	Overall Conclusion and Future Work	109
7	References	112
8	Appendices 1	121

List of Tables

Table 3.1 Activation energies calculated over the thermally activated region using	the
Arrhenius equation from μ+-SR data using the dynamic Kubo-Toyabe function	for
Li ₂ MnO ₃ , Li ₂ MnO _{2.8} F _{0.2} , Li ₂ MnO _{2.2} F _{0.8} , Li ₂ MnO ₂ F, and Li ₂ MnO _{1.8} F _{1.2}	.60
Table 3.2 Diffusion coefficient calculated at 300 K from equation 3.3	.61

List of Figures

Figure 1.1 The comparison of energy densities (W h l ⁻¹) vs. energy density (W h kg ⁻¹) for Lead-acid, Ni-Cd, Ni-MH, and Li-ion battery
Figure 1.2 The demand for the Li-ion batteries market by 20304
Figure 1.3 Intercalation of lithium ions during a discharging and charging process in the Li-ion battery, where LiCoO ₂ is the cathode and graphite is the anode
Figure 1.4 The open circuit energy diagram for electrode within electrolyte9
Figure 1.5 The crystal structures of three lithium-insertion compounds exhibit layered (2D), spinel (3D), and olivine (1D) frameworks that allow for the mobility of Li ⁺ ions within them
Figure 1.6 The energy diagram of (a) LiCoO ₂ , (b) LiNiO ₂ and (c) LiMnO ₂ . The image is taken from the reference
Figure 1.7 The phase diagrams show the LiCoO ₂ , LiNiO ₂ , and LiMnO ₂ stoichiometrically composition. The dots on the diagram describe the corresponding materials, LiNi _{1-x-y} Co _x Mn _y O ₂
Figure 1.8 The comparison of price increases of Co, Ni, Mn elements over the years
Figure 1.9 General rock salt type lithium transition metal oxide crystal structure (a) cation disordered rock salt, (b) layered, (c) spinel-like, and (d) γ-LiFeO ₂ 17
Figure 1.10 Li ⁺ diffusion a) in the layered oxides, b) Li migration barrier in layered oxides, and c) in disordered rock salt
Figure 1.11 The different type of high-energy milling equipment a) ball mill, b) planetary mill, c) vibration mill, d) stirring ball mill, e) pin mill, f) rolling milling. Need permission
Figure 1.12 Visual representation of the degradation of Li-excess cation disordered rock salt cathodes
Figure 2.1 Bragg's law condition shown schematically. Based on Dinnebier and Billinge

Figure 2.2 A standard μ+-SR experiments where positive muons implant within a sample, before decaying to produce positrons
Figure 2.3 A schematic illustration of the GCPL experiment during charge/discharge cycling
Figure 2.4 A schematic illustration of the 2032-coin type cells during cel fabrication
Figure 3.1 XRD patterns of the product during solid-state heat treatment of Li ₂ MnO ₃ at 450 °C for 24 hours (red) and 48 hours (blue), alongside reference pattern for Li ₂ MnO ₃ (black) obtain from ICSD (collection code 239796)
Figure 3.2 XRD patterns of the product during solid-state heat treatment of Li ₂ MnO ₃ at 1000 °C for 24 hours (red) and 48 hours (blue), alongside reference pattern for Li ₂ MnO ₃ (black) obtain from ICSD (collection code 239796)
Figure 3.3 XRD patterns of the product during solid-state heat treatment of Li ₂ MnO ₃ obtained at 450 °C based on ball milling time: 120 minutes (red) and 100 minutes (black)
Figure 3.4 (a) XRD patterns of the product during mechanosynthesis of Li ₂ MnO ₃ (black), Li ₂ MnO _{2.8} F _{0.2} (red), Li ₂ MnO _{2.2} F _{0.8} (blue), Li ₂ MnO ₂ F (green), and Li ₂ MnO _{1.8} F _{1.2} (purple) at 750 rpm for 24 hours. (b) The extended region shows the peak shifting within 2θ range of 35° and 75°
Figure 3.5 The charge-discharge capacity (mAh g ⁻¹) vs. voltage (V) curves obtained from galvanostatic cycling over 50 cycles at room temperature of the Li ₂ MnO _{3-x} F ₅ pellets (active material: carbon black: PTFE in a 60:20:20) (a) Li ₂ MnO ₃ , (b) Li ₂ MnO _{2.8} F _{0.2} , (c) Li ₂ MnO _{2.2} F _{0.8} , (d) Li ₂ MnO ₂ F, and (e) Li ₂ MnO _{1.8} F _{1.2} . 2032-coin type cells were cycled between 2 – 4.8 V vs. Li/Li ⁺ at a rate of 1 C
Figure 3.6 The charge-discharge capacity (mAh g ⁻¹) and coulombic efficiency (%) vs cycle number obtained from galvanostatic cycling over 50 cycles at room temperature of the Li ₂ MnO _{3-x} F _x pellets (active material: carbon black: PTFE in a 60:20:20) (a) Li ₂ MnO ₃ , (b) Li ₂ MnO _{2.8} F _{0.2} , (c) Li ₂ MnO _{2.2} F _{0.8} , (d) Li ₂ MnO ₂ F, and (e) Li ₂ MnO _{1.8} F _{1.2} 2032-coin type cells were cycled between 2 – 4.8 V vs. Li/Li ⁺ at a rate of 1 C51

Figure 3.7 The differential capacity (mAh V ⁻¹) vs. voltage (V) graph obtained from
galvanostatic cycling only two cycles at room temperature of the Li ₂ MnO _{3-x} F _x pellets
(active material: carbon black: PTFE in a 60:20:20) (a) Li ₂ MnO ₃ , (b) Li ₂ MnO _{2.8} F _{0.2} , (c
$Li_2MnO_{2.2}F_{0.8}$, (d) Li_2MnO_2F , and (e) $Li_2MnO_{1.8}F_{1.2}$. 2032-coin type cells were cycled
between 2 – 4.8 V vs. Li/Li+ at a rate of 1 C52
Figure 3.8 Raw data for μ+-SR measurement at 300 K under zero field (black)
longitudinal fields of 10 G (blue), and 20 G (orange). The solid lines represent the
fitting of the data using the dynamic Kubo-Toyabe function for (a) Li ₂ MnO ₃ , (b
Li ₂ MnO _{2.8} F _{0.2} , (c) Li ₂ MnO _{2.2} F _{0.8} , (d) Li ₂ MnO ₂ F and (e) Li ₂ MnO _{1.8} F _{1.2}
Figure 3.9 Temperature dependence of (a) the field fluctuation rate (ν) and (b) the
local field distribution (Δ) obtained from fitting the μ^+ -SR data using the dynamic Kubo
Toyabe function for : Li ₂ MnO ₃ (black) and Li ₂ MnO _{2.8} F _{0.2} (red) measured from 200 K to
500 K, with increments of 20 K. Li ₂ MnO _{2.2} F _{0.8} (blue) measured from 100 K to 200 K
with increments of 20 K, and then from 200 K to 400 K, with increments of 10 K
Li ₂ MnO ₂ F (green) measured from 100 K to 500 K, with increment of 20 K. The
$Li_2MnO_{1.8}F_{1.2}$ (purple) measured from 100 K to 400 K, with an increment of 20
K57
Figure 3.10 Arrhenius plot of the field fluctuation value (ν) within the thermally
activated area displayed from μ^+ -SR data using the dynamic Kubo-Toyabe function
for: (a) Li ₂ MnO ₃ (black), (b) Li ₂ MnO _{2.8} F _{0.2} (red), (c) Li ₂ MnO _{2.2} F _{0.8} (blue), (d) Li ₂ MnO ₂ F _{0.8}
(green), and (e) Li ₂ MnO _{1.8} F _{1.2} (purple)59
Figure 4.1 a) XRD patterns of the product during mechanosynthesis of Li ₂ MnO ₂ F a
750 rpm for 18 hours (black), 24 hours (red), and 36 hours (green) b) The highlighted
region shows peak shifting66
Figure 4.2 The nitrogen adsorption and desorption isotherms of Li ₂ MnO ₂ F samples a
77 K on (a) LMOF-18h, and (b) LMOF-36h were measured67
Figure 4.3 (Left) Experimental and calculated atomic pair distribution function profile
G(r), for Li ₂ MnO ₂ F samples obtained at 750 rpm for 18 hours, 24 hours and 36 hours
The refinement was performed using a monoclinic (C2/m) structure to describe the
disordered rock salt phase. (Right) Highlighted low-r region of 1.5 – 6 Å

Figure 4.4 The charge-discharge capacity (mAh g-1) vs. voltage (V) curves obtained
from galvanostatic cycling over 100 cycles at room temperature of the $\text{Li}_2\text{MnO}_2\text{F}$
pellets (active material: carbon black: 350 μm PTFE in a 70:20:10) (a) 18 hours, (b)
24 hours, (c) 36 hours. 2032-coin type cells were cycled between 2 $-$ 4.8 V vs. Li/Li ⁺
at a rate of C/1069
Figure 4.5 Capacity (mAh g ⁻¹) and coulombic efficiency (%) vs. cycle number curves
obtained over 100 cycles at room temperature of $\text{Li}_2\text{MnO}_2\text{F}$ pellets (active material:
carbon black: 350 μm PTFE in a 70:20:10) (a) 18 hours, (b) 24 hours, (c) 36 hours.
2032-coin type cells were cycled between 2 – 4.8 V vs. Li/Li $^+$ at a rate of C/1070
Figure 4.6 The differential capacity (mAh V ⁻¹) vs. voltage (V) graph obtained from
galvanostatic cycling over 100 cycles at room temperature of the $\text{Li}_2\text{MnO}_2\text{F}$ pellets
(active material: carbon black: 350 μm PTFE in a 70:20:10) (a) 18 hours, (b) 24 hours,
(c) 36 hours. 2032-coin type cells were cycled between 2 – 4.8 V vs. Li/Li $^{\scriptscriptstyle +}$ at a rate of
C/1071
Figure 4.7 Reaction schematic for the mechanochemical synthesis of Li ₂ MnO ₂ F, (a)
where the precursors mixed in one step and ball milled at 750 rpm for 18h. (b) where
the transition metal oxide (red) and lithium (per)oxide (blue) precursor mixed at 750
rpm for 9 hours and the LiF precursor (black) added and mixed at 750 rpm for 9 hours.
The grey colour shape represents ZrO ₂ balls in ZrO ₂ ball milling media73
Figure 4.8 XRD patterns of the product during mechanosynthesis of Li ₂ MnO ₂ F at 750
rpm for one-step ball milling (18 hours) and two-step ball milling (9 hours +9 hours).
Sample "A" is prepared using Li_2O_2 , MnO and LiF, "A-18h" (black) refers one-step ball
milling and "A-9h+9h" (blue) refers two-step ball milling. Sample "B" is prepared using
Li_2O , Mn_2O_3 , and LiF , " B-18h " (red) refers one-step ball milling and " B-9h+9h " (green)
refers two-step ball milling74
Figure 4.9 The charge-discharge capacity (mAh g ⁻¹) vs. voltage (V) curves obtained
from galvanostatic cycling over 50 cycles at room temperature of the Li ₂ MnO ₂ F pellets
(active material: carbon black: PTFE in a 70:20:10) (a) (b) (c) (d). 2032-coin type cells
were cycled between 2 – 4.8 V vs. Li/Li ⁺ at a rate of C/1076

Figure 4.10 The charge-discharge capacity (mAh g-1) and coulombic efficiency (%)
vs. cycle number curves obtained from galvanostatic cycling over 50 cycles at room
temperature of the Li ₂ MnO ₂ F pellets (active material: carbon black: PTFE in a
70:20:10) (a) (b) (c) (d). 2032-coin type cells were cycled between $2-4.8\ V$ vs. Li/Li
at a rate of C/1077
Figure 4.11 The differential capacity (mAh V ⁻¹) vs. voltage (V) graph obtained from
galvanostatic cycling over 50 cycles at room temperature of the Li ₂ MnO ₂ F pellets
(active material: carbon black: PTFE in a 70:20:10) (a) (b) (c) (d). 2032-coin type cells
were cycled between 2 – 4.8 V vs. Li/Li+ at a rate of C/1078
Figure 4.12 The charge-discharge capacity (mAh g ⁻¹) and coulombic efficiency (%)
vs. cycle number curves from galvanostatic cycling over 70 cycles at room
temperature of Li ₂ MnO ₂ F pellets with different particle size PTFE (a) 35 µm PTFE (b)
350 μm PTFE (c) beads PTFE. 2032-coin type cells were cycled between 2-4.8 V vs
Li/Li ⁺ at a rate of C/1080
Figure 4.13 SEM images of Li ₂ MnO ₂ F electrode prepared using 35 μm PTFE (a) pre-
cycling, (b) post-cycling and 350 μm PTFE (c) pre-cycling (d) post-cycling81
Figure 4.14 The Li ₂ MnO ₂ F electrode sheets after calendering a calendering rol
pressure machine (a) the Li ₂ MnO ₂ F pellet prepared in a ratio of 80:10:10 (active
material: carbon black: PTFE), (b) the Li ₂ MnO ₂ F pellet prepared in a ratio of 60:20:20
(active material: carbon black: PTFE)81
Figure 4.15 (a) The charge-discharge capacity vs. voltage curves, (b) the specific
capacity and coulombic efficiency vs. cycle number, (c) the differential capacity vs.
voltage graph obtained from galvanostatic cycling over 5 cycles at room temperature
of the Li ₂ MnO ₂ F pellets (active material: carbon black: PTFE in a ratio of 80:10:10)
2032-coin type cells were cycled between 2 – 4.8 V vs. Li/Li+ at a rate of C/10

Figure 4.16 (a) Capacity vs. voltage curves, (b) the specific capacity and coulombic efficiency vs. cycle number, (c) the differential capacity vs. voltage graph obtained from galvanostatic cycling at room temperature of the Li₂MnO₂F pellets (active

between 2 – 4.8 V vs. Li/Li ⁺ at a rate of C/1085
Figure 4.17 For electrode preparation process, while active material and carbon black are mixed (a) for 20 minutes using a pestle and mortar, (b) at 300 rpm for 3 hours via the high-energy ball milling method. The black colour sphere represents carbon black. The green colour sphere represents active material. The grey colour sphere represents zirconia balls
Figure 4.18 (a) The charge-discharge capacity vs. voltage curves, (b) the specific capacity vs. cycle number, (c) the differential capacity vs. voltage graph obtained from galvanostatic cycling at room temperature of the Li ₂ MnO ₂ F pellets. (active material: carbon black: PTFE in a ratio of 70:20:10). 2032-coin type cells were cycled between 2 – 4.8 V vs. Li/Li ⁺ at a rate of C/10. The orange colour represents carbon milling methods, active material and carbon black are mixed at 300 rpm for 3 hours via the high-energy ball milling method. The grey colour represents active material and carbon black are mixed for 20 minutes using a pestle and mortar
Figure 5.1 XRD patterns of $Li_2Mn_{0.97}Zr_{0.03}O_2F$ (red), $Li_2Mn_{0.94}Zr_{0.06}O_2F$ (blue), $Li_2Mn_{0.90}Zr_{0.10}O_2F$ (black), and $Li_2Mn_{0.85}Zr_{0.15}O_2F$ (green) prepared by mechanochemical synthesis at 750 rpm for 18 hours
Figure 5.2 SEM images of (left) Li ₂ Mn _{0.94} Zr _{0.06} O ₂ F and (right) Li ₂ Mn _{0.85} Zr _{0.15} O ₂ F samples synthesised at 750 rpm for 18 hours via mechanosynthesis. The scale bar represents 500 nm
Figure 5.3 Elemental mapping images for Mn, Zr , O and F from SEM-EDX of $Li_2Mn_{0.94}Zr_{0.06}O_2F$ prepared by mechanosynthesis. The scale bar represents 5 μm 92
Figure 5.4 Capacity (mAh g ⁻¹) vs. voltage (V) curves from galvanostatic cycling over 50 cycles at room temperature between 2-4.8 V vs. Li/Li ⁺ at a C/10 rate of Li ₂ Mn ₁₋ $_{y}Zr_{y}O_{2}F$ electrodes (active material: carbon: PTFE, 60:20:20). (a) Li ₂ Mn _{0.97} Zr _{0.03} O ₂ F, (b) Li ₂ Mn _{0.94} Zr _{0.06} O ₂ F, (c) Li ₂ Mn _{0.90} Zr _{0.10} O ₂ F, and (d) Li ₂ Mn _{0.85} Zr _{0.15} O ₂ F

Figure 5.5 Capacity (mAh g ⁻¹) and coulombic efficiency (%) vs. cycle number curves obtained from galvanostatic cycling over 50 cycles at room temperature of the Li ₂ Mn ₁ -
_y Zr _y O ₂ F electrodes (active material: carbon black: PTFE in a 60:20:20). (a)
Li ₂ Mn _{0.97} Zr _{0.03} O ₂ F, (b) Li ₂ Mn _{0.94} Zr _{0.06} O ₂ F, (c) Li ₂ Mn _{0.90} Zr _{0.10} O ₂ F, and (d) Li ₂ Mn _{0.85} Zr _{0.15} -
O ₂ F. 2032-coin type cells were cycled between 2-4.8 V vs. Li/Li ⁺ at a rate of
C/1095
G, 10
Figure 5.6 The differential capacity (mAh V ⁻¹) vs. voltage (V) graph obtained from
galvanostatic cycling over 2 cycles at room temperature of the Li ₂ Mn _{1-y} Zr _y O ₂ F
electrodes (active material: carbon black: PTFE in a 60:20:20). (a) Li ₂ Mn _{0.97} Zr _{0.03} O ₂ F,
(b) $Li_2Mn_{0.94}Zr_{0.06}O_2F$, (c) $Li_2Mn_{0.90}Zr_{0.10}O_2F$, and (d) $Li_2Mn_{0.85}Zr_{0.15}O_2F$. 2032-coin type
cells were cycled between 2-4.8 V vs. Li/Li ⁺ at a rate of C/1096
Figure 5.7 The charge-discharge capacity (mAh g ⁻¹) and coulombic efficiency (%) vs.
cycle number curves obtained from galvanostatic cycling over 7 cycles at room
temperature of the Li ₂ Mn _{0.97} Zr _{0.03} O ₂ F electrodes (active material: carbon black: PTFE
in a 70:20:10). a) 12 hours, b) 18 hours, and c) 36 hours. 2032-coin type cells were
cycled between 2-4.8 V vs. Li/Li ⁺ at a rate of C/1099
Figure 5.8 The charge-discharge capacity (mAh g ⁻¹) and coulombic efficiency (%) vs.
cycle number curves obtained from galvanostatic cycling over 7 cycles at room
temperature of the $\text{Li}_2\text{Mn}_{0.97}\text{Zr}_{0.03}\text{O}_2\text{F}$ electrodes (active material: carbon black: PTFE
in a 70:20:10). a) 12 hours, b) 18 hours, and c) 36 hours. 2032-coin type cells were
cycled between 2-4.8 V vs. Li/Li ⁺ at a rate of C/10100
Figure 5.9 Differential capacity (mAh V ⁻¹) vs. voltage (V) obtained from galvanostatic
cycling over 5 cycles at room temperature of the Li ₂ Mn _{0.97} Zr _{0.03} O ₂ F electrodes (active
material: carbon black: PTFE in a 70:20:10)). a) 12 hours, b) 18 hours, and c) 36 hours.
2032-coin type cells were cycled between 2-4.8 V vs. Li/Li+ at a rate of
C/10
0/10
Figure 5.10 XRD patterns of the obtained during two-step mechanosynthesis of
Li ₂ Mn _{0.97} Zr _{0.03} O ₂ F at 750 rpm for 9h+9h (black) and 12h+12h (red)

Figure 5.11 XR	D pattern	of the	obtained	l during	two-step	mechan	osynthesis of
$Li_2Mn_{0.90}Zr_{0.10}O_2F_{0.10}$	= at	750 ı	rpm fo	r 9h+9	h (blad	ck) an	d 12h+12h
(red)							103
Figure 5.12 The	charge-dis	scharge	capacity	(mAh g ⁻¹) vs. volta	ge (V) cu	ırves obtained
from galvanostati	c cycling c	ver 10 c	cycles at re	oom temp	oerature o	f the Li ₂ N	1n _{0.97} Zr _{0.03} O ₂ F
(a) 9h+9h, (b) 1	2h+12h a	nd Li ₂ M	n _{0.90} Zr _{0.10}	O ₂ F (c)	9h+9h, (c	d) 12h+1	2h electrodes
(active material:	carbon bla	ck: PTF	E in a 70:	20:10)).	2032-coin	type cel	ls were cycled
between 2-4.8 V	vs. Li/Li⁺ a	t a rate (of C/10				104
Figure 5.13 The	charge-di	scharge	capacity	(mAh g	⁻¹) and co	ulombic	efficiency (%)
vs. cycle number	curves ol	otained	from galv	anostatio	c cycling o	over 10 c	ycles at room
temperature of th	ne Li ₂ Mn _{0.9}	₉₇ Zr _{0.03} C	0₂F (a) 9h	+9h, (b)	12h+12h	and Li ₂ N	1n _{0.90} Zr _{0.10} O ₂ F
(c) 9h+9h, (d) 12h	n+12h elec	ctrodes (active ma	iterial: ca	rbon blac	k: PTFE i	in a 70:20:10).
2032-coin type	cells we	re cycl	ed betwe	en 2-4.	.8 V vs.	Li/Li+	at a rate of
C/10							105
Figure 5.14 The	differentia	al capac	city (mAh	V ⁻¹) vs. v	voltage (V	/) graph	obtained from
galvanostatic cyc	ling over 1	10 cycle	s at room	tempera	ture of the	e Li ₂ Mn _{0.}	₉₇ Zr _{0.03} O ₂ F (a)
9h+9h, (b) 12h+1	2h and Li	2Mn _{0.90} Z	′r _{0.10} O ₂ F (c) 9h+9h	ı, (d) 12h+	-12h elec	trodes (active
material: carbon	black: P	TFE in	a 70:20:	10)). 20	32-coin ty	pe cells	were cycled
between 2-4.8 V	vs. Li/Li+ a	at a rate	of C/10				106

Abbreviations

CEI Cathode Electrolyte Interface

DRX Disordered Rocksalt Cathode

DMC Dimethyl Carbonate

EC Ethylene Carbonate

EDX Energy dispersive X-ray spectroscopy

EMC Ethylene Carbonate

FTIR Fourier Transform Infrared Spectroscopy

ICSD Inorganic Crystal Structure Database

LCO Lithium Cobalt Oxide

LF Longitudinal Field

LFP Lithium Iron Phosphate

LIB Lithium Ion Battery

NCA Lithium Nickel Cobalt Aluminium Oxide

NMC Lithium Nickel Manganese Cobalt Oxide

PDF Pair Distribution Function

PTFE Polytetrafluoroethylene

PXRD Powder X-ray Diffraction

RT Room Temperature

SEI Solid electrolyte interface

SEM Scanning Electron Microscopy

ZF Zero Field

Chapter 1: Introduction

"There's a way to it better find it."- Thomas A. Edison

The effects of climate change are becoming increasingly apparent through the repeated occurrences of extreme weather events. The Paris Agreement on Climate Change warns the world to reduce greenhouse gas emissions and take responsibility for the provision of clean energy [1]. Decarbonising transportation is recognised as one of the critical factors in reducing greenhouse gas emissions [2]. In the United Kingdom, 28% per cent of greenhouse gases emissions are caused by transportation [3]. Governments have started taking environmental measures to reduce greenhouse gas emissions caused by transport [4]. Traditional transportation systems have begun to shift ground from internal combustion engines to electric vehicles (EVs) [5]. Consequently, electrochemical energy storage systems, which supply portable power from small electronic devices to electric vehicles, have become an important part of modern energy systems worldwide. This growing market needs rechargeable batteries, which are non-expensive and possess high energy density because of the demand for intelligent devices, electric vehicles, and smart energy management. Before methods for improving energy density is discussed, a brief history of electrochemical energy storage devices is presented.

The first energy storage system was the Voltaic pile, which was discovered in 1799 by Alessandro Volta [6], and then the Daniell cell was developed in 1836 by John Frederic Daniell [7]. The lead-acid battery was created in 1859, the first rechargeable battery and most internal combustion engines vehicles still use this technology today [8]. By the 1900s, the zinc-carbon battery [9], nickel-cadmium battery [10] and nickel-metal hydrogen battery [11] were further developed. The zinc-carbon battery works as a

primary battery (i.e., is not rechargeable), while the nickel-cadmium (Ni-Cd) and nickel-metal hydrogen (Ni-MH) batteries are rechargeable. In 1976, M. Stanley Whittingham has started to work on lithium-ion based reversible battery systems and showed that Li^+ could be reversibly intercalated into a layered TiS_2 structure [12]. John B. Goodenough used a similar approach with layered-type $LiMO_2$ (M = Co, Ni, Mn) in 1980 [13]. After more investigation, in 1991, Sony commercialised the first rechargeable lithium-ion batteries. Since then, lithium-ion batteries (Li-ion) have been used and served humanity with increasing demand. Whittingham, Goodenough and Yoshino were also awarded the Nobel Prize in 2019 for their significant contributions to humanity and technology.

1.1. The need for Li-ion Batteries

Replacing fossil fuel-based power with renewable energy solutions to reduce greenhouse gas emissions is essential. In the last decade, Li-ion batteries have played an important role in. Since the commercialization of Li-ion batteries in 1991 for use in portable electronics, they have progressed to applications such as electric vehicles and grid energy storage sectors.

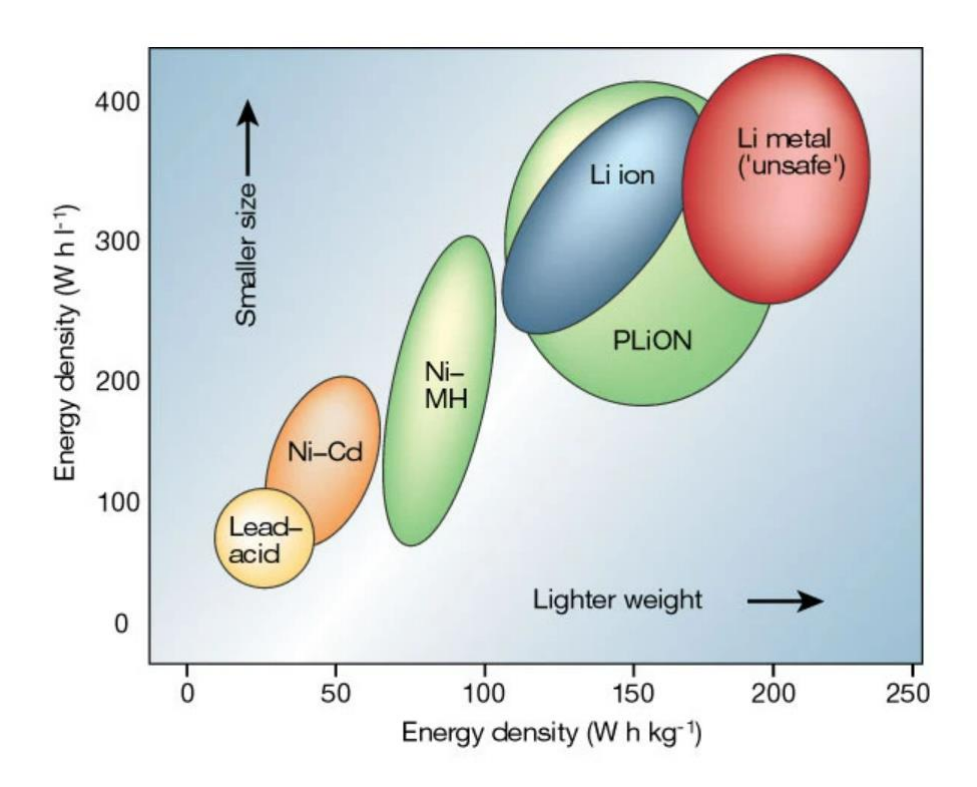


Figure 1.1 The comparison of energy densities (W h l⁻¹) vs. energy density (W h kg⁻¹) for Lead-acid, Ni-Cd, Ni-MH, and Li-ion battery [14].

Figure 1.1 displays a Ragone plot analysing various electrochemical energy storage methods, and it shows that Li-ion battery has higher energy densities (>150 Wh kg⁻¹ and >300 Wh I⁻¹) with smaller size and lighter weight. The higher volumetric (Wh I⁻¹) and gravimetric (Wh kg⁻¹) densities with small dimensions and low weight represent ideal properties for energy storage systems for transport. Rechargeable Li-ion batteries also provide enhanced, safety, reliability, and long life leading to the increased application in EVs [15]. Increasingly, Li-ion battery technology is finding applications in electrical vehicles. Figure 1.2 illustrates the Li-ion battery market's dramatic predicted growth by 2030 from 700 GWh to 4700 GWh due to the demand for electric vehicles and the development of a new market driven by fixed energy consumption. However, present technologies supply limited energy densities for longdistance applications in electric vehicles. Today's commercial Li-ion cathode materials are dominated by lithium transition metal oxides and phosphates such as LiCoO2, LiNi_{0.333}Co_{0.333}Mn_{0.333}O₂, LiMn₂O₄, and LiFePO₄. However, some of these materials are moving closer to their theoretical capacities [16]. Therefore, it is necessary to find more effective materials deliver high energy densities safely at an affordable cost.

Developing new cathode materials is of immediate interest as this plays a crucial role in determining the capacity and battery cost. For this reason, improving new families of positive electrode materials to enhance battery capacity and reduce fading is the most appropriate regarding the next-generation Li-ion batteries.

As a consequence, the cathode market requires high voltage (> 4 V) and/or high capacity (>200 mAh g⁻¹) to meet this demand. Among these materials, layered oxide materials including Li-rich Li_{1+x}M_{1-x}O₂ (*M* = Mn, Co, Ni, etc.) and Ni-rich LiNi_{1-x}M_xO₂ (*M* = Mn, Co, Al, etc.) are emerging as promising candidate cathodes. Recent studies have indicated that Li-excess cation disordered rock salt materials are also promising cathodes for future Li-ion battery technologies. Owing to their high energy density, non-expensive and environmentally friendly chemistries, Li-excess cation disordered rock salt materials are becoming increasingly important. Despite their advantages, these materials currently pose several challenges which must be solved for practical applications. These include challenges with synthesis, preventing severe capacity fade with repeated cycling and developing a better understanding of the role of disorder in these materials. This project seeks to address each of these points, through the targeted synthesis, electrochemical cycling and structural characterization of a series of disordered rock salts.

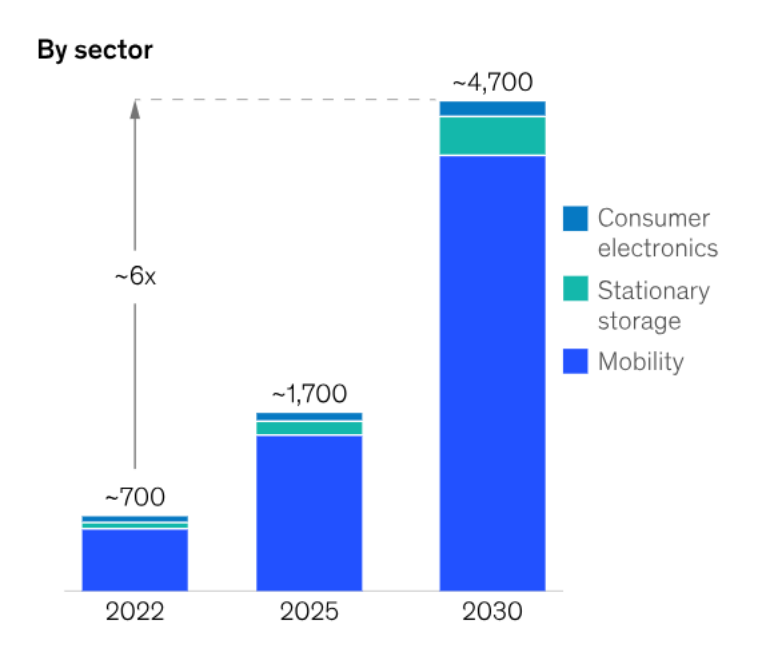


Figure 1.2 The demand for the Li-ion batteries market by 2030 [17].

1.2. An operating Lithium-ion Battery

Li-ion batteries were commercialized in 1991 by Sony and have grown to become the most common rechargeable battery in a growing battery market due to their lifetimes and energy densities. A Lithium-ion battery is a secondary battery based on ion insertion and extraction in the electrode during the charging and discharging processes. A typical Li-ion battery is made up of the cathode as a positive electrode, the anode as a negative electrode, and the electrolyte as a conductor. Moreover, in order to assemble a battery, separators, current collectors, and cell casing are additional components that are essential. The separator is situated between the cathode and anode to prohibit any short-circuit while simultaneously enabling the diffusion of Li ions into the electrolyte. The role of the current collector is to establish a connection between the electrodes and the external electrical circuit. In Li-ion batteries, an aluminium current collector is used on the cathode side while and a copper current collector is typically applied uses on the anode side.

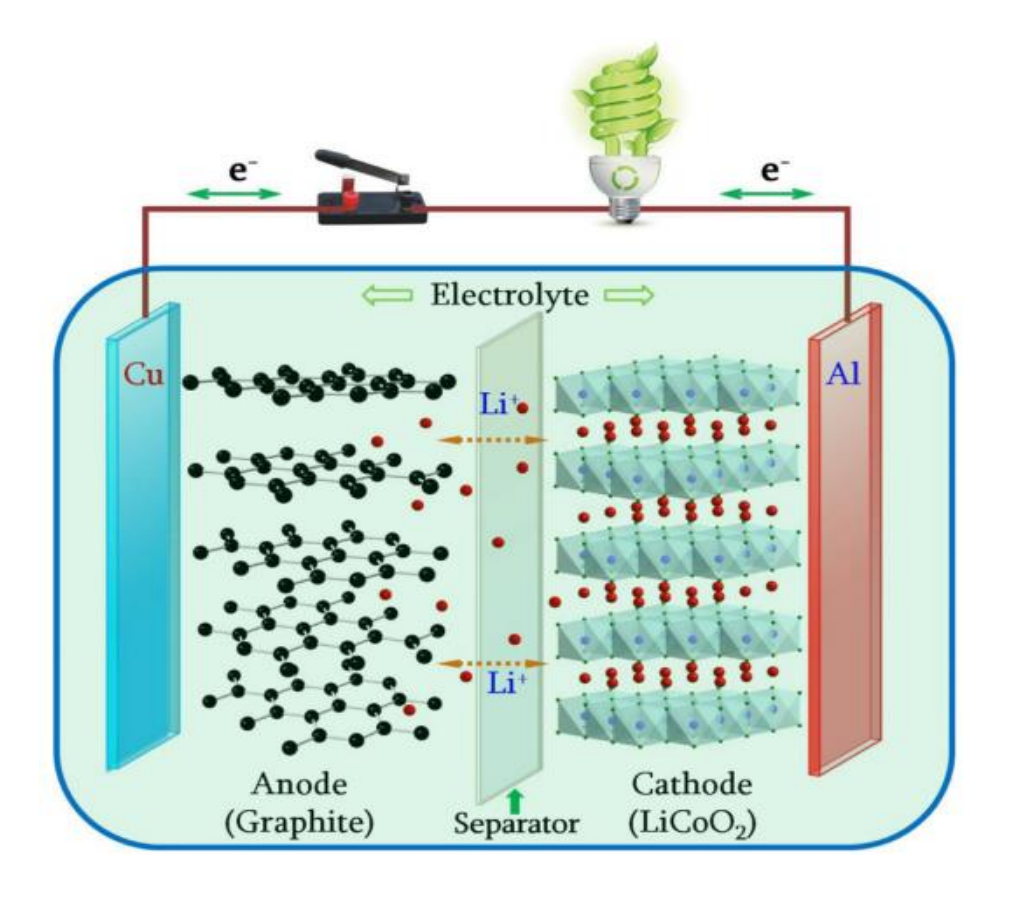


Figure 1.3 Intercalation of lithium ions during a discharging and charging process in the Li-ion battery, where LiCoO₂ is the cathode and graphite is the anode [18].

Generally, metal oxides are employed as cathodes and due to safety concerns with metallic lithium, which can be prone to dendrite formation, graphitic carbon is used as anode. Figure 1.3 exhibits the main mechanism during the discharging and charging process in the Li-ion battery [18]. In this figure, graphite is the anode and LiCoO₂ cathode side. During discharging process, the ions move from the anode side to the cathode side through a separator soaked with electrolyte (typically a lithium salt dissolved in an organic solvent, e.g., LiPF₆ in a dimethyl carbonate and ethylene carbonate mixture). At the same time, to preserve charge neutrality, an electron is released from the anode and flows through the external circuit where it provides a current. Upon charging the battery, the process is reversed, and the ions move from the cathode side to the anode side. The following equations (Eq.1.1-1.3) illustrate electrochemical reactions in a Li-ion battery during charge/discharge.

Cathode
$$LiCoO_2 \rightarrow Li_{1-x}CoO_2 + xLi^+ + xe^-$$
 (1.1)

Anode
$$xLi + xe^- + C_6 \rightarrow Li_xC_6$$
 (1.2)

Overall
$$LiCoO_2 + 6C \rightarrow Li_xC_6 + Li_{1-x}CoO_2$$
 (1.3)

One of the most famous examples of a cathode is the metal oxide LiCoO₂, which was investigated by Goodenough's group, who went on to be awarded the Nobel Prize in Chemistry in 2019 for this ground-breaking work [13]. It was suggested that Li⁺ could be extracted from LiCoO₂ via the Co^{3+/4+} redox couple at a voltage of ~4 V. However, the bottom of Co^{3+/4+} t_{2g} band overlaps with O²⁻:2p band, which causes the release of oxygen gas upon charging to high voltages. The release of oxygen from LiCoO₂ could react with the electrolyte and can lead to safety problems including thermal runaway. For this reason, the experimental capacity of LiCoO₂ is limited to ~140 mAh g⁻¹ (compared to its theoretical capacity, ~275 mAh g⁻¹) to avoid this band overlap and subsequent reactivity. Research into layered Li*M*O₂ oxides has continued, including the move to LiNi_xMn_yCo_zO₂, where a lower reliance on cobalt can reduce the cathode cost and the energy density can be tuned by the addition of Ni. However, challenges persist in the development of next-generation cathodes including overcoming poor

kinetics, cycle life, and reversibility. The investigation of new cathode materials continues with a focus on safety, cost, thermal stability, and high energy.

Energy density is a particularly crucial characteristic of batteries and is a measure of the amount of energy stored per unit volume or mass and is dependent on the specific capacity and voltage. The theoretical specific capacity can be obtained by Equation 1.4 with the unit of mAh g⁻¹, as follows:

$$Q_{theoretical} = \frac{nF}{M_w \times 3.6} \tag{1.4}$$

where n is the number of electrons exchanged during charge and discharge, F is the Faraday constant (96485 C mol⁻¹), M_w is the molecular weight of the electrode material, and 3.6 is the constant value which converts sA g⁻¹ to the more traditionally reported mAh g⁻¹. We can see immediately from this equation that in order to achieve high theoretical capacity either the molecular mass should be reduced or the number of exchanged electrons during charge and discharging should be increased.

$$V_{oc} = \frac{\mu_a - \mu_c}{e} \tag{1.5}$$

The cell voltage is another critical parameter for the operation of the cell, and it helps to determine the voltage area under correct and safe conditions. The cell voltage, V_{oc} , is determined by the difference in electrochemical potentials between the anode side (μ_a) and the cathode side (μ_c) , as shown below (in Equation 1.5), where e is the charge of an electron (1.6 x 10^{-19} C). This cell voltage is also governed by the electrochemical stability window of the electrolyte. For an ideal voltage window, the energy level of the electrolyte should be between the lowest unoccupied molecular orbital (LUMO) and the highest occupied molecular orbital (HOMO). Figure 1.4 displays the diagram of the energy level of the electrode and electrolyte under thermodynamically stable conditions. The electrolyte stability window (Eg) determines the stability boundaries.

The anode should be chosen so that its μ_a lies below the lowest unoccupied molecular orbital of the electrolyte to avoid reduction of the electrolyte at the anode. Conversely, the µc of the cathode should lie above the highest occupied molecular orbital of the electrolyte to prevent widespread oxidation of the electrolyte. During electrolyte reduction and oxidation, a layer called the solid electrolyte interphase (SEI) is formed on the surface of the anode or cathode. Lithium is the lightest metal and exhibits an extremely low electrode potential of -3.04 V vs. the standard hydrogen electrode with a high specific capacity (3.86 Ah g⁻¹). However, lithium metal also shows instabilities during charging, since the lowest unoccupied molecular orbital of the traditionally applied non-aqueous electrolytes lies below this electrochemical potential of Li+/Li which causes reactions at the interface SEI. This SEI can promote the growth of lithium dendrites which can cause short-circuiting and resulting safety issues, which means metallic lithium is not currently applied as an anode material. When graphite is applied as an anode in a commercialized battery, it shows that the SEI layer can be stabilized after the first cycle, and the SEI layer can prevent the disintegration of graphite. However, the SEI layer can also increase the internal battery resistance, and it can also reduce the cycling efficiency.

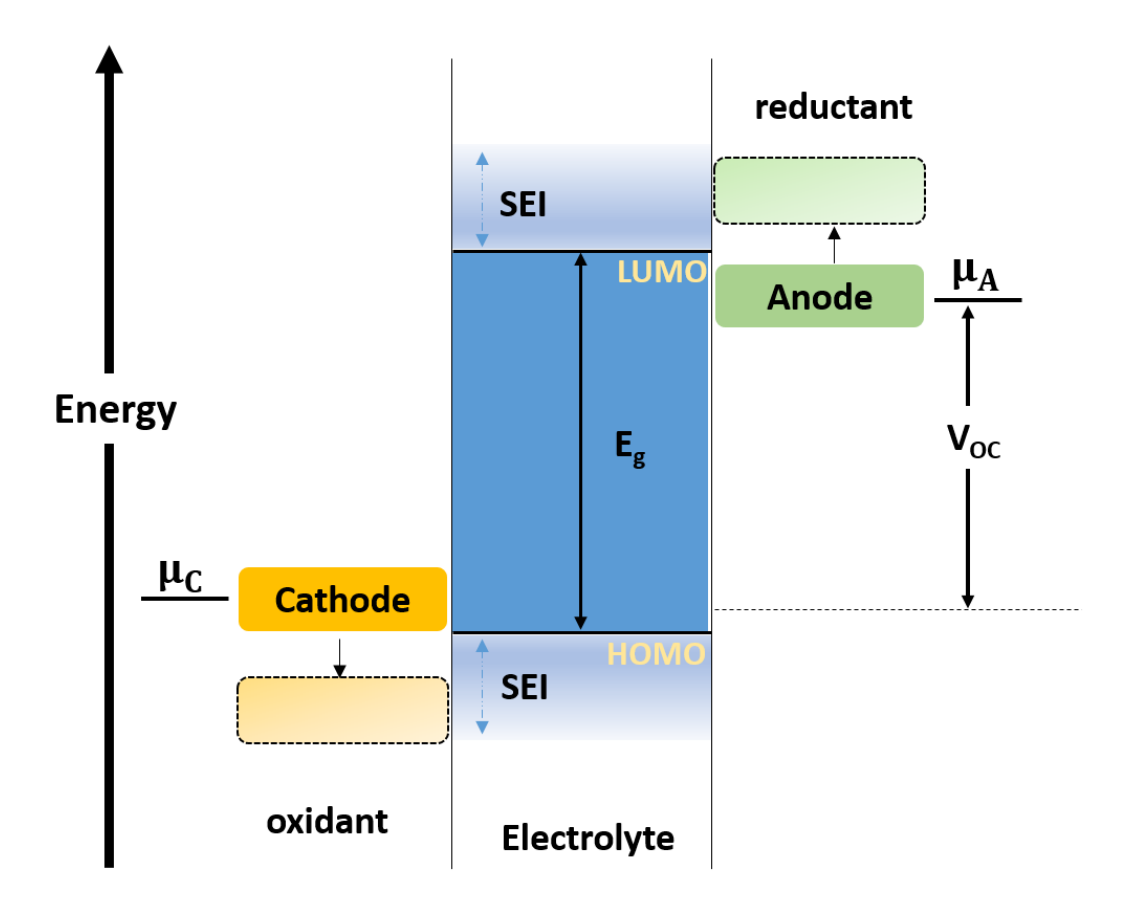


Figure 1.4 The open circuit energy diagram for electrode within electrolyte. Based on [19].

The choice of electrolyte also plays a role in the performance of these electrodes. Traditional organic liquid electrolytes provide excellent ionic conductivity, which is a crucial requirement for achieving rapid charging and extended battery lifetimes. However, they have a significant drawback in that they are highly flammable and electrolyte decomposition may result in the release of O₂ and CO₂, which can lead to thermal leaks, fires, and even explosions under mechanical, electrical, or thermal abuse conditions [20]. Therefore, much ongoing research is addressing the need for more stable and safer alternatives. One such example are solid-state electrolytes which offer enhanced thermal stability and improved durability compared to traditional organic liquid electrolytes. Unfortunately, many solid-state electrolytes still exhibit

lower ionic conductivity at room temperature when compared to their liquid counterparts and challenges remain in mass processing these solid alternatives. Currently, various inorganic solid-state electrolyte systems are undergoing in-depth investigation, including garnets and perovskite [21].

1.3. Designing high energy density cathodes materials for Li-ion Battery

To meet the increasing demand for high energy density Li-ion batteries, it is vital that the battery operates at higher voltages and while simultaneously providing high specific capacity. The most commonly applied anode material remains graphite (theoretical capacity of 372 mAh g⁻¹) because of its excellent reversibility in lithiation and delithiation reactions and its low lithiation potential [22]. When compared to the high capacity of the graphite anode currently in use, the cathode materials show lower capacities (~200 mAh g⁻¹). The lower capacity of cathodes poses a significant barrier to enhancing the energy density of Li-ion batteries. This is because cathode materials not only have a notable impact on the battery's voltage and power characteristics but also influence other important factors such as rate capability and cycle life, which are determined by their intrinsic chemistry. The ability to achieve high rates of charge and discharge is closely linked to the electronic and ionic conductivities exhibit by cathode materials. For instance, by substituting nickel for cobalt in the layered oxide material LiCoO₂, the specific capacity of the cathode increased from 140 mAh g⁻¹ to 200 mAh g⁻¹ [23]. Replacing cobalt with nickel allows for the reversible incorporation of more Li⁺, in contrast to LiCoO₂, where only 0.5 Li⁺ ion can be reversible, leading to capacity improvement. In addition to providing a route for improving energy densities, cathode materials play a crucial role in determining the cost of batteries. Currently, the cathode accounts for approximately 40-50% of the overall cost in Li-ion batteries [24]. The cost of the cathodes largely depends on the cost of raw materials. This aspect will be discussed in greater depth in the following section.

Insertion-type cathode materials are commonly preferred in Li-ion batteries due to the simplicity and reversibility of the insertion reaction. During the charge and discharge, the process of Li-ion insertion and extraction occurs in host structure. LiCoO₂, LiFePO₄, LiMn₂O₄, LiNi_{1/3}Mn_{1/3}Co_{1/3}O₂, and LiNi_{0.8}Co_{0.12}Al_{0.05}O₂ are among the commonly employed cathode materials in Li-ion batteries. There are already several high voltage cathode candidates available, such as the LiNi_{0.5}Mn_{1.5}O₄ spinel or the

LiNiPO₄ and LiCoPO₄ olivine phosphates among others. However, their application has been precluded by the lack of suitable high voltage stable liquid electrolytes. Some of these compounds will be discussed more details in next section. The cathode materials are broadly classified here according to crystal structure into layered, spinel, and olivine. Figure 1.5 displays the crystal structure of three lithium-insertion compounds exhibit layered (2D), spinel (3D) and olivine (1D) frameworks [25].

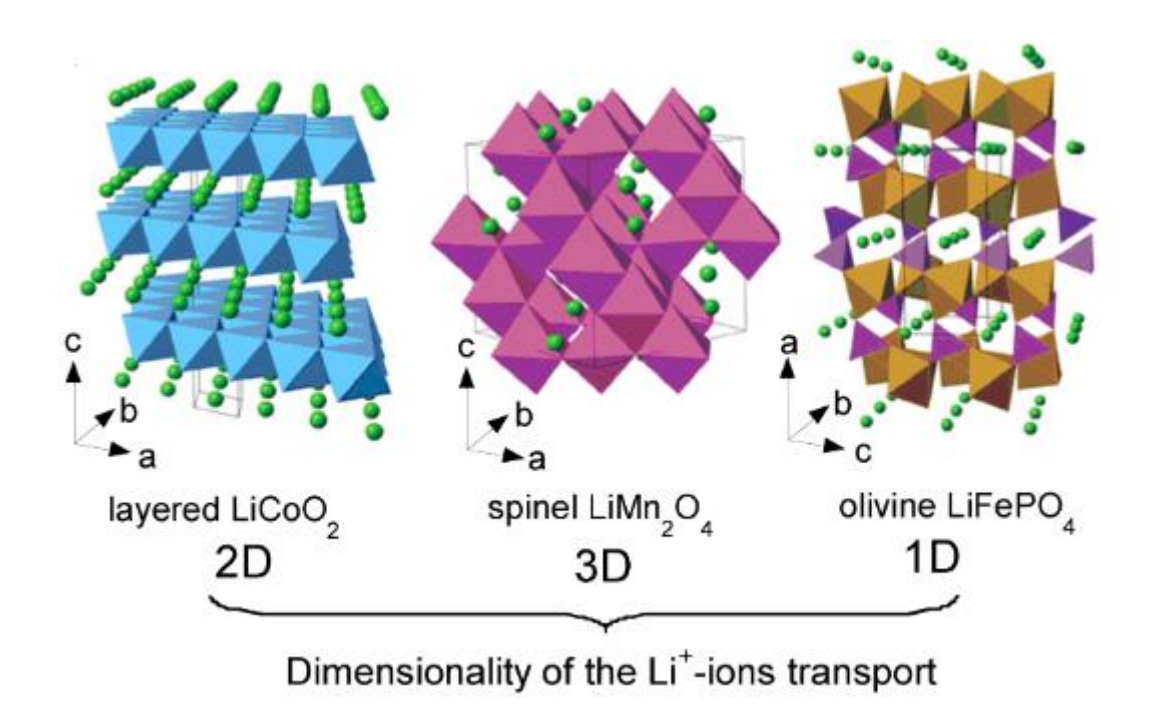


Figure 1.5 The crystal structures of three lithium-insertion compounds exhibit layered (2D), spinel (3D), and olivine (1D) frameworks that allow for the mobility of Li⁺ ions within them [25].

1.3.1. Layered Structure Cathode Materials for Li-ion Battery

Layered transition metal oxides are one of the commonly used cathode materials in Li-ion batteries. Transition metal oxides have a general Li*M*O₂ (M= Co, Ni) formula in a layered structure. LiCoO₂, developed by Goodenough, has a layered structure where Li⁺ and Co³⁺ ions are an ordered arrangement in the crystal structure with oxygen planes arranged in an ABCABC stacking pattern. The Li⁺ and Co³⁺ ions occupy octahedral sites, alternating between the oxygen sheets. The significant difference in

charge and size between these ions contributes to the observed cation ordering in LiCoO₂, which displays good electronic conductivity and intercalation reversibility with a high voltage of ~4 V. However, as previously mentioned the Co^{3+/4+} band overlap with O²⁻:2p band and resulting oxygen loss limits the workable capacity to 140 mAh g⁻¹. In addition to these limitations, the price of cobalt metal is high, it is a non-abundant element, and there are ethical concerns surrounding its mining practices. To help improve capacity and reduce cost, the substitution of manganese and nickel for cobalt presents an attractive option for layered oxide cathodes. The layered structure, LiNi_{1-x-y}Mn_xCo_yO₂ (NMC), has been regarded as a competitor to LiCoO₂ due to low cost derived by a reduced reliance on cobalt, with high capacities of ~ 200 mAh g⁻¹ offered for Ni-rich NMCs such as LiNi_{0.8}Mn_{0.1}Co_{0.1}O₂ (NMC811). In NMC111 where Ni, Mn, and Co exist in equal amounts, manganese acts as structural stabilizer without partaking in the cycling process. Nevertheless, the NMC cathodes, in particular the Ni-rich compositions, suffer from structural instability, solid electrolyte interface (SEI) formation, voltage fading, and safety problems [26].

1.3.2. Spinel Structure Cathode Materials for Li-ion Battery

The spinel structure cathodes, such as LiMn₂O₄, consists of a tightly packed arrangement of oxygen atoms with a Li[M₂] O₄ formula, where Li⁺ cations occupy the 8a tetrahedral sites and M cations occupy reside 16d octahedral sites. The spinel framework also possesses three-dimensional (3D) diffusion pathways through the voids present in the octahedral sites at 16c [27]. These cathodes, especially Mn-based, could present a safer and cheaper alternative but have lower capacities compared to LiCoO₂ (~110 mAh g⁻¹). During cycling, the Jahn-Teller distortion of Mn³⁺ ions lead to structural instability and capacity loss because of the dissolution of Mn ions. To solve these challenges, the Ni-substitution has been considered such as LiNi_{0.5}Mn_{1.5}O₄ which has been studied as a high voltage cathode [28].

1.3.3. Olivine Structure Cathode Materials for Li-ion Battery

The most well-known member of the olivine structure family is the LiFePO₄ cathode, which crystalises in the Pnma space group and represents a more inexpensive and non-toxic alternative to cobalt-based chemistries. It was discovered and used in 1997

by Goodenough and co-workers [29] and has a theoretical capacity of 170 mAh g⁻¹. The Li⁺ ions within LiFePO₄ can be extracted, leading to the formation of FePO₄. During charge and discharge, the movement of Li⁺ takes place via one-dimensional (1D) channels which leads to low Li⁺ ion diffusion. LiFePO₄ also suffers from low electronic conductivity. The LiNiPO₄ and LiCoPO₄ olivine phosphates have been investigated as alternatives to LiFePO₄. Nevertheless, their application has been impeded due to the lack of suitable high voltage stable liquid electrolytes.

1.4. Development of Ni-rich Cathode Materials for Li-ion Battery

As previously mentioned in sections 1.3. and 1.3.1., $LiCoO_2$ can extract only ~0.5 Li^+ ion per unit formula, with a specific capacity of 140 mAh g⁻¹. If 1 Li^+ ion was extracted per unit formula, it could provide 274 mAh g⁻¹ capacity. However, the $Co^{3+/4+}$ band and O^{2-} :2p band have overlapping energy levels, which the Co band is partially occupied, and the O band is fully occupied [30]. Figure 1.6 (a) displays the energy diagram of $LiCoO_2$ with highlighted the $Co^{3+/4+}$: t_{2g} and the O^{2-} :2p band.

During the charging process, the Li amount at the cathode decreases and the $Co^{3+/4+}$: t_{2g} band will lose electrons. If there are more than 0.5 Li⁺ ion per unit formula, the required electrons will be supplied from the overlapping region and the O^{2-} :2p band. Therefore, the oxidation of O species can occur by removing electrons from the O^{2-} :2p band, leading to the formation of O_2 gas. Another hazard associated with the formation of O_2 gas is that oxygen readily reacts with organic liquid electrolytes which can cause overheating problems. If this continues, the reaction rate will increase, reducing the amount of cathode and causing a decrease in capacity [31]. For these reasons, more sustainable alternatives to LiCoO₂ must be sought.

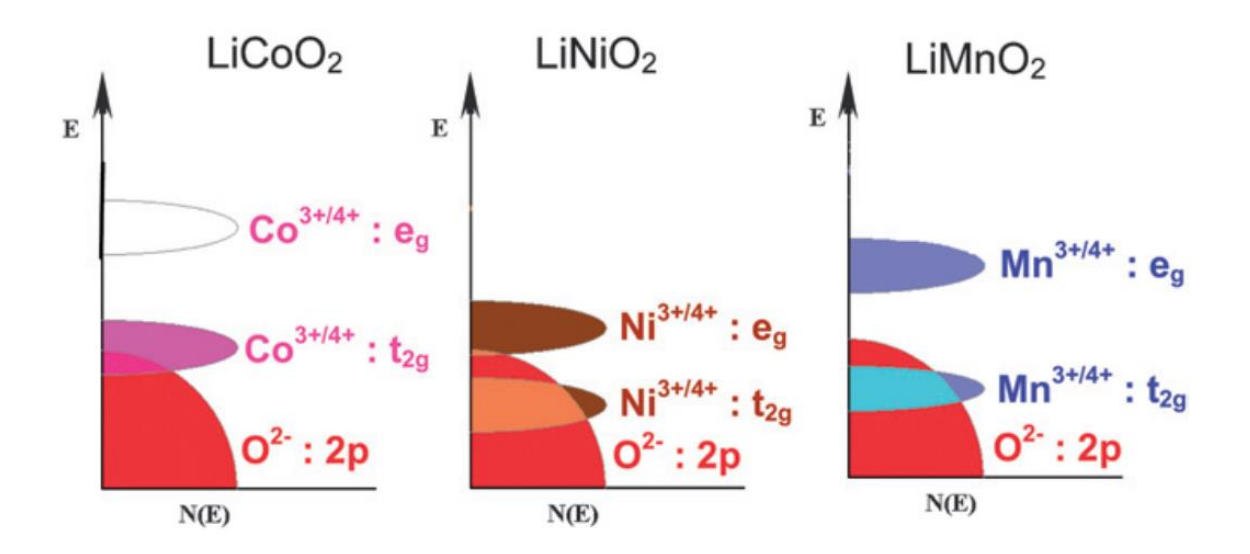


Figure 1.6 The energy diagram of (a) LiCoO₂, (b) LiNiO₂ and (c) LiMnO₂. The image is taken from the reference [32].

Figures 1.6 (b) and (c) show the energy diagram of LiNiO₂ and LiMnO₂, which are cathode alternatives to (a) LiCoO₂. Here, the energy level of the redox active Ni^{3+/4+}: e_q band slightly overlaps with the top of the O²-:2p band, and it enables the removal of a significant amount of Li⁺ in LiNiO₂ without the loss of the O². In contrast, the energy level of the redox active Mn^{3+/4+}:e_q band is significantly higher than the O²⁻:2p band. Because of this, the Ni^{3+/4+} and Mn^{3+/4+} pairs provide better chemical stability in LiMO₂ when compared to $Co^{3+/4+}$ and these provide more cost-effective alternatives to cobalt. However, there are some drawbacks too with these materials. For instance, the synthesis of LiNiO2 with a balanced Li: Ni ratio of 1:1 is challenging due to the formation of a Li-deficient phase. During the synthesis process, the presence of Ni²⁺ causes the mixing of Li⁺ and Ni²⁺ cations in Li layer, with the Li_{1-x}Ni_{1+x}O₂ formula. When the cation mixing degree within Li layer increases, the Li₂Ni₈O₁₀ is formed and reduces the capacity by preventing the diffusion of Li⁺ ions. In addition, LiNiO₂ exhibits multiphase transitions along charging and discharging, which result in structural instabilities [33]. The long-term cycle stability of LiNiO₂ is severely constrained by these phase transitions. Moreover, when the LiNiO₂ crystal lattice is substantially delithiated, the release of O₂ gas threatens thermal stability at temperatures above 180 °C. The exothermic reaction causes a decomposition process into a cubic spinel

LiNi₂O₄ and rocksalt NiO due to release of O₂ [34] and can lead to the formation of micro cracks [35, 36]. The structural integrity of LiNiO₂ can therefore became comprised due to the presence of unwanted cation disordering, multiple phase transitions, micro crack formation, and O₂ leakage [37]. Alternatively, LiMnO₂ exhibits a structural transition from layered to spinel during the charge-discharging process [38]. The electrochemical performance of LiMnO₂ is impacted by the structural shifting from layered to spinel phase resulting in capacity fade [39]. For the above reasons, both LiNiO₂ and LiMnO₂ require additional research to deliver on their promise for use in commercial lithium-ion batteries. On the other hand, mixed LiNi_{1-y}Co_yO₂ or LiNi_yMn_yCo_{1-2y}O₂ (NMC) phases can overcome some of these disadvantages [40]-[41-43], [44].

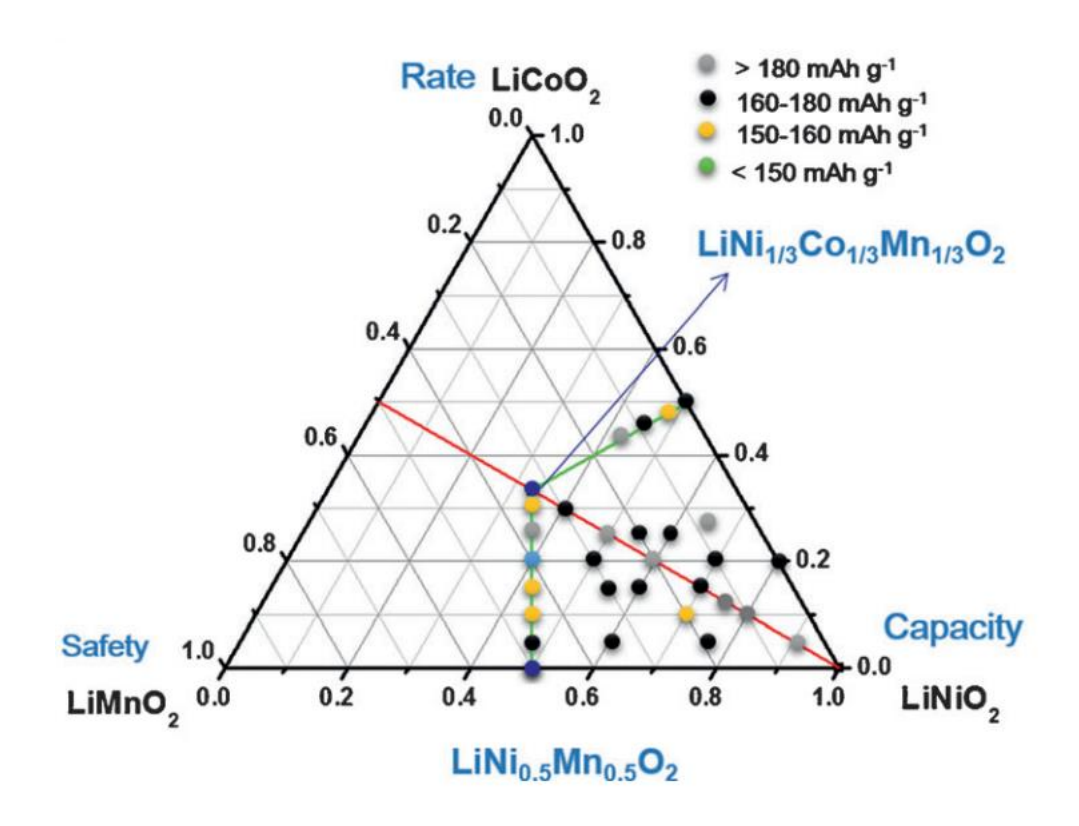


Figure 1.7 The phase diagrams show the LiCoO₂, LiNiO₂, and LiMnO₂ stoichiometrically composition. The dots on the diagram describe the corresponding materials, LiNi_{1-x-y}Co_xMn_yO₂ [45].

1.5. Exploration of Lithium Excess Cathodes Based on Manganese

Li-excess cation disordered rock salt (DRX) materials have emerged as highly promising group of cathodes that offer several advantages over traditional layered

oxides. These cathodes have the potential to achieve high specific energy densities, reaching up to 1000 Wh kg⁻¹ [46]. Additionally, they utilize low-cost elements that are abundantly available in Earth's crust, ensuring a more sustainable and cost-effective approach to cathode production. Although LCO and NMC cathodes exhibit promising performance, their significant nickel (Ni) and cobalt (Co) content present challenges in terms of cost and supply chain stability. The high levels of Ni and Co in these cathodes contribute to increased costs and raise concerns about reliability and sustainability of the materials' availability. Consequently, the advancement of cathodes that do not contain Co or Ni is crucial to fulfil the continuously increasing energy requirement. Figure 1.8 show that the comparison of price of Co, Ni and Mn elements over the years [47].

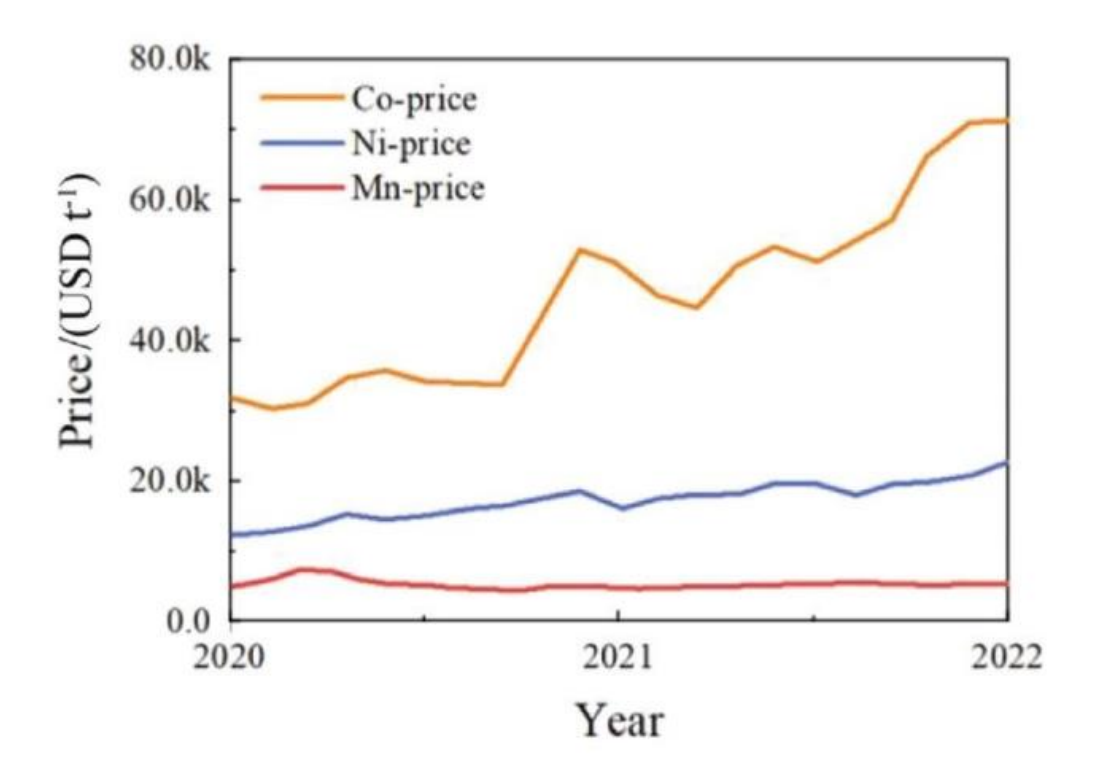


Figure 1.8 The comparison of price increases of Co, Ni, Mn elements over the years.

Several disordered cation rock salt cathode compounds have been studied, such as structures based on Li₃NbO₄, Li_{1.2}Ni_{0.333}Ti_{0.333}Mo_{0.133}O₂, Li₂TiO₃, Li_{1.9}Mn_{0.95}O_{2.05}F_{0.95} etc. (ref). Among these materials, the Mn-based cation disordered rock salt cathode

materials show great promise due to their non-expensive price, non-toxicity, and Earth abundance. Also, the thermal stability of the Mn-based cathode compound could be supplied by the Mn⁴⁺ ions in the full charged state.

The cation-disordered rock salt structures have an α-LiFeO₂ type crystal structure, illustrated in Figure 1.9. It has been suggested that this type of structure is electrochemically inactive with the fully disordered cation arrangement leading to poor lithium diffusion. A few studies have indicated that the electrochemical performances deteriorate as the degree of cation disordering as increases in both olivine structure and layered structure cathodes during cycling, due to the migration of transition metal into the Li layers that may hinder the Li⁺ diffusion. Interestingly, recent reports have found that the disordered cation structures might impact positively on Li⁺ transport properties and generate only small volume changes upon charge-discharge processes [48]. Moreover, the structure also provides an opportunity to extend to further transition metals, extending the chemical species for the design of positive electrode materials.

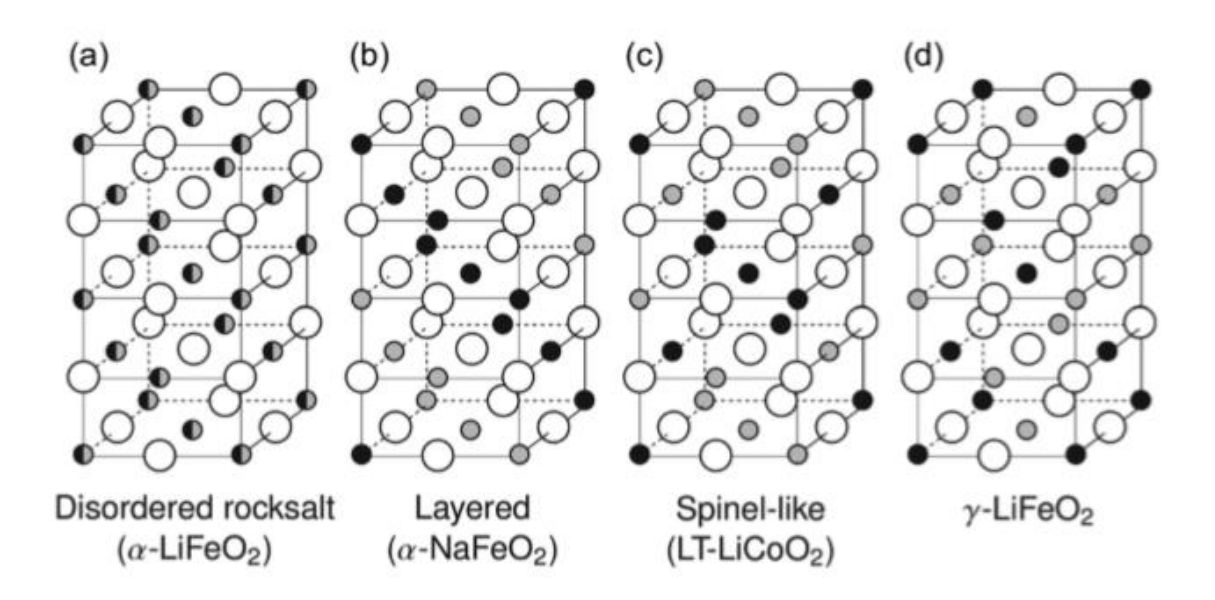


Figure 1.9 General rock salt type lithium transition metal oxide crystal structure (a) cation disordered rock salt, (b) layered, (c) spinel-like, and (d) χ-LiFeO₂ [49].

1.6. Li Migration in Disordered Rock salt

Li+ mobility in the rock salt lithium metal oxides occurs through an octahedral-tetrahedral-octahedral pathway (sometimes termed o-t-o diffusion). Factors which can affect the activation energy for this diffusion process include the size of the activated tetrahedral site and the electrostatic nature of that site (e.g., the interactions between the Li+ in the tetrahedral site with the surrounding octahedral cations). We can consider this latter point in terms of tetrahedral clusters which manifest in the crystal structure. For o-t-o diffusion to take place, two octahedral Li+ must be connected through an intermediate tetrahedral site. For cation-ordered layered LiMO₂, two clustering scenarios result: LiM₃ clusters in the transition metal layer (designated 3-TM in Figure 1.10 (a) which are not involved in Li+ diffusion) and Li₃M clusters in the lithium layer (labelled 1-TM in Figure 1.10 (a) which permit Li+ diffusion). Since the size of the tetrahedral site is chiefly governed by the lithium content in the Li layer, we should focus on the electrostatic effects on diffusion processes.

As lithium departs the structure upon charging, it is the face-sharing octahedral Li⁺ in the 1-TM channels which depart first. The energy cost for this migration is plotted in Figure 1.10 (b), which shows that the strong columbic interactions between Li⁺ in the tetrahedral and octahedral sites result in a higher energy barrier for Li⁺ hops into isolated vacancies compared to hops into di-vacancies where such repulsions can be avoided. During charge, the oxidation state of the transition metals increases to maintain charge balance. This increases the resulting electrostatic interaction with the departing Li⁺ ion, which is offset by an increase in the slab spacing. These mechanisms manifest in the resulting activation energies for o-t-o diffusion, resulting in an increase in Li diffusivity with charge for lithium content in the range 0.5≤x<1 in Li_xMO₂ and a decrease for lower Li content due to decreasing layer spacing. Therefore, the Li⁺ diffusion properties are governed strongly by the Li concentration and dominated by the di vacancy mechanism.

The picture for Li diffusion in the disordered rock salt is different. Figure 1.10 (c) illustrates the tetrahedral clusters formed as a result of cation disorder. Cation mixing means that there is an increased barrier to ion diffusion via these 1-TM channels. However, the 0-TM channels are now accessible for ion diffusion. Given the lack of long-range order in these materials, disordered rock salt was thought to be

electrochemically inactive. However, ion percolation has now been established under certain conditions and alternative methods for establishing these percolation pathways must be considered. Pioneering in this field has been the work of Ceder and coworkers who have shown that the 0-TM channels show different lithium diffusion performance depending on the degree of cation disorder and Li percolation network, with 10% Li excess is shown to help the macroscopic Li⁺ diffusion in these disordered cation rock salt compounds [49].

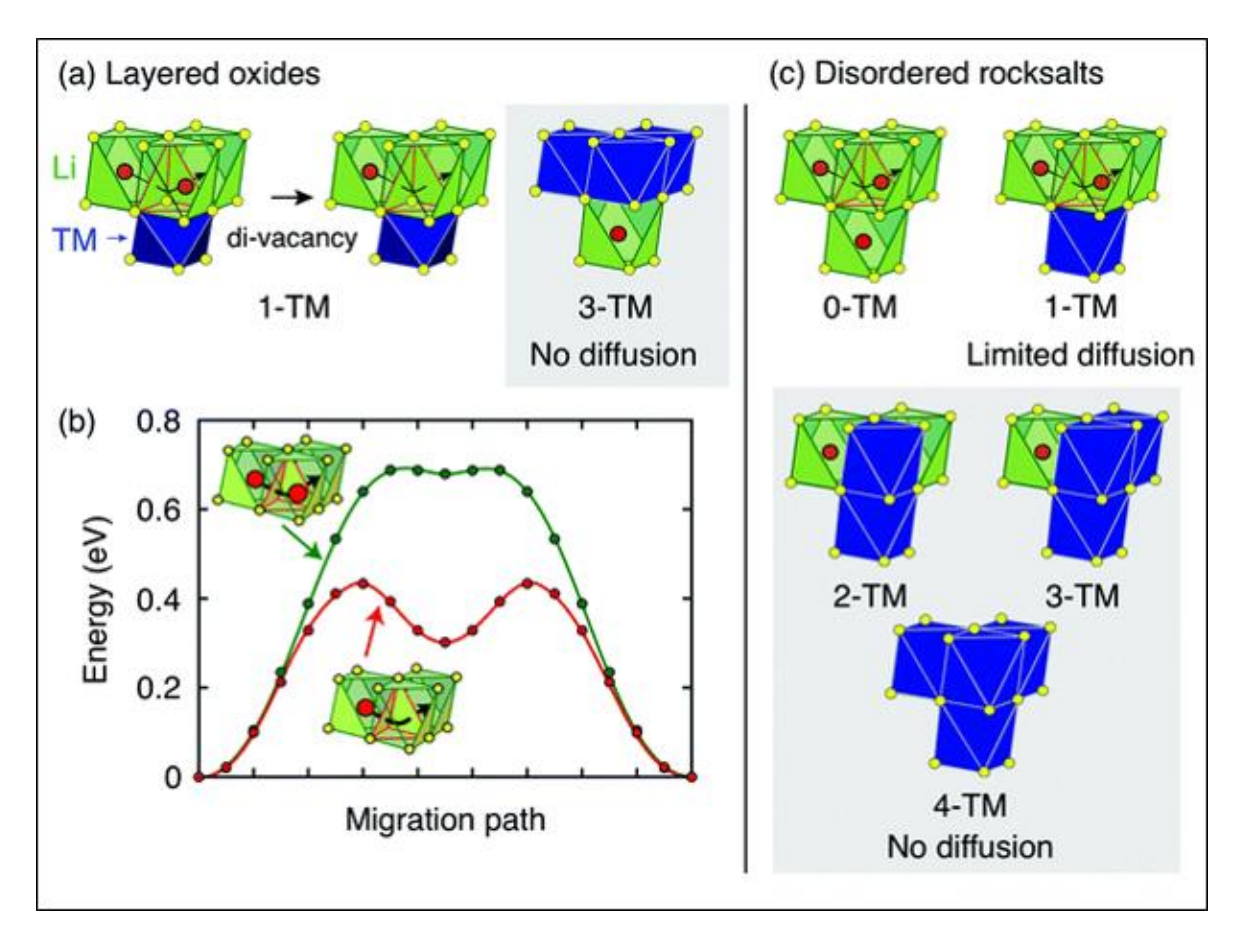


Figure 1.10 Li⁺ diffusion a) in the layered oxides, b) Li migration barrier in layered oxides, and c) in disordered rock salt [50].

On the other hand, cation short-range order has noted for disordered rock salt compounds and how this influences Li⁺ diffusion can be considered. This kind of short-range order has also been observed in Ni-rich disordered compounds and has been found to be damaging to the Li diffusion networks [51]. To determine the effects of short-range order, Jones et *al.* examined Li_{1.25}Nb_{0.25}Mn_{0.5}O₂ compounds under the different cooling temperature [52]. Slower cooling regimes result in greater ordering

than when rapid cooling is applied. For slow cooling conditions, the same sample also showed quicker voltage fade and poorer capacity retention than the material prepared by rapid cooling conditions. Moreover, Ji et *al.* investigated short range order in different high valence d⁰ cation such as Ti⁴⁺ and Zr⁴⁺ [53]. Although these compositions possess similar amount of Li, Mn, and dopant cations, these compounds showed different tetrahedral clusters, which determine diffusion channels. Depending on ion size, the Ti⁴⁺ ions support the lithium diffusion via Li₄ cluster, and the Zr⁴⁺ ions lead to weaker diffusion.

1.7. Synthetic Approach to Disordered Rocksalt Materials

The characteristics of functional materials, including battery materials, are greatly influenced by the synthetic methods used during their preparation. The crystal structure, particle size, and morphology of the constituent materials play a significant role in determining electrochemical performance parameters such as specific capacity and rate capability. It is essential to use appropriate synthesis methods to design advanced materials and exploring new techniques could lead to significant advancements in future technologies [54]. Different synthesis methods have been used to obtain the desired battery material, such as solid-state, sol-gel, hydrothermal, co-precipitation, mechanosynthesis, amongst others [55].

1.7.1. Solid-State Synthesis

Solid-state synthesis is a most common strategy to produce inorganic materials. The synthesis requires the initial mixing of the starting materials and then heating solid materials in a furnace at high temperatures. However, solid-state synthesis has some drawbacks, including high temperatures and prolonged heating times, leading to high energy consumption. In addition to this, control over particle size and disorder is a challenge as high temperatures and long reaction times will favour bulk materials and thermodynamic products.

1.7.2. Mechanosynthesis

Mechanosynthesis has a lengthy historical background and is still a very important technique today. Mechanosynthesis began in ancient times by using mortar and pestle to produce clay or grinding seed and wheat [56]. In the literature, mechanical synthesis was first mentioned by Matthew Carey Lea [57], referring to compounds that show different reactions under mechanical action and heat [58]. And then Wilhelm Ostwald

coined the term mechanochemistry in 1919 [59]; however, the first accepted definition was made by Gerhard Heinicke in 1984 [60].

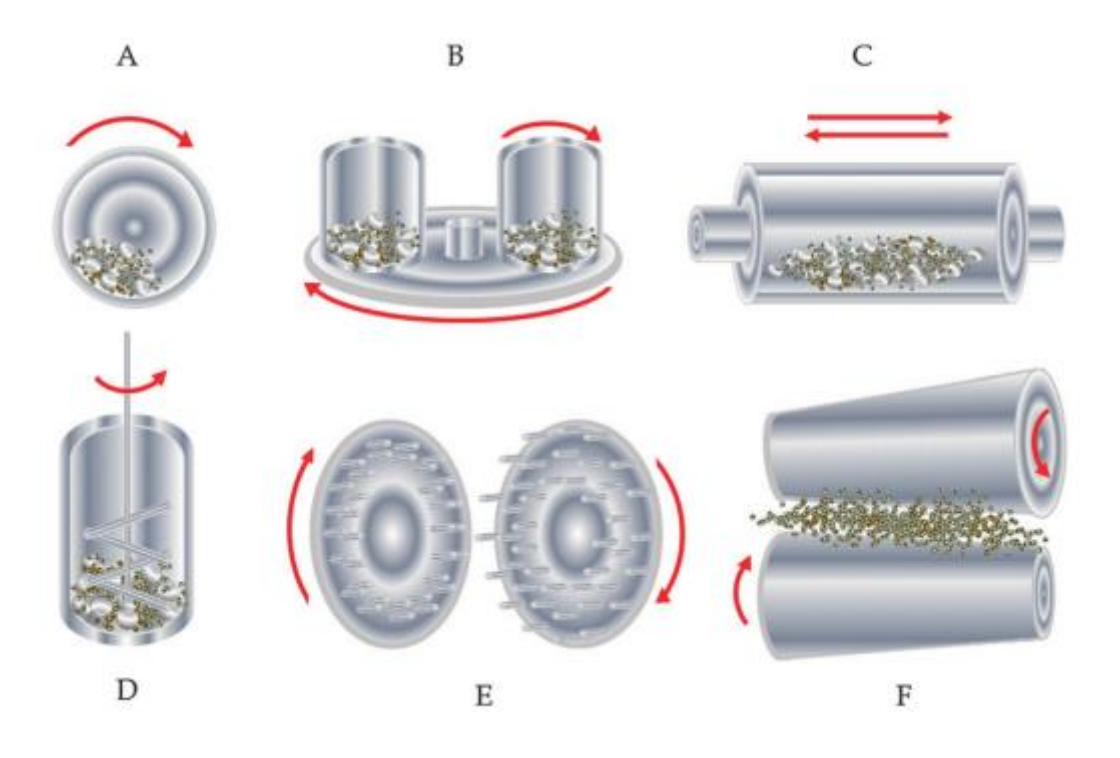


Figure 1.11 The different type of high-energy milling equipment a) ball mill, b) planetary mill, c) vibration mill, d) stirring ball mill, e) pin mill, f) rolling milling. Need permission [61].

Mechanosynthesis focuses on the chemical and physical changes that mechanical activity causes to solids. Currently, mechanosynthesis is the most common technique used for reducing the size of solid particles. It is also employed for effectively mixing and combining chemical elements at the atomic level and initiating or expediting chemical reactions in the solid state. Presently, high-energy ball milling machines are the most common tool for synthesis. The ball mills are classified according to the direction of movement and shown in Figure 1.11. In the ball mills, the chemicals are contained within a jar with balls. Depending on the direction of movement, the balls transfer energy through impact, shearing and friction forces [62]. During the milling, the collision of the powder and balls causes particle deformation and fracturing. Resulting from the collision, the chemical structures become dislocated and

disordered and then caused by reducing particle size. In this reaction, the chemicals are contained within a jar with balls. In this thesis, the planetary ball mill was used.

Synthesis of these cation-disordered materials often requires mechanochemical methods to achieve disorder. Because of the non-equilibrium thermodynamics of mechanical milling, the isotropic strain of the powder will reduce, and the disordered cation rock salt can be synthesized more easily. For instance, the synthesis of Li₂Mn_{2/3}Nb_{1/3}O₂F disordered rock salt requires temperatures of approximately 1750 °C theoretically but can be synthesized mechanochemically via high-energy ball milling at room temperature [63]. The reported Li₄Mn₂O₅ nanostructured phase, synthesised via the mechanochemical route at room temperature, has demonstrated discharge capacities of 355 mAh g⁻¹, representing one of the highest capacity values to date for a lithium manganese oxide material [64].

1.8. Main Challenges facing wider uptake of disordered materials.

Cation disordered rock salt materials have promising properties for Li-ion batteries, but there are also some challenges to overcome. During cycling, cation disordered rock salt cathodes can suffer from capacity reduction or structural deformations due to degradation problems [65, 66]. Figure 1.12 summarize the general problems of cation disordered rock salt cathodes during long cycling.

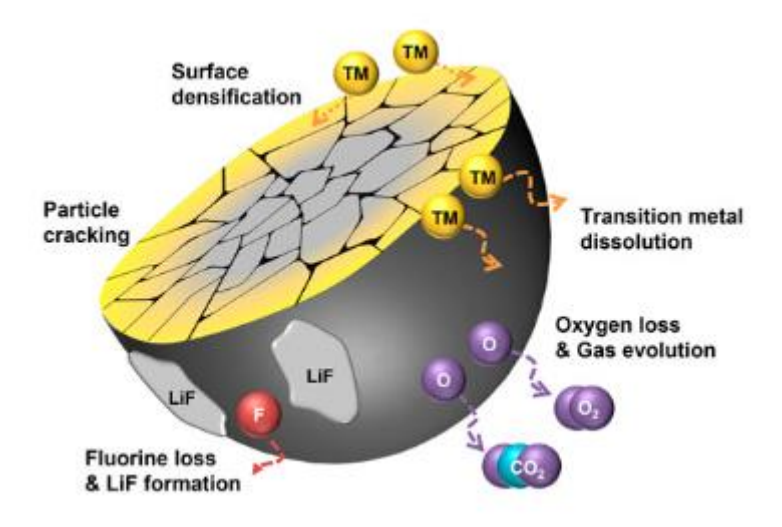


Figure 1.12 Visual representation of the degradation of Li-excess cation disordered rock salt cathodes [67].

1.8.1. Oxygen based charge compensation mechanism for cation- disordered rock salt Li-ion cathodes

In the LMOs, the charge mechanism depends on Li⁺ extraction and M oxidation state. To date, several studies have suggested O species may also join in the redox mechanism, especially in Li-excess and/or cation-disordered materials. A much debated question is whether the oxygen charge compensation could be adapted to improve the energy density. It is known that anion redox supplies high initial capacity but at the same time gives rise to speedy capacity fade [68].

Understanding how anion redox restrains and/or stabilizes, is a significant driving factors of cathode research studies. Ceder et *al.* have investigated the O redox process in Li-excess LMOs [69]. In the layered LiMO₂ structure, all of oxygen are connected to three lithium with three metal and every oxygen 2p orbital hybridizes with a metal orbital. However, in the Li-excess and/or DRXs, oxygen could be different coordination such as Li-O-M, Li-O-Li and M-O-M depending on Li content and the degree of cation disorder. It found that when the Li-O-Li band overlaps with e_g* band, it can lead to oxidation processes such as in Ni^{2+/4+} compounds. Otherwise, Mn^{3+/4+} e_g* band are not able to overlap with Li-O-Li band and show better performance.

1.8.2. Fluorination for cation-disordered rock salt Li-ion cathodes

Fluorination is generally used for increasing the thermal and electrochemical stability in battery materials. Thus, whilst the incorporation of fluorine increases the stability of organic electrolytes, fluorinated salts and solutions are used to help stabilise high voltage inorganic electrolyte. Studies also indicate that fluorinated coatings on cathodes are able might to prohibit undesirable exothermic reactions at the electrode/electrolyte surface upon charge [70].

In Li-excess disordered cation rock salt cathodes, it has been suggested that F substitution for O anions could help to improve battery capacity and decrease the irreversible processes at high voltage which causes to degradation during cycling. Previous studies have shown that the solubility of fluorine in layered lithium metal oxides is weak; therefore, fluorine is not incorporated into transition metal oxide is material structure and LiF accumulates at the surface instead [71, 72].

The solubility of fluorine was investigated to understand the effect of F incorporation on layered and disordered structures. It is found that forming anion sites with less

transition metal neighbours could create an opportunity for F incorporation into disordered rocksalt structure, whereas this is not viable in conventional layered oxide structures [70]. In contrast to layered lithium metal oxides, oxyfluoride cation disordered rocksalt structures can be accessed through a mechanochemical route [73] Furthermore, compared to the solid-state route, the mechanochemical synthesis opens up an opportunity to enable high F contents of around 30%. The Li₂VO₂F disordered cation materials have been synthesised via this method with the incorporation of fluorine into transition metal oxide verified by ¹⁹F NMR spectroscopy [74].

According to the effect of fluorination on the voltage and capacity retentions studies, it is found that oxyfluoride structures demonstrate about 20% increase in redox active transition metal content compared to the non-fluorinated compound. It means that the F substitution for O leads to a decrease in the valency of redox-active transition metals and thus a decreased dependence on O redox to achieve higher capacities. Due to this suppression of the oxygen redox, the oxyfluoride structures could reduce the amount of O₂ and CO₂ gas evolved upon charge at high voltages of ~4.6 V and decrease the extent of irreversible capacity, unlike non-oxyfluoride structures which rely on oxygen redox to a greater extent [75].

In addition to capacity effect, fluorination may also affect Li⁺ transport and short-range order in disordered rock salt structure because of its attraction to Li. According to NMR spectroscopy and Monte Carlo simulation results, F ions are not always located around Li-rich clusters in disordered rock salt structure, and instead, they are ~around 90 % located to 6 Li or 5 Li- 1 M. Furthermore, the amount of F doping also effect on the Li⁺ transport with high F doping aiding percolation, whereas the low F doping can lead to low percolation performance. This reveals that the concentration of F is an important parameter for Li percolation and requires further insight and optimization [76].

Consequently, the present studies examined the effect of fluorination on the capacity, voltage, percolation, and stability in Li-excess disordered cation cathode materials. These studies confirm that fluorination is associated with enhanced battery performance. However, there are some difficulties relating to the structural characterization of such materials because fluorination cannot be detected confidently

with X-ray diffraction and cannot be confidently distinguished from oxygen using neutron diffraction. In the future works, it should be noted that X-ray absorption spectroscopy could be useful for investigating the fluorination in these disordered rock salts.

1.9. Aims and Objectives of This Work

The aim of this PhD research is to focus on the design and characterization of high energy density next generation lithium-ion battery positive electrodes. The electrochemical energy storage market requires high energy density rechargeable batteries which are non-expensive. A key component for reduction in cost and improvements in capacity is the cathode. Compared to commercial layered LMO systems, such as NCA-type and NMC-type compounds, or the standard LCO cathode, the capacity and energy density of the disordered rock salt structure compound could be at least as good if not superior. However, these disordered rock salt materials are not as well optimized as today's commercial cathodes, and better insight into the relation between chemistry, structure and performance is required in order to optimise these materials for broader application.

Therefore, the objectives of this PhD are to investigate the design of Li-excess cation disordered rock salt cathode materials based on Mn compounds and examining their physical and structural properties and electrochemical performance for applications in Li-ion batteries. Investigations into the experimental conditions (synthesis methods, the effect of time, molar ratio, etc.) that are used to synthesise these materials is of initial interest in this research, in order to relate synthesis route to resulting material structure and electrochemical performance. Furthermore, investigating a new combined strategy of high valence cation Zr-substitution alongside fluorination presents an interesting route tailoring the Li+ transport properties and the transition metal redox behaviour of these disordered rock salt materials. As this family of cathodes are relatively new (compared to transition metal layered oxides) the work carried out here on the Mn-based structures will be helpful in establishing a thorough foundation for new and interesting disordered rock salt compositions for the lithiumion batteries of the future.

Chapter 2: Experimental Methods

2.1. Introduction

The chapter details the methods used to obtain and analyse the materials synthesized in this thesis, as well as the fundamental principles for understanding the main techniques used to investigate their properties.

2.2. Materials

The following chemicals were purchased and used without further purification: Lithium carbonate (Li₂CO₃) (Aldrich), Lithium peroxide (Li₂O₂) (Sigma Aldrich), Lithium oxide (Li₂O) (Sigma Aldrich), Lithium fluoride, LiF (Aldrich), Manganese carbonate, (MnCO₃) (Alfa), Manganese oxide, MnO, Manganese (III) oxide (Mn₂O₃) (Sigma Aldrich), Zirconia oxide (ZrO₂) (Alfa), Tungsten (IV) oxide (WO₂) (Alfa).

For battery fabrication the following were purchased and used: 1 M lithium hexafluorophosphate (LiPF₆) in ethylene carbonate (EC) and dimethyl carbonate (DMC) 1:1 v/v (Solvionic) and 1 M lithium hexafluorophosphate (LiPF₆) in ethylene carbonate (EC) and dimethyl carbonate (EMC) 3:7 v/v were used as electrolytes, 1-methyl-2-pyrrolidone (NMP) as a solvent, polytetrafluoroethylene (PTFE) (Sigma Aldrich) and polyvinylidene fluoride (PVDF) (Aldrich) as a binder, Li metal ribbon and Li metal disk, Whatman glass microfiber filter as separators, Carbon black KETJEN BLACK EC-600 JD (AkzoNobel) as a conductive additive.

2.3. Synthetic Methodologies

Two main synthetic methods were utilized to develop the materials in this thesis: Solid state synthesis and Mechanosynthesis.

2.3.1. Solid State Synthesis

2.3.1.1. Synthesis of Li₂MnO₃ from Li₂CO₃ and MnCO₃ precursors

For the solid-state synthesis of the Li₂MnO₃, stoichiometric amounts of Li₂CO₃ and MnCO₃ (previously dried at 250 °C for 24 hours) were weighed and mixed in 5 mL acetone with ball milling at a rate 20 Hz for 99 minutes or 120 minutes in Retsch

MM200 Mixer Mill. A 10 mL ZrO₂ jar and 1 zirconia ball were used for ball milling. The milled mixture was the dried at 50 °C and the fine powder was pelleted at 2 tonnes under uniaxial pressure. The pellet was transferred to a muffle furnace in air and heated at 450 °C for 24 hours with a ramping rate of 5 °C min⁻¹ in order to decompose the precursors. Once cool at the room temperature, the obtained powder was reground using an agate pestle and mortar and pelleted for a second heat treatment at 450 °C for 24 hours in the same muffle furnace. A brown powder was obtained as final product. The same protocol was also applied at 1000 °C for 24 hours.

2.3.1.2. Synthesis of Li₂MnO₃ from Li₂CO₃ and Mn₂O₃ precursors

For the solid-state synthesis of the Li₂MnO₃, Li₂CO₃ and Mn₂O₃ (as that described in Section 2.3.1.1.) was dried at 250 °C overnight and were then weighed in their stoichiometric amounts. The precursors were mixed and ground with an agate pestle and mortar for 30 minutes to prepare the powder. A black powder was obtained. Then, the mixed powder was transferred to a muffle furnace in air and heated at 800 °C for 10 hours with a ramping rate of 5 °C min⁻¹. A brick-red powder was obtained.

2.3.1.3. Thermal Decomposition of Mn (II)CO₃ to Mn₂O₃

To facilitate the conversion of Mn (II)CO₃ to Mn₂O₃, thermal decomposition methods was used. Mn (II)CO₃ was transferred to a muffle furnace in air and was then heated at 600 °C for 48 hours with a ramping rate of 5 °C. The obtain powder was cooled to room temperature inside the furnace.

2.3.2. Mechanosynthesis

2.3.2.1. Synthesis of Li₂MnO₃ via Mechanosynthesis

For the mechanosynthesis of the Li₂MnO₃, a mechanochemical ball-milling method was used. The precursors were weighted in their stoichiometric amounts and were then ball-milled at 750 rpm for different times in a Fritsch Pulverisette 7 planetary ball mill. A 20 mL air-tight zirconia jar with 25 of 5 mm diameter zirconia balls were used for ball-milling in order to avoid contamination. The precursors were weighed and sealed in zirconia jars in an argon filled glovebox with H₂O and O₂ less than 1 ppm.

To prevent excessive heat generation, the milling process was undertaken in intervals of 5 minutes, followed by 10 minutes of rest.

2.3.2.2. Synthesis of Li₂MnO₂F via Mechanosynthesis -one step

For the mechanosynthesis of the Li₂MnO_{3-x}F_x, Li₂O₂ and/or Li₂O as Li sources, MnO and/or Mn₂O₃ as Mn sources, and LiF were weighed in their stoichiometric amounts and were then ball-milled at 750 rpm for different times in a Fritsch Pulverisette 7 planetary ball mill. A 20 mL airtight zirconia jar with 25 of 5 mm diameter zirconia balls were used for ball-milling in order to avoid contamination. The precursors were weighed and sealed in zirconia jars in an argon filled glovebox with H₂O and O₂ less than 1 ppm. To prevent excessive heat generation, the milling process was undertaken in intervals of 5 minutes, followed by 10 minutes of rest.

2.3.2.3. Synthesis of Li₂MnO₂F via Mechanosynthesis- two step

For the two step mechanosynthesis of the Li₂MnO_{3-x}F_x, Li₂O₂ and/or Li₂O as Li sources, MnO and/or Mn₂O₃ as Mn sources, and LiF were weighed in their stoichiometric amounts and were then ball-milled at 750 rpm for different times in a Fritsch Pulverisette 7 planetary ball mill. In the synthesis methods, the oxide precursor mixed at 750 rpm for 9 hours (or 12 hours) and the LiF precursor added and mixed at 750 rpm for 9 hours (or 12 hours). A 20 mL air-tight zirconia jar with 25 of 5 mm diameter zirconia balls were used for ball-milling in order to avoid contamination. The precursors were weighed and sealed in zirconia jars in an argon filled glovebox with H₂O and O₂ less than 1 ppm. To prevent excessive heat generation, the milling process was undertaken in intervals of 5 minutes, followed by 10 minutes of rest.

2.3.2.4. Synthesis of Zr-doped Li₂MnO₂F via Mechanosynthesis -one step

For the mechanosynthesis of Li₂Mn_{1-x}Zr_xO₂F, Li₂O₂, MnO, ZrO₂, LiF were weighted in their stoichiometric amounts and were then ball-milled at 750 rpm for different times in a Fritsch Pulverisette 7 planetary ball mill. A 20 mL air-tight zirconia jar with 25 of 5 mm diameter zirconia balls were used for ball-milling in order to avoid contamination. The precursors were weighed and sealed in zirconia jars in an argon filled glovebox

with H₂O and O₂ less than 1 ppm. To prevent excessive heat generation, the milling process was undertaken in intervals of 5 minutes, followed by 10 minutes of rest.

2.3.2.5. Synthesis of Zr-doped Li₂MnO₂F via Mechanosynthesis- two step

For the mechanosynthesis of Li₂Mn_{1-x}Zr_xO₂F, Li₂O₂, MnO, ZrO₂, LiF were weighted in their stoichiometric amounts and were then ball-milled at 750 rpm for different times in a Fritsch Pulverisette 7 planetary ball mill. In the synthesis methods, the oxide precursor mixed at 750 rpm for 9 hours (or 12 hours) and the LiF precursor added and mixed at 750 rpm for 9 hours (or 12 hours). A 20 mL air-tight zirconia jar with 25 of 5 mm diameter zirconia balls were used for ball-milling in order to avoid contamination. The precursors were weighed and sealed in zirconia jars in an argon filled glovebox with H₂O and O₂ less than 1 ppm. To prevent excessive heat generation, the milling process was undertaken in intervals of 5 minutes, followed by 10 minutes of rest.

2.4. Characterization Techniques

2.4.1. Crystal Structure Characterization

2.4.1.1. Powder X-ray Diffraction (PXRD)

Powder X-ray diffraction (PXRD) is an analytical technique to determine the crystal structure and structural properties of the materials. X-rays were discovered in 1895 by Wilhelm Rontgen [77], and the first diffraction pattern was published in 1892 by Maxwell von Laue [78]. An X-ray diffraction pattern represents the intensity of X-rays scattered by a sample at different angles. The X-ray diffractometer comprises an X-ray tube, a sample holder, and a detector. The X-ray tube generates X-rays by heating a filament which then releases electrons. These electrons move towards a metal target (generally copper, molybdenum or chromium). As the electrons collide with the metal target, they disperse energy and create monochromatic X-rays. When monochromatic X-ray reach to sample, the detector and the X-ray tube start to revolve around the sample to record the intensity of the diffracted X-rays.

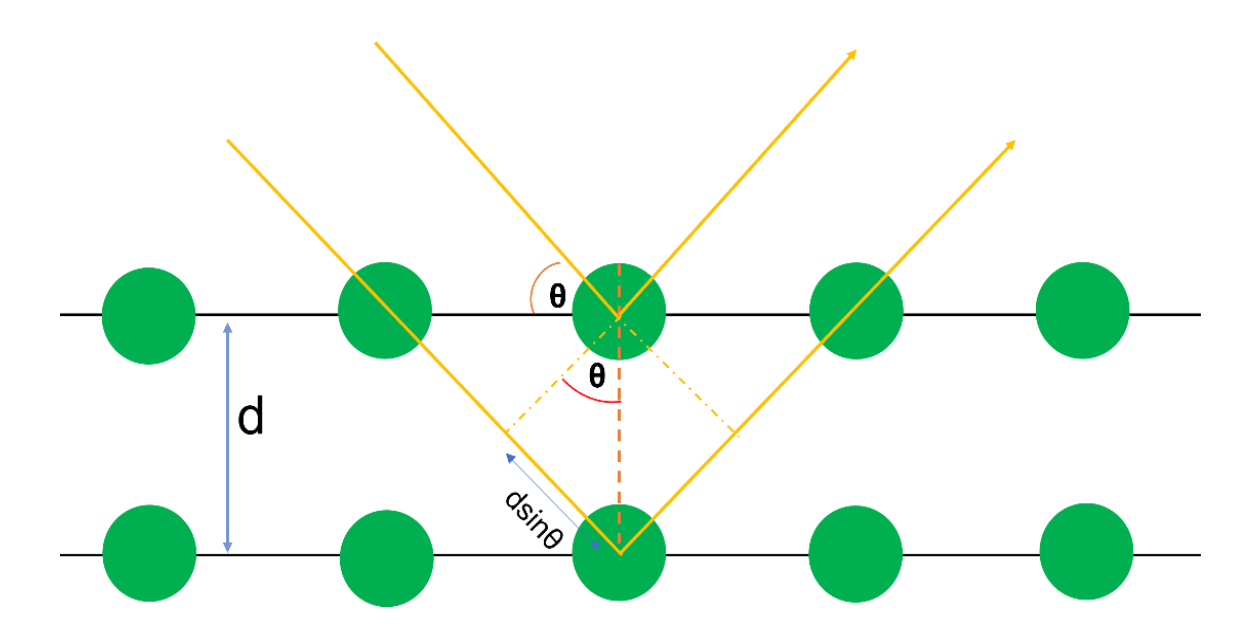


Figure 2.1 Bragg's law condition shown schematically. Based on Dinnebier and Billinge [79].

The recorded data can be defined by Bragg's law. Bragg equation is shown as schematically in Figure 2.2, and is given by Equation 2.1:

$$n \lambda = 2d \sin \theta \tag{2.1}$$

where λ is the wavelength of the incident beam, d is the lattice distance between adjacent places, θ is the diffraction angle and n is the number of the diffracted beam.

In this thesis, powder X-ray diffraction measurements were examined to characterize all synthesized samples. X-ray diffraction (XRD) patterns were obtained using a Rigaku MiniFlex diffractometer with Cu source (λ = 0.15418 nm) operated at 40 kV and 40 mA. The samples were scanned in the 20 range between 10° – 90° with a step size of 0.020. Before the X-ray diffraction measurement, the samples were ground using a mortar and pestle to obtain a homogenous particle size. After the X-ray diffraction measurement, the samples patterns were compared to the Inorganic Crystal Structure Database (ICSD) to examine the phases obtained and any impurity phases which may also be present. Rietveld refinement analysis was performed using Generalised Structure Analysis System (GSAS2) software.

2.4.1.2. Rietveld Refinement

Rietveld refinement may be used to determine the cell parameters, site occupancy, and atomic positions from the diffracted pattern of the crystal structure. Using the GSAS2 software and the graphical user interface EXPGUI, the Rietveld refinement of the diffraction data can be carried out.

The Rietveld method relies on the least squares mathematical technique which is employed to iteratively adjust a theoretical crystallographic model to model the experimental crystal structure. The objective is to align the model and the actual measured profile. In a Rietveld refinement the intensity of each data in the XRD diffraction pattern is computed using the equation specified. The most accurate alignment is achieved by minimizing between the observed data and the calculated fit through a process of function optimization. After undergoing a complete refinement process, the structural model can be regarded as a reliable representation of the actual structure. The refined model provides valuable parameter values including, atomic positions, site occupancies, cell volume, and cell parameters, which accurately describe the structure.

2.4.2. Scanning Electron Microscopy (SEM)

Scanning electron microscopy is a technique used to examine the morphology and particle size of the materials from nanometre to millimetre scale. A scanning electron microscope comprises an electron source, a series of electromagnetic lenses and a detector. A scanning electron microscope magnifies a sample by using a focused beam of electrons. The electron beam is scanned across the surface of the sample in a regular pattern, and the electrons that escape are employed to produce the pictures. Scanning electron microscopy can magnify an image up to 300,000 times. Each SEM image typically includes a scale bar, which is used to calculate the sizes of image features. SEM detectors capture two types of SEM images: secondary electron images and backscattered electron images. The shades of grey in a secondary electron image represent by the topography of the material. In backscattered electron images, the shades of grey represent by the atomic weight of the constituent element in the material.

In this thesis, SEM images were collected using an FEI Inspect F50 microscope at the Sorby Centre, Sheffield. The operating voltage was applied between 5 to 15 kV with the beam spot size ranging from 3.0 to 4.0 units. All samples were finely ground for SEM analysis, and the powder was placed on a sample holder coated with carbon tape. The samples were then sputter-coated with gold in a vacuum sealed chamber for approximately 20 seconds, to enhance the surface conductivity and prevent any damage cause by the electron beam.

2.4.3. Energy dispersive X-ray spectroscopy (EDX)

Energy dispersive X-ray spectroscopy (EDX) is a method employed to ascertain the elemental composition of a given specimen. The working principle of EDX relies on the generation of characteristic X-rays within the atoms of the specimen through the interactions with electrons from the incident beam. The X-rays produced can be detected and provide information on the elemental distribution within the sample under investigation. EDX data in this thesis were collected using the FEI Inspect F50 SEM.

2.4.4. Pair Distribution Function (PDF)

Traditional X-ray diffraction methods can describe crystalline materials where there is extended long range order. However, for materials where long-range order does not persist, such as nanoparticles, amorphous materials or disordered materials, alternative structural tools are necessary. Total scattering, where Bragg data from crystalline material together with diffuse scattering from material where long-range order is absent, can provide such a tool. Pair distribution function (PDF) analysis may be used to obtain information about the local structure of the material in real space, which provides a weighted histogram of all atom-atom distances present in the material under investigation. In this thesis, PDF data and analysis was carried out by collaborator, Dr Xiao Hua, at Lancaster University on samples detailed in this thesis.

2.4.5. Muon Spin Relaxation Spectroscopy (µ+-SR)

The muon spin relaxation spectroscopy technique provides information about the local ionic diffusion of cations in batteries. Traditional techniques for examining ion diffusion include nuclear magnetic resonance (NMR), electrical impedance spectroscopy (EIS) and quasi-elastic neutron scattering (QENS). Compared to μ^+ -SR, QENS technique enables the investigation of ionic diffusion on a limited time scale between 10⁻⁹ to 10⁻¹

 12 s range and it may not be able to measure when there is ionic diffusion outside this range. Although NMR measurements provides a broader time scale, the NMR technique can be complicated in the presence of magnetic ions since these have the potential to disrupt the spin lattice relaxation rate $(1/T_1)$. Among the various techniques employed for studying ionic diffusion, EIS stands out as the most extensively utilized methods. However, EIS has limitations imposed by significant factors such as the influence of grain boundaries and interfaces within electrodes. The μ^+ -SR technique offers advantages with a time scale between 10^{-5} to 10^{-8} s, ideally suited to detecting ion diffusion in battery materials [80].

A muon is a member of the Lepton family, a subatomic particle, and can be compared to either a heavy electron (about 200 times the mass of an electron) or a light proton (about 1/9 the mass of a proton), depending on its charge [81]. High-energy particle accelerators are required for µ+-SR experiments. Figure 2.2 shows the diagram of a standard µ+-SR experiment, wherein positrons produced from muon decay are detected by forward and backward detectors [82]. Muons can be generated by directing a high-energy proton beam onto a carbon target, producing pion particles. Positive pions decay, producing a positive muon and a muon neutrino. These muons become nearly 100% spin polarised as a parity violation. The muons are directed and focused through an intricate arrangement of bending magnets and quadrupoles to access the target material. In the experiment, once the muons collide with the sample, they rest within interstitial sites located close to highly electronegative regions. These regions typically correspond to the O2- anions found in oxide cathode materials used in Li-ion batteries. Due to the muon's spin, muons possess the ability to detect a broadening (Δ) of the field distribution caused by the local magnetic fields originating from nearby nuclei. Moreover, the movement of neighbouring nuclei can affect the fluctuation rate (v). The muon undergoes decay and releases a positron, which tends to exit the material in a direction aligned with the spin of the muon at the time of decay. The detection of decay positron asymmetry (Pz) is calculated by utilizing two detectors placed in front of and behind the sample stage. For the calculation, the equation 2.3 can used:

$$P_{z}(t) = a_{0} \frac{N_{F}(t) - \alpha N_{B}(t)}{N_{F}(t) + \alpha N_{B}(t)}$$
(2.3)

where a_0 represents the initial decay asymmetry and it is determined by the average energy of the muon beam, N_B and N_F represent the count of positrons observed by the detectors placed at the rear and front positions, respectively, and α represents a calibration parameter.

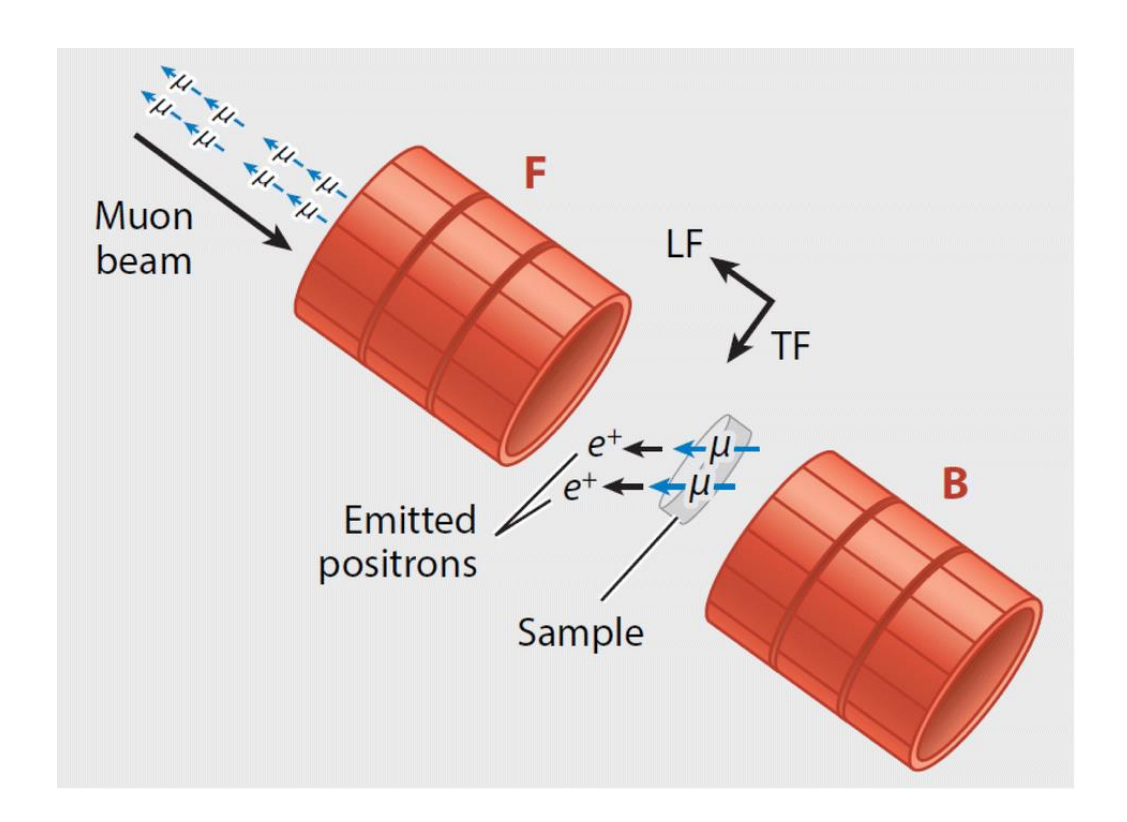


Figure 2.2 A standard μ^+ -SR experiments where positive muons implant within a sample, before decaying to produce positrons [82].

In this thesis, the local ionic diffusion of cations in battery materials is examined using the $\mu^+\text{-}SR$ technique. $\mu^+\text{-}SR$ experiments were undertaken on the EMU instrument beamline at the ISIS Pulsed Neutron and Muon Source in Oxford, UK. The data fittings were analysed using the Mantid workbench data analysis program. The EMU spectrometer is a specialized instrument and designed specifically for conducting measurement in zero field and longitudinal field measurements. Approximately 1 gram of powder samples were placed into titanium sample holders, along with up to 2 titanium backing discs to ensure a compact arrangement of the powder. The holders were then sealed using a titanium window that had a thickness of 25 μm . Titanium is selected due to its low depolarization effect on muons. Experiments were conducted

across the temperature range of 100K to 500 K at zero field (ZF) and applied longitudinal fields (LF) of 10 and 20 G at each temperature. The calibration constant α was determined by conducting a calibration measurement in a transverse field at 20 G under 300 K.

2.5. Electrochemical Characterization

2.5.1. Galvanostatic Cycling with Potential Limitation (GCPL)

Galvanostatic potentiostatic looping (GCPL) is an electrochemical method that enables the examination of the voltage behaviour in an electrochemical cell as a constant current is applied, progressing until specific voltage limits are attained. A schematic illustration of the procedure performed in a GPCL experiment was shown in Figure 2.3. Theoretically, a constant current is applied until a specific voltage value. There is specific voltage limit for each electrode materials, and this depends on the properties of the electrode materials. Once the voltage limit is achieved, the current direction is reversed till the next specific voltage limit. When the next voltage limit is completed, full cycling is successfully over. In Figure 2.3, "I" represent applied current, and "t" represent time. In galvanostatic cycling tests, the primary goal is to determine the energy storage and release capacity of the cell during the charge and discharge processes.

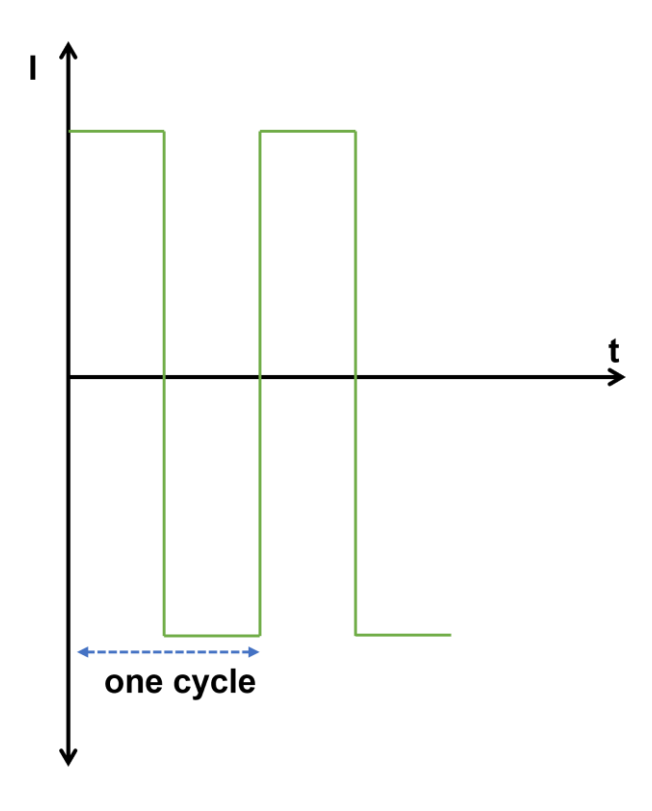


Figure 2.3 A schematic illustration of the GCPL experiment during charge/discharge cycling.

2.5.2. Electrode Preparation

To prepare the cathode pellets, each active cathode material was mixed with conductive carbon black and PTFE in a weight ratio of 60:20:20 (or 70:20:10 or 80:10:10) (Active Material: Carbon Black: Binder) using a mortar and pestle for 30 minutes. Subsequently, the electrode sheets were calendered using a calendering roll pressure machine to minimize porosity on the electrode surface and enhanced particle contact [83, 84]. The calendered electrodes were kept in a vacuum drying oven at 80°C overnight to remove any moisture or other volatiles before transferring the electrodes into a glovebox. 2032-coin type cells were fabricated, with Li metal chips as the counter electrode and 1M LiPF₆ in EC: EMC (3:7 vol.%) as electrolyte in an Arfilled glovebox. Coin cell measurements were carried out on a Maccor Battery Tester at room temperature.

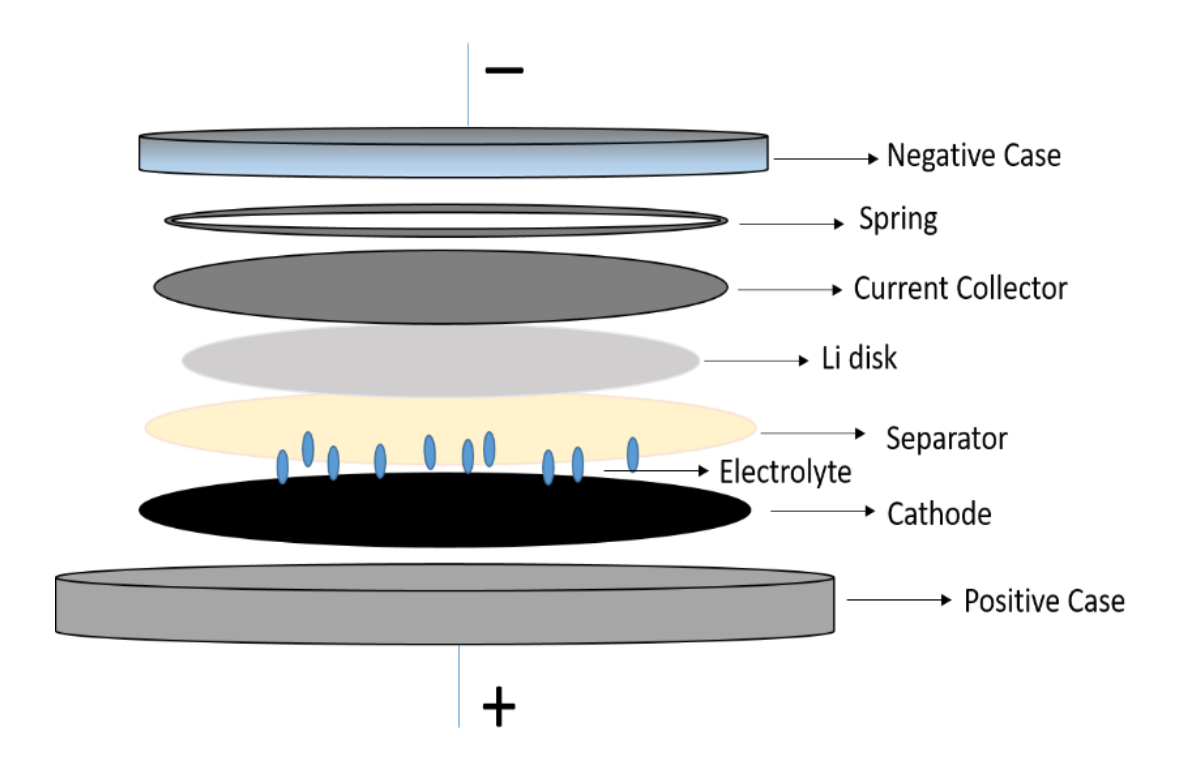


Figure 2.4 A schematic illustration of the 2032-coin type cells during cell fabrication.

Chapter 3: Manganese based cation-disordered rock salt cathode materials via mechanochemical synthesis.

3.1. Introduction

The lithium manganese oxides are a promising alternative for lithium-ion battery cathode due to its cost-effectiveness and abundant availability in nature. Within this group of oxides, LiMnO₂ and LiMn₂O₄ have exhibited favourable electrochemical features with high discharge capacity at high operating voltage. Although these cathodes have an active Mn^{3+/4+} redox pair in their structure during charge-discharge, they have difficulty maintaining the Mn³⁺ valance state because of Jahn-Teller distortion [85, 86]. With side reactions, deformations occur in their structure, and they begin to loss their structure. Lithium rich manganese oxide, Li₂MnO₃ is another promising Mn-based cathode with a high theoretical capacity of 460 mAh g⁻¹ at high voltage (>4.5 V). However, it is reported that the existence of the Mn⁴⁺ oxidation state renders the material electrochemically inactive, as Mn cannot be oxidised above the 4+ state when in an octahedral environment [87]. These compounds can also suffer oxygen loss due to challenges in stabilising the anionic redox [88].

In recently years, the development of cation disordered rock salt type lithium transition metal oxides has shown a promising alternative as high energy density cathodes for lithium-ion batteries [48]. Remarkably, manganese based disordered rock salt type cathodes have exhibited high capacities (>250 mAh g⁻¹) and energy densities (~1000 Wh kg⁻¹) [48, 65]. While the cationic redox from the transition metal and anionic redox from the oxygen work together to supply this high capacity [65, 89], the Mn based disordered rock salt cathodes display notable capacity fading with long cycling because of irreversible oxygen loss, structural degradation, and manganese dissolution in the electrolyte [67, 90].

One way in which to improve the electrochemical performance and supply structural stability during cycling is through the partial substitution of fluorine (F) into the oxygen (O) lattice [91, 92]. As described in section 1.8.2, fluorination is generally used for increasing the thermal and electrochemical stability in battery materials. Recently, Li₂Mn_{2/3}Nb_{1/3}O₂F and Li₂Mn_{1/2}Ti_{1/2}O₂F displayed a promising initial discharge capacity

of ~300 mAh g⁻¹ via the Mn²⁺/Mn⁴⁺ redox pair and O-redox [93]. These cathodes require the addition of a high valent d⁰ transition metal dopant such as Nb⁵⁺ or Ti⁴⁺ to stabilise the oxidised oxygen species. Among the F substitution disordered rock salt cathodes, the Li-Mn-O-F family of disordered rock salt cathodes show great promise high energy density cathodes and compositions in the Li₂MnO_{2-x}F_x (0 ≤ x ≤ 1) range are the focus in this chapter. In the literature, there are a few studies related to Li-Mn-O-F [94-96]. The partial substitution of fluorine into the oxygen lattice is notable efficient for enhancing cycling stability, although the underlying atomistic mechanism remains unknown.

In this chapter, the focus is on the mechanochemical synthesis of Li₂MnO_{3-x}F_x, which involves the partial substitution of fluorine into oxygen. The mechanochemical synthesis of the Li₂MnO_{3-x}F_x (x=0, 0.2, 0.8, 1, 1.2) compositions were examined. The crystal structure was studied by X-ray diffraction (XRD) prior to electrochemical analysis where coin cells were assembled and galvanostatic measurements taken. This was followed by utilization of the muon spin relaxation (μ^+ -SR) technique to probe local Li⁺ diffusion in Mn-based cation disordered rock salt cathodes of mechanochemical synthesis of Li₂MnO_{3-x}F_x (x=0, 0.2, 0.8, 1, 1.2).

3.2. Result and Discussion

3.2.1. Mechanosynthesis of manganese-based cation-disordered rock salt $Li_2MnO_{3-x}F_x$ (x=0, 0.2, 0.8, 1, 1.2) oxyfluoride cathodes for Li-ion batteries

Previous reports on the structure of Li₂MnO₃ have indicated that the choice of experimental parameters, such as Mn precursor and annealing conditions, can affect the degree of stacking disorder and morphology which has implications for subsequent electrochemical properties. The selection of synthetic route is also critical. For example, traditional solid state ceramic methods may be employed to synthesise Li₂MnO₃. Matsunaga et al [97], have shown that Li₂CO₃ and MnCO₃ precursors can be heated at elevated temperatures to obtain layered Li₂MnO₃. A typical XRD pattern for this synthesis is shown in Figure 3.1 and 3.2, where annealing temperatures of 450 °C and 1000 °C have been employed.

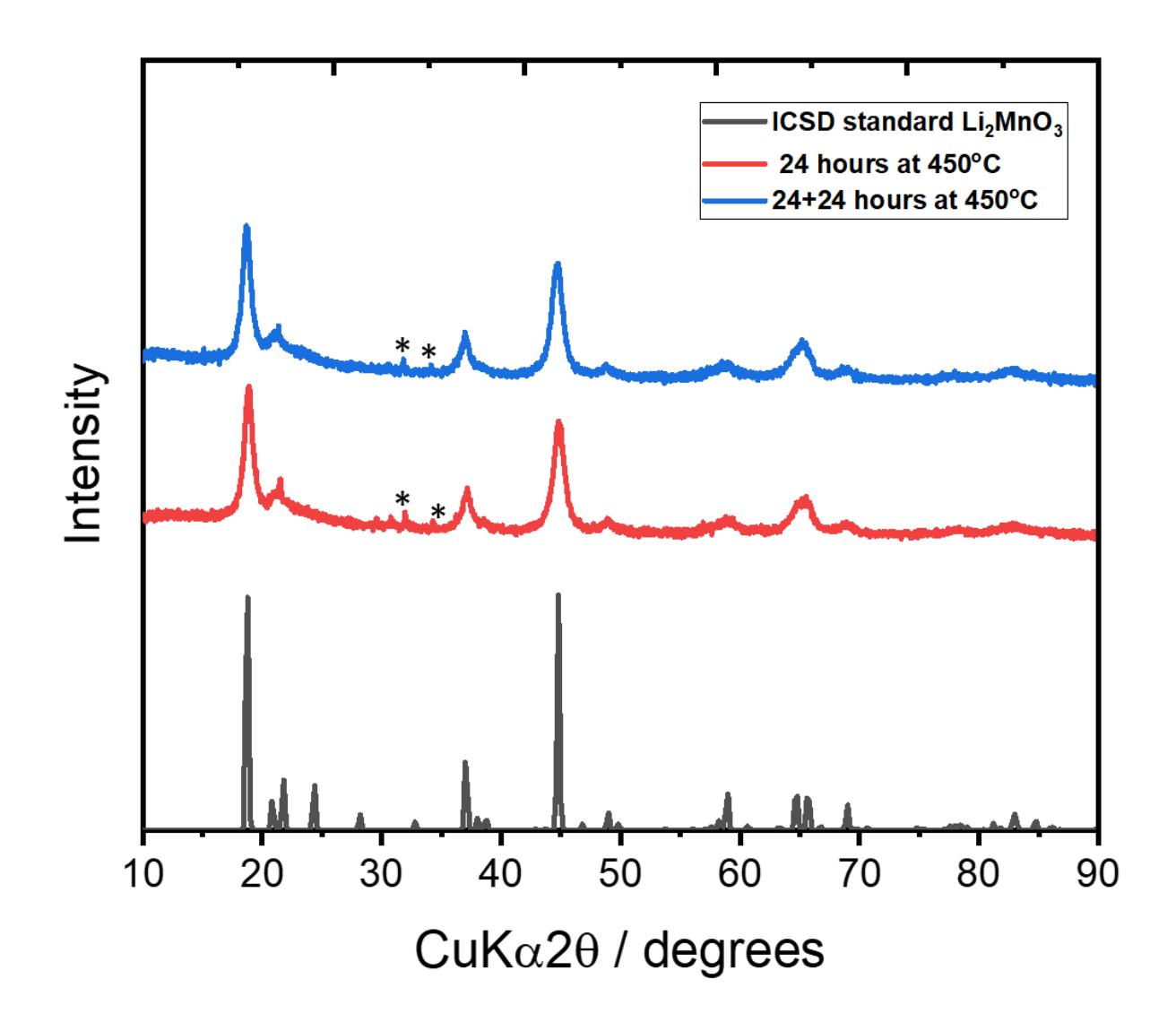


Figure 3.1 XRD patterns of the product during solid-state heat treatment of Li₂MnO₃ at 450 °C for 24 hours (red) and 48 hours (blue), alongside reference pattern for Li₂MnO₃ (black) obtain from ICSD (collection code 239796).

It is clear from these data that the products obtained strongly depend on the heat treatment conditions. The XRD patterns of the sample prepared at 450°C for 24 hours and 48 hours are shown in Figure 3.1 and comparison to the ICSD standard for Li₂MnO₃ (space group *C2/m*) reveals that, while the layered Li₂MnO₃ has been successfully synthesized, the sample is not phase pure. Peaks corresponding to Li₂CO₃ are observed with greater intensity with decreasing reaction time. Both patterns are characterized by broad peaks, which may suggest the presence of smaller crystallites. These broad, weak peaks could also indicate an amorphous nature to the material, which could be consistent with the low synthesis temperature used.

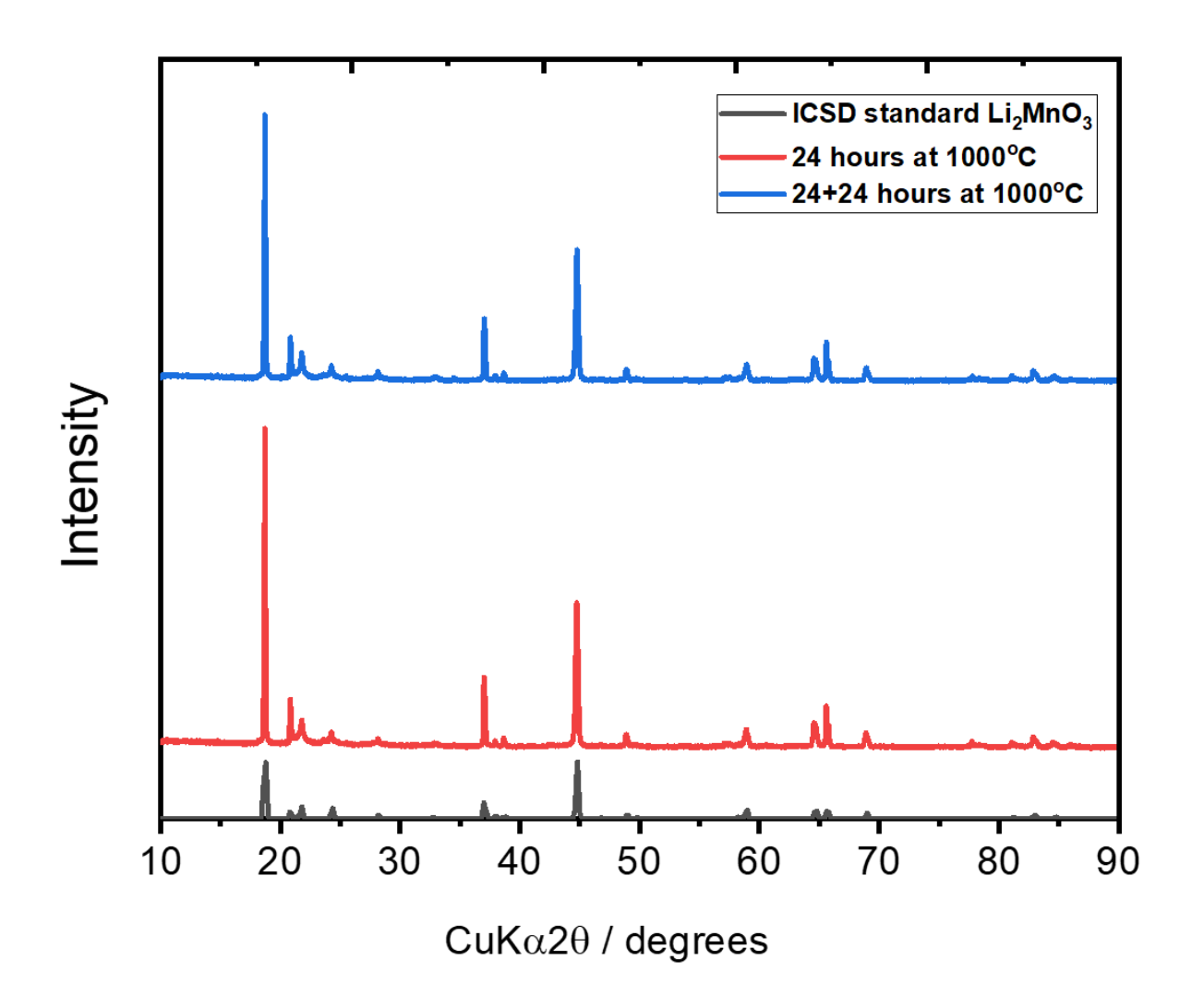


Figure 3.2 XRD patterns of the product during solid-state heat treatment of Li₂MnO₃ at 1000 °C for 24 hours (red) and 48 hours (blue), alongside reference pattern for Li₂MnO₃ (black) obtain from ICSD (collection code 239796).

Improvements in sample purity and crystallinity can be achieved by employing a higher annealing temperature. XRD patterns of a sample prepared after heat treatment at 1000°C for 24 hours and 48 hours (Figure 3.2) confirm this and peak matching to the ICSD Li₂MnO₃ confirm that layered Li₂MnO₃ (space group *C2/m*) has been achieved. Peaks corresponding to Li₂CO₃, apparent in the lower temperature syntheses, are not observed here. The XRD patterns at higher temperatures also show stronger peak intensity, which may indicate greater crystallinity in the products obtained likely a result of the higher synthesis temperature employed.

Rietveld refinement, shown in appendix 3.1, confirmed the C2/m space group with corresponding cell parameters: a= 4.92853 (Å), b= 8.53246 (Å), c= 5.02446 (Å), β= 109.228° and volume= 199.504 Å. Previous studies have demonstrated that highenergy ball milling of Li₂MnO₃ (space group C2/m) can induce the formation of nanosized particles, which can improve capacity retention [98]. Previous work by Diaz-Lopez and coworkers has demonstrated that ball-milling of the layered C2/m phase can produce nanosized particles where the local structure is in the rhombohedral R-3m space group, rather than the rock salt Fm-3m space group [87, 98]. Here, ballmilling of the Li₂MnO₃ sample obtained at 450°C was completed to investigate this. Again, there are peaks in the XRD patterns which indicate the presence of impurity phases (Figure 3.3). It may be possible to fine-tune the ceramic solid-state method in combination with ball-milling, but as the results above show there are multiple parameters across both steps which would require optimising. In an effort to avoid unwanted side products and achieve smaller particle sizes in a single step, mechanochemical synthesis has been applied in the synthesis of a series of disordered rock salt phases.

To examine the inclusion of F on the synthesis and electrochemical properties of disordered rock salt cathodes, a series of Li₂MnO_{3-x}F_x compounds were prepared by mechanosynthesis, in a similar approach reported by House et al. [94]. For this synthesis, Li₂O₂, MnO and LiF precursors were employed to obtain Li₂MnO_{3-x}F_x by mechanosynthesis at 750 rpm for 24 h. To avoid contamination as much as possible, a Fritsch Pulverisette 7 planetary ball mill was used within a 20 mL air-tight zirconia jar with 5 mm diameter zirconia balls. The precursors were weighed and sealed in zirconia jars in an argon filled glovebox with H₂O and O₂ less than 1 ppm. To prevent excessive heat generation, the milling process was undertaken in intervals of 5 minutes, followed by 10 minutes of rest.

Figure 3.4 (a) shows the XRD patterns obtained of the products after mechanosynthesis of Li₂MnO₃ (black), Li₂MnO_{2.8}F_{0.2} (red), Li₂MnO_{2.2}F_{0.8} (blue), Li₂MnO₂F (green), and Li₂MnO_{1.8}F_{1.2} (purple) at 750 rpm for 24 hours. The XRD pattern confirmed the successful synthesis of the compounds in a cubic rock salt structure in the *Fm-3m* space group. Compared to traditional solid-state methods, this synthesis involves a one-step high energy ball milling process conducted at room

temperature. As shown in the Figure 3.7 (a), the XRD pattern from synthesized samples exhibited a broadened peak with a noisy background, indicating these samples show low crystallinity with less ordering. The diffraction data reveal a shift in the peak positions to the left as the amount of fluorine is increased, highlighted in Figure 3.7 (b), which indicates an expansion in the lattice. From the lattice parameters, calculated using Bragg's law, it is found that a lattice parameter increases from 4.0823 to 4.1444 Å on moving from Li₂MnO₃ to Li₂MnO_{1.8}F_{1.2}.

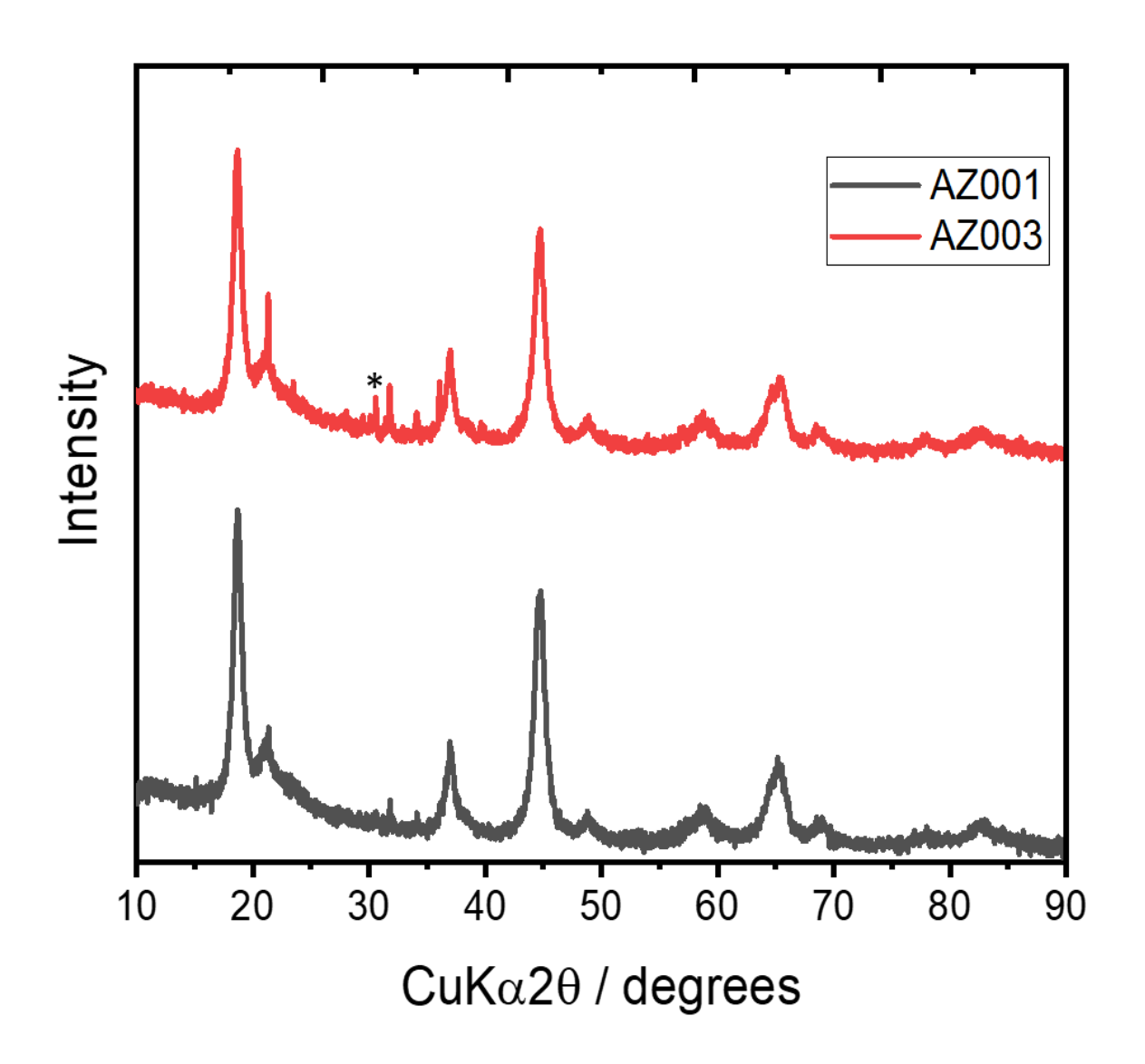


Figure 3.3 XRD patterns of the product during solid-state heat treatment of Li₂MnO₃ obtained at 450 °C based on ball milling time: 120 minutes (red) and 100 minutes (black).

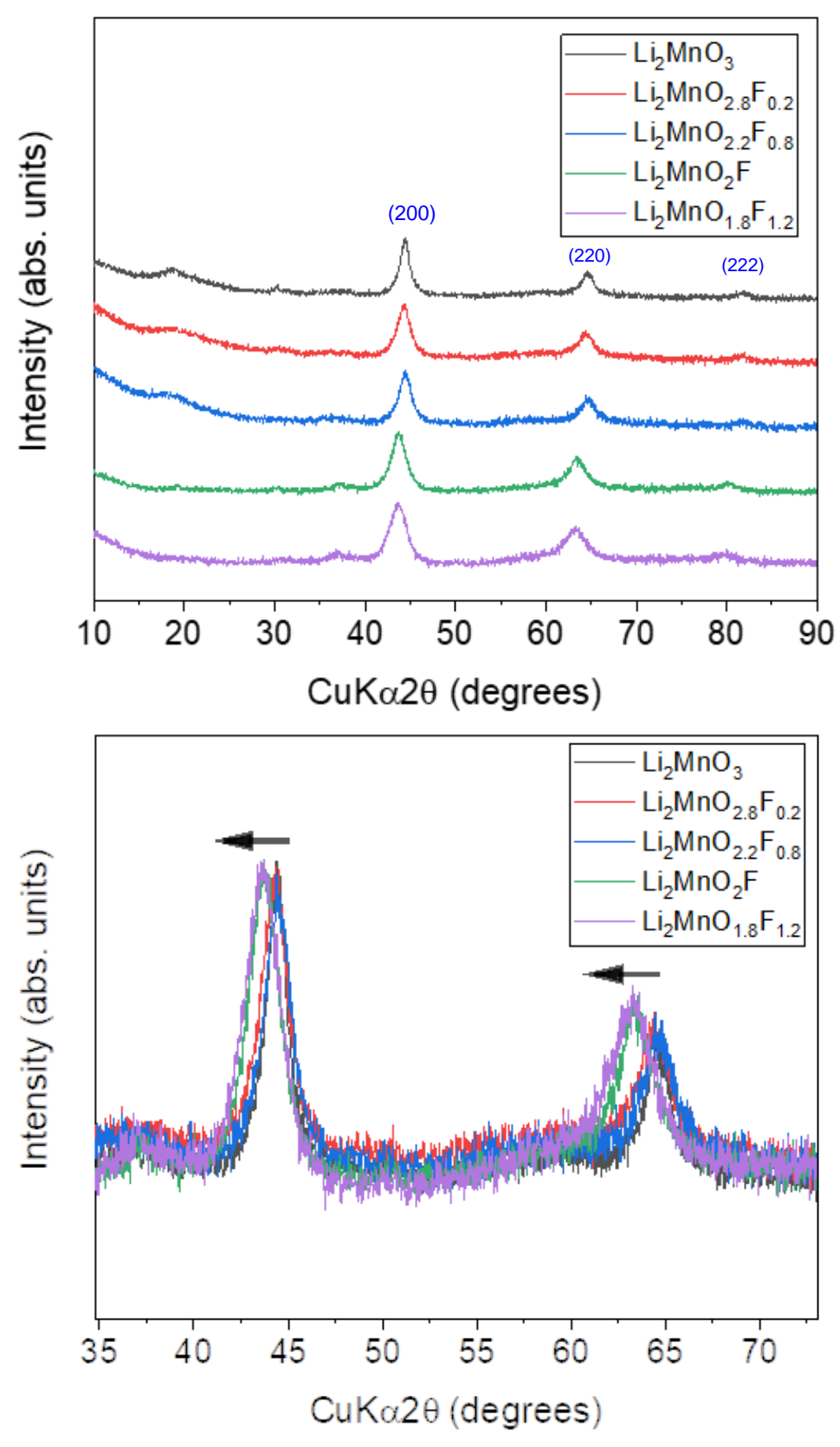


Figure 3.4 (a) XRD patterns of the product during mechanosynthesis of Li_2MnO_3 (black), $Li_2MnO_{2.8}F_{0.2}$ (red), $Li_2MnO_{2.2}F_{0.8}$ (blue), Li_2MnO_2F (green), and $Li_2MnO_{1.8}F_{1.2}$ (purple) at 750 rpm for 24 hours. (b) The extended region shows the peak shifting within 20 range of 35° and 75°.

3.2.2. Electrochemical performances of manganese-based cation-disordered rock salt Li₂MnO_{3-x}F_x (x=0, 0.2, 0.8, 1, 1.2) oxyfluoride cathodes for Li-ion batteries prepared using a mechanochemical synthesis.

Galvanostatic cycling with potential limitation (GCPL) was performed on the Li₂MnO₃, Li₂MnO_{2.8}F_{0.2}, Li₂MnO_{2.2}F_{0.8}, Li₂MnO₂F, and Li₂MnO_{1.8}F_{1.2} cation-disordered rock salt phases. To prepare the cathode pellets, each active cathode material was mixed with conductive carbon black and PTFE in a weight ratio of 60:20:20 (Active Material: Carbon Black: Binder) using a mortar and pestle for 30 minutes. Subsequently, the electrode sheets were calendered using a calendering roll pressure machine to minimize porosity on the electrode surface and enhanced particle contact [83, 84]. The calendered electrodes were kept in a vacuum drying oven at 80°C overnight to remove any moisture or other volatiles before transferring the electrodes into a glovebox. 2032-coin type cells were fabricated, with Li metal chips as the counter electrode and 1M LiPF₆ in EC: DMC (50:50 vol.%) as electrolyte in an Ar-filled glovebox. Coin cell measurements were carried out on a Maccor Battery Tester at room temperature. For the accurate evaluation of the experimental results, at least three-coin cells were fabricated from each sample. As shown in Appendix 3.1, the charge-discharge performance of each sample was evaluated at a constant current of 1 C between 2.0 V to 4.8 V vs. Li/Li⁺. According to their charge-discharge profiles, the best coin cell performances were selected based on repeatability and reproducibility and were further analysed.

Figure 3.5 displays the charge and discharge capacity curves obtained over 50 cycles from galvanostatic cycling for (a) Li₂MnO₃, (b) Li₂MnO_{2.8}F_{0.2}, (c) Li₂MnO_{2.2}F_{0.8}, (d) Li₂MnO₂F, and (e) Li₂MnO_{1.8}F_{1.2}. Most samples show a reduction in capacity with an increase in the number of cycles, with the exception of Li₂MnO_{1.8}F_{1.2}. This decline in capacity is commonly observed in lithium-ion battery cathodes and can be attributed to irreversible first cycle capacity loss due to factors such as electrode degradation, surface reactions, electrolyte decomposition and side reactions [99]. The voltage profile observed for Li₂MnO₃ (Figure 3.5(a)) exhibits a large plateau between approximately 4.4 V and 4.7 V during the first charge cycle. The initial charge capacity is 149 mAh g⁻¹, which decreases to 128 mAh g⁻¹ for the first cycle discharge capacity. As a result, the first cycle coulombic efficiency is calculated to be approximately 85%,

as depicted in Figure 3.6(a). The subsequent cycle exhibited rapid capacity fading with no apparent plateau, displaying 110 mAh g⁻¹ of charge capacity and 95 mAh g⁻¹ of discharge capacity. It should be noted that all Li₂MnO_{3-x}F_x samples presented here have been prepared in the same way and the coin cells assembled in the same way, i.e. none have been individually optimised at this stage. This is in order to (i) compare performance to identify trends and (ii) more efficiently down select to those most promising stoichiometries. It is therefore not surprising that the capacity for Li₂MnO₃ noted here is lower than some reports in the literature (129 mAh g⁻¹ versus >250 mAh g⁻¹). Further optimisation of synthesis and coin cell preparation is discussed in Chapter 4.

The corresponding differential capacity graph of Li₂MnO₃ is presented in Figure 3.7(a) and there is no observable oxidation peak until 4.4 V during the first charge cycle. After this point, a second sharp peak was observed at 4.7 V. These two peaks are likely related to lithium extraction and oxygen oxidation, which are likely occur randomly in the high voltage area. Compared to previous studies, similar differential capacity patterns were also observed during the first cycle for Li₂MnO₃ [100]. A reduction peak was observed at 3.2 V during the first discharge cycle which was not apparent on charge. It is likely this redox activity results from some irreversible phase change which occurred on charge. In the second cycle, there is one peak observed between 4.4 V and 4.8 V in the charge profile, which indicates some irreversible change has occurred during this second cycle. Again, a noticeable oxidation peak appears at 3.3 V, and a reduction peak is observed at 3.2 V.

In contrast to the Li₂MnO₃ parent phase, the first charge cycle for Li₂MnO_{2.8}F_{0.2} (Figure 3.5(b)) did not exhibit any obvious plateau lines, with a charge capacity of only 86 mAh g⁻¹ followed by a discharge capacity of 69 mAh g⁻¹. Compared to other samples, it showed the smallest irreversible capacity reduction of 20 mAh g⁻¹ with a coulombic efficiency of 81% in the first cycle, as shown in Figure 3.6 (b). In the subsequent cycles, it displays stable cycling behaviour with charge and discharge capacity retentions of > 95%. Such stable cycling behaviours over cycles is highly desirable and it is evident that the partial replacement of oxygen (O) lattice with fluorine (F) represents an effective approach to enhance the electrochemical stability. The differential capacity graph of Li₂MnO_{2.8}F_{0.2} is presented in Figure 3.7 (b), and there is no oxidation peak

until 4.4 V during the first charge cycle. In contrast to Li_2MnO_3 , the partial substitution of F into oxygen lattice appears to switch on reduction of the Mn^{4+} oxidation state to Mn^{3+} , with this oxidation process likely contributing to the first cycle capacity. As can be seen from the graph, the peak that is presumed to belong to the anionic redox at 4.6 V and with cathodic redox at 4.3 V is also reversible in the second cycle.

The charge-discharge profiles of Li₂MnO_{2.2}F_{0.8} (Figure 3.5(c)) and Li₂MnO₂F (Figure 3.5(d)) exhibit similar patterns. They exhibit an initial charge capacity of 195 mAh g⁻¹ and 187 mAh g⁻¹, respectively, along with first-cycle discharge capacities of 143 mAh g⁻¹ for each. This indicates coulombic efficiencies of 73 % and 76 % respectively as shown in Figure 3.6 (c) and (d). There are several reasons why electrodes exhibit such low coulombic efficiency values during the initial cycles, especially when operated in the high voltage range. The formation of solid electrolyte interphase (CEI) can lead to electrode degradation result of undesirable side reactions. The charge capacities of 145 mAh g⁻¹ and charge-discharge capacity retentions in the second cycle of higher than 90 % were calculated for each. Differential capacity plots (Figure 3.7 (c) and (d)) for both F=0.8 and F=1.0 samples show similar profiles, where broad peaks between 3.2 V and 3.6 V are attributed to Mn-redox and the second peak in the first charge cycle at higher voltage is attributed to oxygen redox. Over the 50 cycles measured, Li₂MnO₂F displays the best capacity retention of all samples prepared (~120 mAh g⁻¹); therefore, this stoichiometry was selected for optimisation in Chapter 4.

Figure 3.5 (e) shows the charge-discharge profiles corresponding to the $Li_2MnO_{1.8}F_{1.2}$. It exhibited an initial charge capacity of 146 mAh g⁻¹ and a discharge capacity of 84 mAh g⁻¹. It showed the lowest coulombic efficiency of 58 % compared to other samples, as shown in Figure 3.6 (e). With increased fluorination substitution, a significant, irreversible loss of capacity occurred in the first cycle. The differential capacity graph of $Li_2MnO_{1.8}F_{1.2}$ is indicated in Figure 3.7 (e).

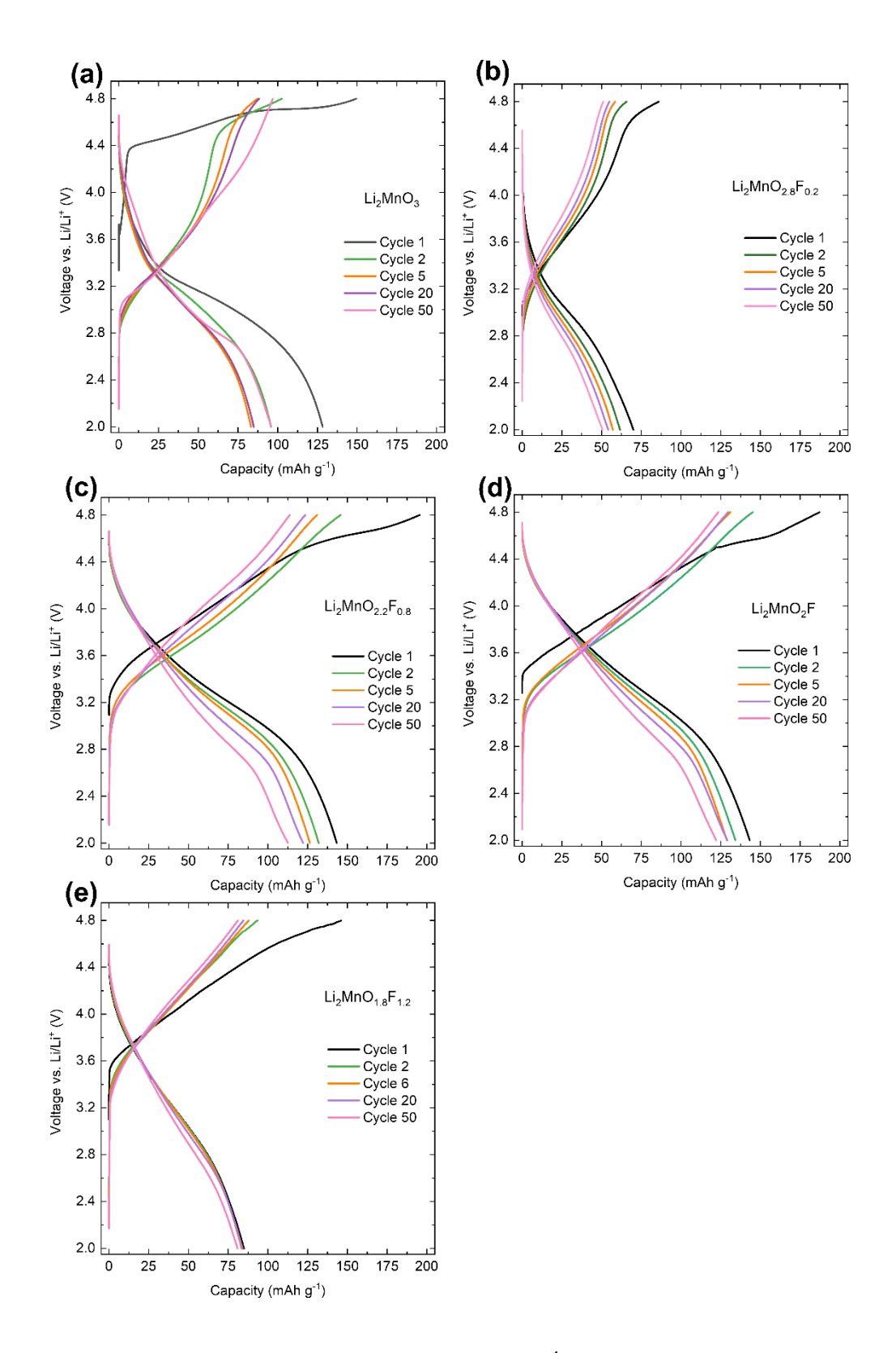


Figure 3.5 The charge-discharge capacity (mAh g⁻¹) vs. voltage (V) curves obtained from galvanostatic cycling over 50 cycles at room temperature of the $Li_2MnO_{3-x}F_x$ pellets (active material: carbon black: PTFE in a 60:20:20) (a) Li_2MnO_3 , (b) $Li_2MnO_{2.8}F_{0.2}$, (c) $Li_2MnO_{2.2}F_{0.8}$, (d) Li_2MnO_2F , and (e) $Li_2MnO_{1.8}F_{1.2}$. 2032-coin type cells were cycled between 2 – 4.8 V vs. Li/Li^+ at a rate of 1 C.

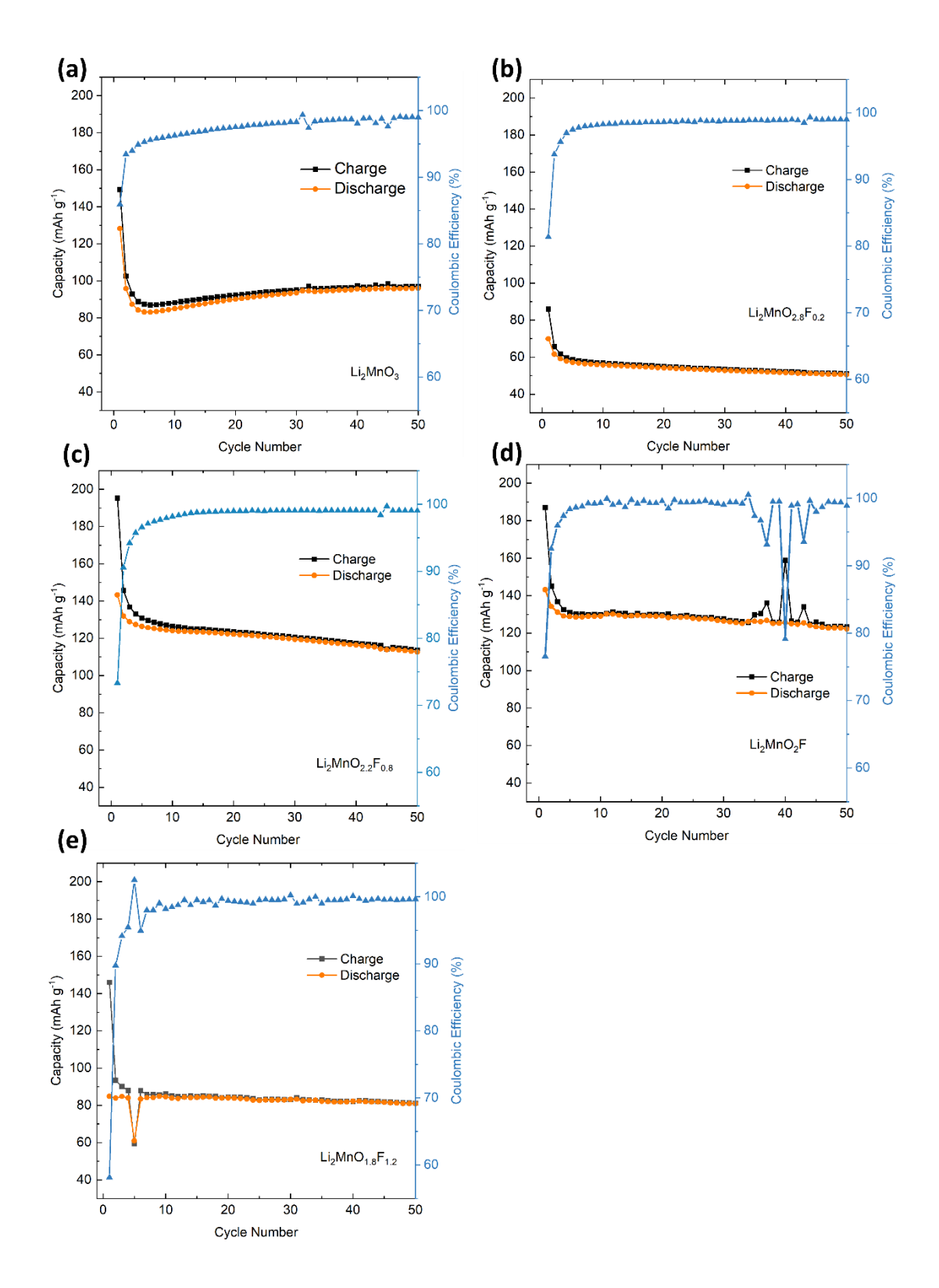


Figure 3.6 The charge-discharge capacity (mAh g⁻¹) and coulombic efficiency (%) vs. cycle number obtained from galvanostatic cycling over 50 cycles at room temperature of the Li₂MnO_{3-x}F_x pellets (active material: carbon black: PTFE in a 60:20:20) (a) Li₂MnO₃, (b) Li₂MnO_{2.8}F_{0.2}, (c) Li₂MnO_{2.2}F_{0.8}, (d) Li₂MnO₂F, and (e) Li₂MnO_{1.8}F_{1.2}. 2032-coin type cells were cycled between 2 – 4.8 V vs. Li/Li⁺ at a rate of 1 C.

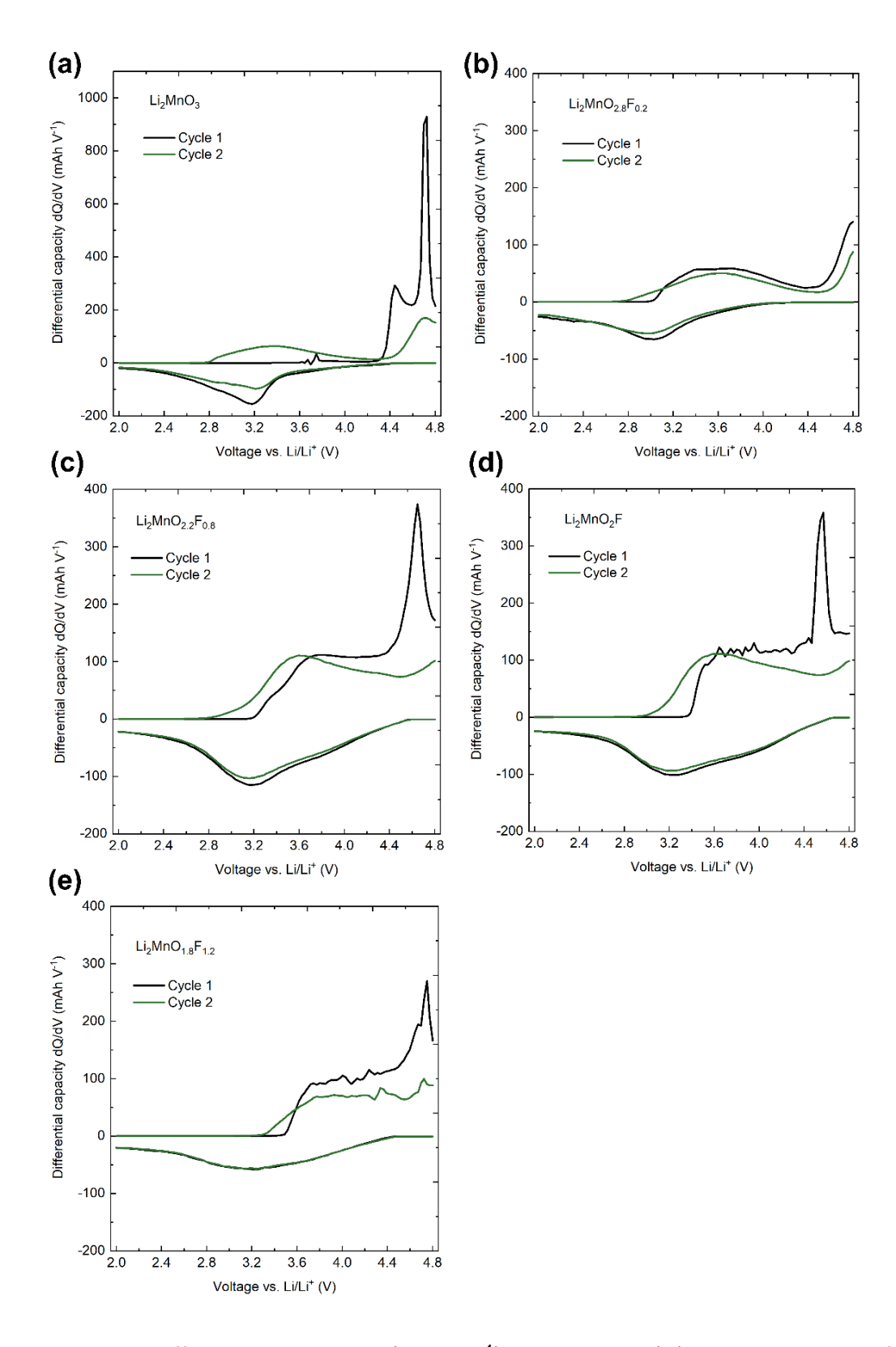


Figure 3.7 The differential capacity (mAh V⁻¹) vs. voltage (V) graph obtained from galvanostatic cycling only two cycles at room temperature of the $Li_2MnO_{3-x}F_x$ pellets (active material: carbon black: PTFE in a 60:20:20) (a) Li_2MnO_3 , (b) $Li_2MnO_{2.8}F_{0.2}$, (c) $Li_2MnO_{2.2}F_{0.8}$, (d) Li_2MnO_2F , and (e) $Li_2MnO_{1.8}F_{1.2}$. 2032-coin type cells were cycled between 2 – 4.8 V vs. Li/Li^+ at a rate of 1 C.

3.2.3. Local Lithium diffusion studies on manganese-based cation-disordered rock salt Li₂MnO_{3-x}F_x (x=0, 0.2, 0.8, 1, 1.2) oxyfluoride cathodes by muon spin spectroscopy (μ^+ -SR)

The efficient movement of lithium ions (Li⁺) within the electrodes and electrolyte plays vital role in enhancing the performance of lithium-ion batteries. Fast charging is essential for next generation LIBs and the fundamental requirements for this rely of rapid ion diffusion at the site-site level. The ability to achieve faster diffusion of ions at lower temperature is particularly beneficial for batteries, especially in electric vehicle applications. This is crucial because the performance of batteries can be restricted by lower temperatures experienced during different seasons and in various regions. Therefore, the measurement of ionic diffusion dynamics and kinetics in electrode materials is crucial aspect of material analysis. In this work, the μ +-SR technique was utilized to investigate the microscopic diffusivity behaviour of Li⁺ ions in the F-doping samples, which were prepared using a high-energy ball milling method.

The µ+-SR experiments were carried out using the EMU and MuSR instrument at the ISIS Neutron and Muon Source. The measurements were undertaken at three different beamtime periods. The analysis of powered samples was conducted using a titanium sample holder due to its low background. Titanium has no nuclear magnetic moment and thus any stray muons will not provide a relaxing signal which could interfere with the signal obtained from the sample. Muon spin spectroscopy measurements were conducted on various cathode materials, including the F-doped Li₂MnO₃ (F=0), Li₂MnO_{2.8}F_{0.2} (F=0.2), Li₂MnO_{2.2}F_{0.8} (F=0.8), Li₂MnO₂F (F=1), and Li₂MnO_{1.8}F_{1.2} (F=1.2). The measurements were carried out within temperature ranges of 100 to 500 K under both zero field (ZF) and applied longitudinal fields (LF) of 10 and 20 Gauss. Longitudinal fields are applied to gradually decouple the muon from its local nuclear fields and hold the muon position in the field direction. Fitting three fields simultaneous at a single temperature therefore provides a reliable interpretation of Li⁺ diffusion.

Figure 3.8 shows the time evolution of the decay positron asymmetry at 300 K (room temperature) under 0 Gauss (black), 10 Gauss (blue), and 20 Gauss (orange) for the raw data (a) Li₂MnO₃, (b) Li₂MnO_{2.8}F_{0.2}, (c) Li₂MnO_{2.2}F_{0.8}, (d) Li₂MnO₂F, and (e) Li₂MnO_{1.8}F_{1.2}. The solid lines in each field represent the fitting of the data using the dynamic Kubo-Toyabe function for the compounds. The samples displayed a slightly

different background fractions because of difference in the experimental conditions during multiple beamtimes. The samples of Li₂MnO_{2.8}F_{0.2} and Li₂MnO₂F were measured with MuSR instrument, while the other samples were measured with the EMU instrument. Therefore, a direct comparison between the raw data is difficult. However, each sample exhibited a similar behaviour in the decay positron asymmetry. It is clearly observed from Fig. 3.8 that the form of the zero field in each compound has asymmetry fast relaxation in the decay positron asymmetry. All samples deviate from static Kubo-Toyabe behaviour, indicating a dynamic contribution from the movement of Li⁺ at 300 K. With an increase in the applied field, the decay positron asymmetry shows a slower relaxation in decay positron asymmetry, as expected. Initially, the positron decay asymmetry shows a quick relaxation and then it displays a much slower relaxation process. The initial relaxation can mostly be considered as independent form the applied magnetic field, and mostly originates from the electronic field present from the d-electrons in Mn. The slower relaxation at longer timescales likely originates from the muon spin interaction with internal nuclear fields, which are usually weaker than electronic fields. In each sample, there is remarkably similar fast relaxation observed for approximately ~1.5 µs (shown in Figure 3x.2). This initial relaxation can mainly be attributed to the interaction between muon spin and the delectrons. The presence of Mn^{3+} (d^4 , t_{2g}^3 e_g^1) and Mn^{4+} (d^3 , t_{2g}^3 e_g^0) ions significantly influences this first relaxation due to their unpaired 3d electrons and paramagnetic characteristics. After ~1.5 µs in each sample, another relaxation occurred. This slower relaxation arises from the interaction between the collective spins of muon and the magnetic moment of nearby atomic isotopes with non-zero spin such as 6Li (7.6 % abundance), 7Li (92.4 % abundance), 55Mn (100 % abundance), 17O (0.03 % abundance), and 19F (100 % abundance). Although the muon likes to reside near O sites, the oxygen ions do not significantly influence the muon spin due to the low abundance on non-zero nuclear moment nuclei [101]. The decay positron plots of each sample show that the dynamic behaviour of Li+ ions, with decrease in relaxation rate from low temperature (shown in Appendix A) to room temperature (Figure 3.8). In comparison to F-doping samples at zero-field, from Li₂MnO₃ to Li₂MnO_{1.8}F_{1.2} samples show a more robust static Kubo-Toyabe type relaxation at 300 K, which may be due to the slower Li+ diffusion in these samples at this temperature. At the applied longitudinal fields of 10 G and 20 G, the relaxation rate in each sample is decreased

due to the increasing decoupling of the muon spin interaction with its nearby nuclear environment.

To examine the dynamics of Li⁺ diffusion in these samples, the data were collected across the temperature range of 100 K to 500 K using zero field and the longitudinal fields at 10 G and 20 G. The Li₂MnO₃ and Li₂MnO_{2.8}F_{0.2} were measured within a temperature range of 200 K to 500 K, with increments of 20 K. The sample of Li₂MnO_{2.2}F_{0.8} was measured within a temperature range of 100 K to 200 K, with increments of 20 K, and then from 200 K to 400 K, with increments of 10 K. Li₂MnO₂F was measured within a temperature range of 100 K to 500 K, with increment of 20 K. Li₂MnO_{1.8}F_{1.2} was measured within a temperature range of 100 K to 400 K, with an increment of 20 K. The raw data at various temperatures were used to fit the data using the Mantid software, employing equation 3.1. This equation contains several terms to describe the trend of polarisation P_{LF} with initial amplitude A_0 over time t, including (a) exponentially relaxing term to consider interactions with 3d magnetic moments from initial fast relaxation, with a rate λ_{F} , (b) a dynamic Kubo-Toyabe function to give information about the behaviour of diffusing Li⁺, which is dependent on time (t), the local field distribution at the muon stopping location (Δ), the field fluctuation rate (ν) , and the applied field (H_{LF}) . The last component used was (c) a flat background amplitude (A_{BG}).

$$A_{0} P_{LF} (t) = A_{F} e^{-\lambda_{F} t} + A_{KT} G^{DGKT} (\Delta, \nu, t, H_{LF}) + A_{BG}$$
(a) (b) (c)

The obtained parameter from the fitting process gives valuable information about Li⁺ diffusion in these samples. Figure 3.9 displays the temperature dependence of the ν and Δ parameters across the measured temperature range. The field fluctuation rate (ν) gives information on the Li⁺ hopping rates for Li⁺ diffusion. As the temperature rises, these rates start to increase gradually, which can be related to the gradually rise in thermally induced Li⁺ diffusion. For Li₂MnO₃ and Li₂MnO_{2.8}F_{0.2}, the ν values exhibit a steady plateau from 200 K to 280 K. After 280 K, the ν values of both samples gradually increase from 280 K to 500 K. While this increase reaches ~0.25 MHz for Li₂MnO₃, it is measured as ~0.20 MHz for Li₂MnO_{2.8}F_{0.2} at the end temperature point.

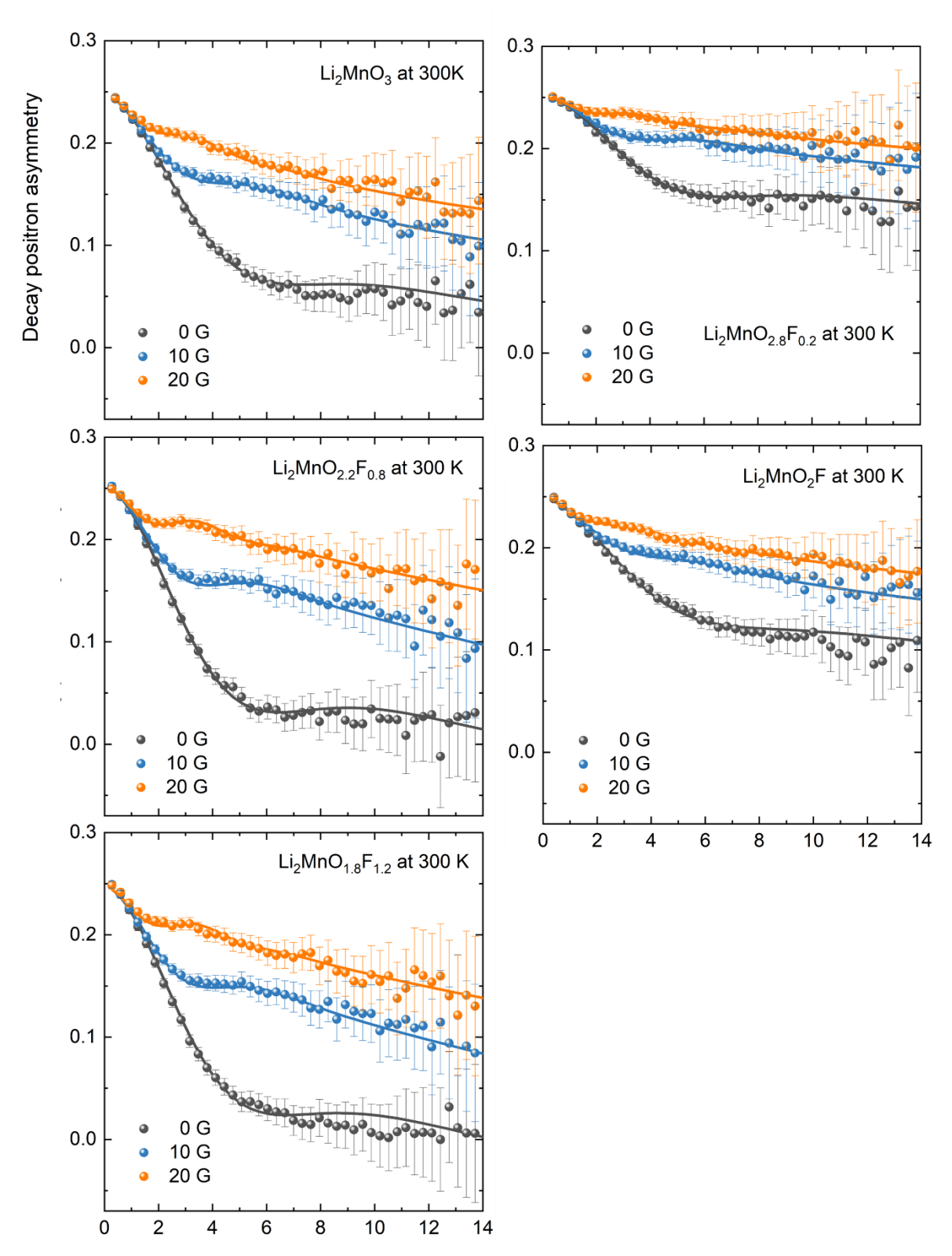


Figure 3.8 Raw data for μ +-SR measurement at 300 K under zero field (black), longitudinal fields of 10 G (blue), and 20 G (orange). The solid lines represent the fitting of the data using the dynamic Kubo-Toyabe function for (a) Li₂MnO₃, (b) Li₂MnO_{2.8}F_{0.2}, (c) Li₂MnO_{2.2}F_{0.8}, (d) Li₂MnO₂F and (e) Li₂MnO_{1.8}F_{1.2}.

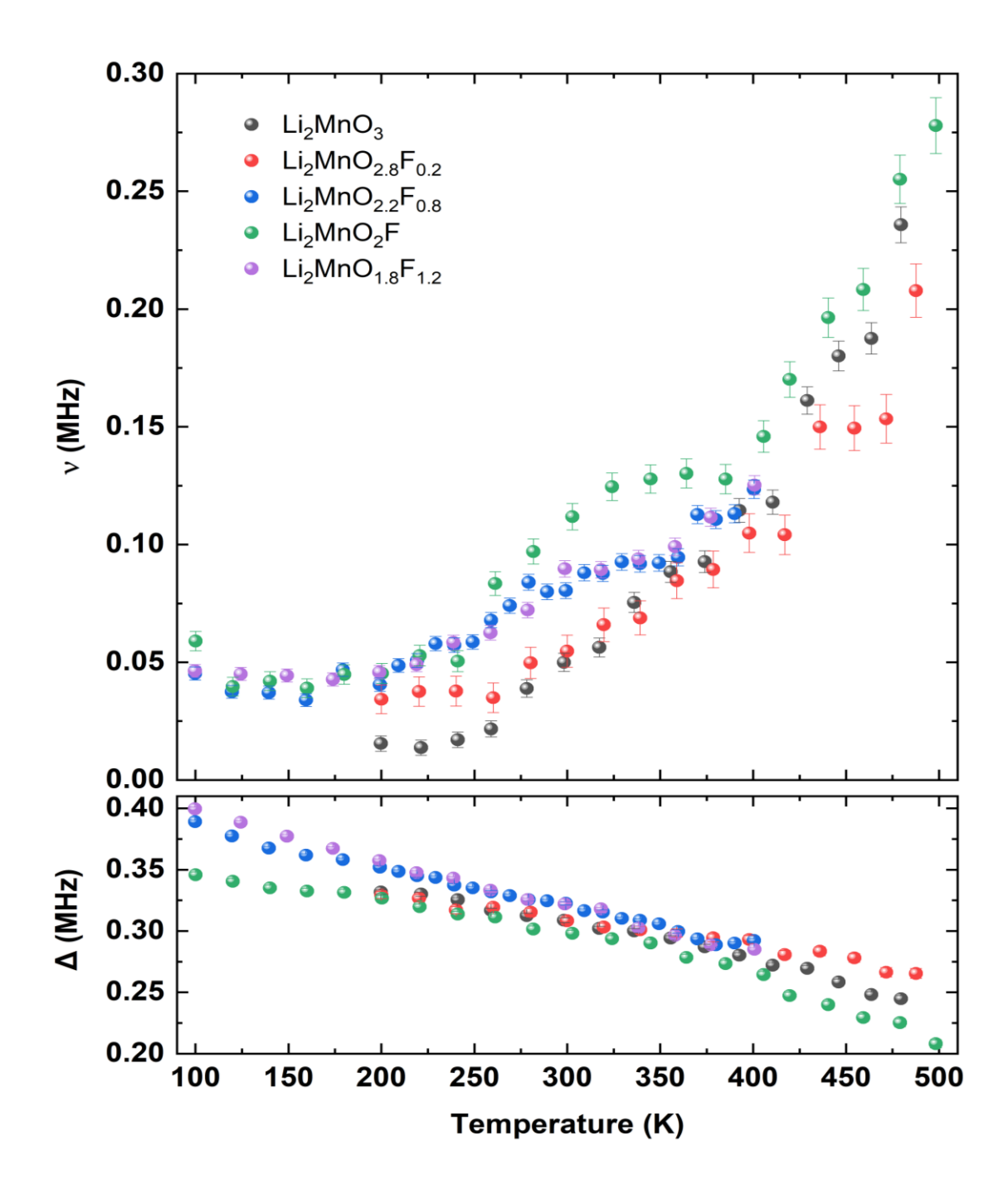


Figure 3.9 Temperature dependence of (a) the field fluctuation rate (ν) and (b) the local field distribution (Δ) obtained from fitting the μ⁺-SR data using the dynamic Kubo-Toyabe function for : Li₂MnO₃ (black) and Li₂MnO_{2.8}F_{0.2} (red) measured from 200 K to 500 K, with increments of 20 K. Li₂MnO_{2.2}F_{0.8} (blue) measured from 100 K to 200 K, with increments of 20 K, and then from 200 K to 400 K, with increments of 10 K. Li₂MnO₂F (green) measured from 100 K to 500 K, with increment of 20 K. The Li₂MnO_{1.8}F_{1.2} (purple) measured from 100 K to 400 K, with an increment of 20 K.

It is noted that measurement on the Li₂MnO₃ and Li₂MnO_{2.8}F_{0.2} began at 200 K instead of the usual at 100 K for other samples. The reason for this was the limited time available on the μ^+ -SR beamline. For Li₂MnO_{2.2}F_{0.8}, Li₂MnO₂F, and Li₂MnO_{1.8}F_{1.2}, the ν values display a steady plateau in the low-temperature region, indicating little Li⁺ dynamics. The value of ν in Li₂MnO_{2.2}F_{0.8} gradually starts to increase from around 200 K to 400 K, while in Li₂MnO_{1.8}F_{1.2} a similar gradual increase is observed from 220 K to 400 K. The field fluctuation rate in Li₂MnO₂F starts to increase from 240 K to 500 K. This is significantly much sharper than the behaviour seen in F-doping samples, where the ν value increases at high temperature.

The relationship between temperature and the local field distribution width (Δ) in each sample is shown in Figure 3.9. As the temperature rises, the Δ value often exhibit a steady decrease for all samples. The Δ value for Li₂MnO₃ and Li₂MnO_{2.8}F_{0.2} commences at around 0.32 MHz and 0.33 MHz at 200 K, respectively. These samples show a consistent trend of decreasing steadily from 0.31 MHz to 0.25 MHz within the temperature range of 280 K to 500 K, where thermal activation occurs. The Δ value for Li₂MnO₂F starts at around 0.34 MHz at 100 K, showing a steady decrease with increasing temperature and steady values between 240 K to 500 K, where the thermal activation takes place. However, the Li₂MnO_{2.2}F_{0.8} and Li₂MnO_{1.8}F_{1.2} samples show higher values at 100 K with approximately 0.38 MHz and 0.39 MHz respectively, which are noticeably larger than the other samples. The thermally active region for Li₂MnO_{2.2}F_{0.8} ranges from 200 K to 400 K, while for Li₂MnO_{1.8}F_{1.2} it ranges from 220 K to 400 K.

The activation energy (E_a) for Li⁺ diffusion can be calculated via the Arrhenius equation as shown in Equation 3.2:

$$\ln (v) = \frac{-E_a}{K_B T} + \ln (A)$$
 (3.2)

where v is the field function rate, T is the temperature, K_B is the Boltzmann constant (is equal to 1.3806488 x 10²³ J K⁻¹), and A value is a pre-exponential factor.

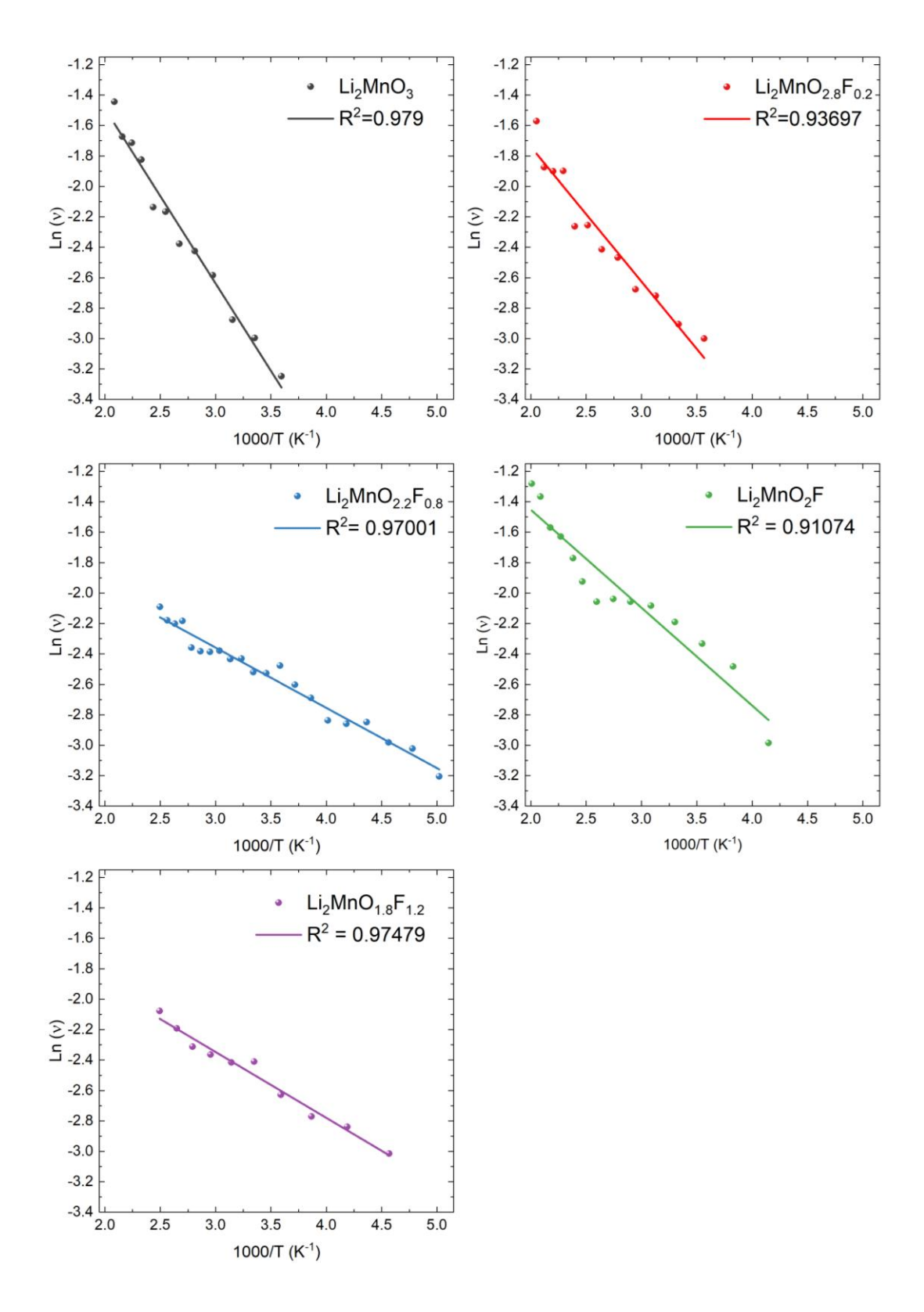


Figure 3.10 Arrhenius plot of the field fluctuation value (ν) within the thermally activated area displayed from μ^+ -SR data using the dynamic Kubo-Toyabe function for: (a) Li₂MnO₃ (black), (b) Li₂MnO_{2.8}F_{0.2} (red), (c) Li₂MnO_{2.2}F_{0.8} (blue), (d) Li₂MnO₂F (green), and (e) Li₂MnO_{1.8}F_{1.2} (purple).

According to the equation, the activation energy (E_a) can be determined by analysing the slope of the linear fit on the plot of $\ln (v)$ versus 1/T. To obtain the activation energy, Ea, for ionic diffusion, the thermal activated region used for all samples is shown in Figure 3.10. For Li₂MnO₃ and Li₂MnO_{2.8}F_{0.2}, the temperature range of 280 K to 500 K was analysed. Li₂MnO_{2.2}F_{0.8} was evaluated within 200 K to 400 K. Li₂MnO₂F was analysed within 240 K to 500 K. Li₂MnO_{1.8}F_{1.2} was calculated within 220 K to 400 K. Table 3.1 lists the obtained activation energies for all samples. The activation energies for various these samples were found as follows: Li₂MnO₃ exhibited an activation energy of around 99.05 meV, Li₂MnO_{2.8}F_{0.2} showed an activation energy of approximately 76.35 meV. Li₂MnO_{2.2}F_{0.8} displayed an activation energy of around 34.13 meV. Li₂MnO₂F demonstrated an activation energy of approximately 50.26 meV. For Li₂MnO_{1.8}F_{1.2}, the activation energy was 37.32 meV. The highest activation energy is observed for Li₂MnO₃ and is similar to values obtained for other cathode materials [102]. The activation energy then decreases on a small amount of F doping (e.g. F=0.2). This trend continues towards higher fluorine content, from F=0.8 to F=1.2. These results indicate that F doping successfully enables Li hopping through the structure. Typically, µ+-SR measurements give lower values for activation energy compared to techniques such as EIS, as µ+-SR is not as affected by grain boundaries or surface layers [103].

Table 3.1 Activation energies calculated over the thermally activated region using the Arrhenius equation from μ+-SR data using the dynamic Kubo-Toyabe function for Li₂MnO₃, Li₂MnO_{2.8}F_{0.2}, Li₂MnO_{2.2}F_{0.8}, Li₂MnO₂F, and Li₂MnO_{1.8}F_{1.2}.

Composition	Thermal activated region	Slope	Activation Energy, E _A
Li ₂ MnO ₃	280 K – 500 K	-1.14943 ± 0.05323	99.05 ± 4.587 meV
Li ₂ MnO _{2.8} F _{0.2}	280 K – 500 K	-0.88597 ± 0.06907	76.35 ± 5.952 meV
Li ₂ MnO _{2.2} F _{0.8}	200 K – 400 K	-0.39615 ± 0.01556	34.13 ± 1.341 meV
Li ₂ MnO ₂ F	240 K – 500 K	-0.6434 ± 0.05565	50.26 ± 4.795 meV
Li ₂ MnO _{1.8} F _{1.2}	220 K – 400 K	-0.43307 ± 0.02318	37.32 ± 1.997 meV

Understanding the pathways through which Li⁺ ions move within the structure is crucial for determining the lithium diffusion coefficient. To calculate the diffusion coefficients (D_{Li}), the equation 3.3 was used for μ^+ -SR data. In this equation, N_i represent the number of possible diffusion pathways that are accessible in the specific structure being considered. $Z_{v,i}$ denotes the vacancy fraction of the destination site, while s_i represents the distance of the lithium jump. The parameter ν corresponding to the field fluctuation rate, which is derived from the fitting of experimental data [103].

$$D_{Li} = \sum_{i=1}^{n} \frac{1}{N_i} Z_{\nu,i} \, s_i^2 \nu \tag{3.3}$$

To calculate the diffusion coefficients, various assumptions have been made. The N_i , where is the number of lithium site, was assumed as 8 because Li^+ ion migration occurs via 0-TM channels with o-t-o diffusion [48, 104] . The $Z_{v,i}$ value is taken as 1 as the hopping pathway was determined as site to interstitial, while the value of s_i was calculated via lattice parameters. The ν corresponding to the field fluctuation rate and was taken from the μ^+ -SR data at the appropriate temperature. Table 3.2 gives the diffusion coefficient values calculated for all samples measured.

Table 3.2 Diffusion coefficient calculated at 300 K from equation 3.3.

Composition	Diffusion Coefficient, D _{Li} (cm ² s ⁻¹)	
Li ₂ MnO ₃	6.9250 × 10 ⁻¹²	
Li ₂ MnO _{2.8} F _{0.2}	7.6134×10^{-12}	
Li ₂ MnO _{2.2} F _{0.8}	1.1179 × 10 ⁻¹¹	
Li ₂ MnO ₂ F	1.5999 × 10 ⁻¹¹	
Li ₂ MnO _{1.8} F _{1.2}	1.2880 × 10 ⁻¹¹	

3.3. Conclusion

This chapter details the mechanochemical synthesis of Li₂MnO_{3-x}F_x (x=0, 0.2, 0.8, 1, 1.2) which involves the partial substitution of fluorine into oxygen. These materials were characterised by X-ray diffraction, electrochemical cycling in half coin cells and muon spin spectroscopy (μ^+ -SR). The results here indicate that the best electrochemical performance is observed for Li₂MnO₂F and this sample was selected for further optimisation in Chapter 4.

Chapter 4: Optimising the synthesis and electrochemical performance of Li₂MnO₂F cation disordered rock salt cathodes

4.1. Introduction

Results from Chapter 3 have demonstrated the cation disordered rock salt type oxyfluoride Li₂MnO₂F has promise as a high energy density cathode for lithium-ion batteries. However, the oxyfluoride cathodes still exhibit rapid material degradation and poor capacity retention, which limits commercial applications [67]. Many lithium-ion cathode reports presented in the literature suggest that performance is not only limited to the material level, but also depends heavily on electrode fabrication and cell manufacturing processes [105-107]. There have been reported studies on oxygen redox induced degradation and the voltage hysteresis for cation disordered rock salt cathodes [108, 109]. Among them, Mn-based oxyfluoride cathodes have been successfully synthesized using mechanochemical synthesized [94]. Lun et al. reported how the Li percolation and Mn redox mechanism for Mn-based cation disordered rock salt cathode changes depending on F substitution of oxygen along with mechanochemical [96].

This chapter provides a comprehensive work on the mechanochemical synthesis conditions of Li₂MnO₂F, including optimising ball milling time, and optimising starting materials for synthesis, alongside structural, morphological and electrochemical characterisation. This chapter also includes research on selecting binder particle size and optimising carbon/binder/active material ratio in order to enhance electrode capacity and demonstrates how this can improve stability during the cycling of the obtained Li₂MnO₂F.

4.2. Result and Discussion

4.2.1. Optimising ball milling time for Li₂MnO₂F synthesis

Mechanochemical synthesis depends on mechanical milling to enable chemical reactions between solid precursors. High-speed milling supplies more energetic collisions, which leads to more effective milling performance and a quicker reduction

in particle size. However, high-speed milling lead to increases in local heat production and can also lead to contamination of the final product (e.g. through the use of stainless steel jars). Depending on the milling time, the reactants can interact effectively with each other and effectively reduce the final particle size. Moreover, the ball milling time may cause differences in particle morphology [110]. Therefore, the milling time, speed and milling media are crucial parameters to a successful and effective chemical reaction [111-113]. This thesis uses zirconia jars and balls to prevent contamination due to this being chemically inert and non-reactive [114]. To avoid heat production, a ten-minute rest break was taken after every five minutes of ball milling. In this context, the effect of ball milling time for Li₂MnO₂F was investigated. For this synthesis, Li₂O₂, MnO and LiF precursors were employed to obtain Li₂MnO₂F by mechanosynthesis at 750 rpm during three different ball milling times: 18 hours, 24 hours, and 36 hours. The same synthesis conditions as in section 2.3.2.2 were used.

Figure 4.1 shows the XRD patterns obtained of the products after mechanosynthesis of Li₂MnO₂F at 750 rpm for 18 hours (black), 24 hours (red), and 36 hours (blue). The XRD pattern for each sample is characterised by three peaks which correspond to the main peaks in Li₂MnO₃. Both the layered (*C*2/*m*) and cubic (*Fm-3m*) models have been used to describe diffraction data relating to ball-milled Li₂MnO₃ samples [98, 115]. As shown in the Figure 4.1 (a), the XRD pattern from synthesized samples exhibit broad peaks with a noisy background, indicating these samples show low crystallinity with less ordering. A decrease in the intensity of the peaks was observed for 36-hours long duration ball mill operation. As shown in Figure 4.1 (b), the samples obtained from 36 hours ball mill displays a slight peak shift to the right. From the lattice parameters, calculated using Bragg's law, it is found that a lattice parameter for 18 hours, 24 hours, and 36 hours are 4.1106 Å, 4.1358 Å, and 4.1016 Å, respectively. Brunauer-Emmett-Teller (BET) analysis was performed to observe the morphological effect of ball milling time for Li₂MnO₂F. Low ball milling (18 hours) and high ball milling (36 hours) samples were selected for analysis. Figure 4.2 shows the nitrogen adsorption and desorption isotherms of Li₂MnO₂F for 18 hours and 36 hours samples from BET measurement. Their specific surface area was calculated as 10 m² g⁻¹ and 9 m² g⁻¹, respectively, indicating that ball milling time beyond 18 hours had little effect on the resultant surface area.

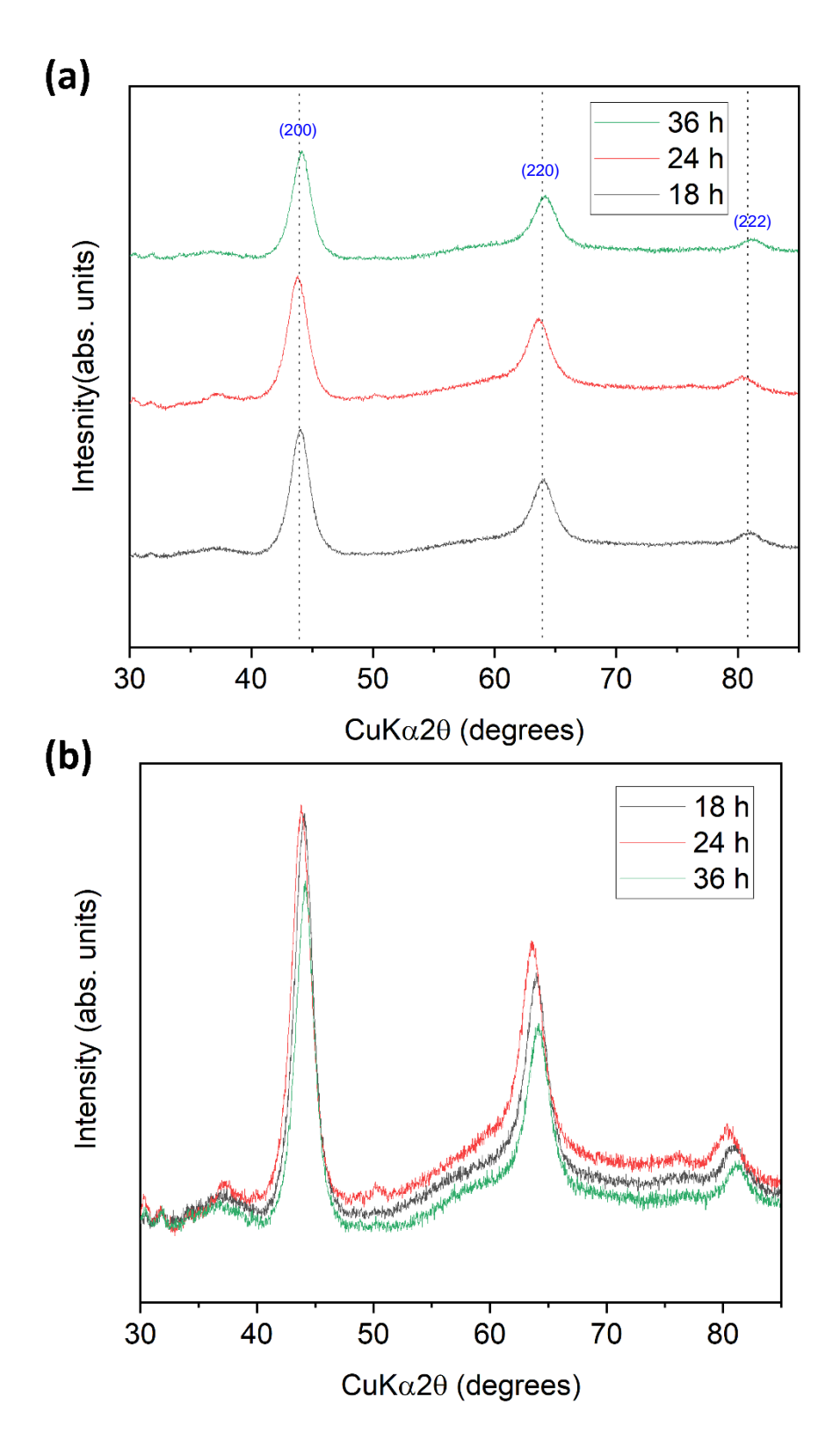


Figure 4.1 a) XRD patterns of the product during mechanosynthesis of Li₂MnO₂F at 750 rpm for 18 hours (black), 24 hours (red), and 36 hours (green) b) The highlighted region shows peak shifting.

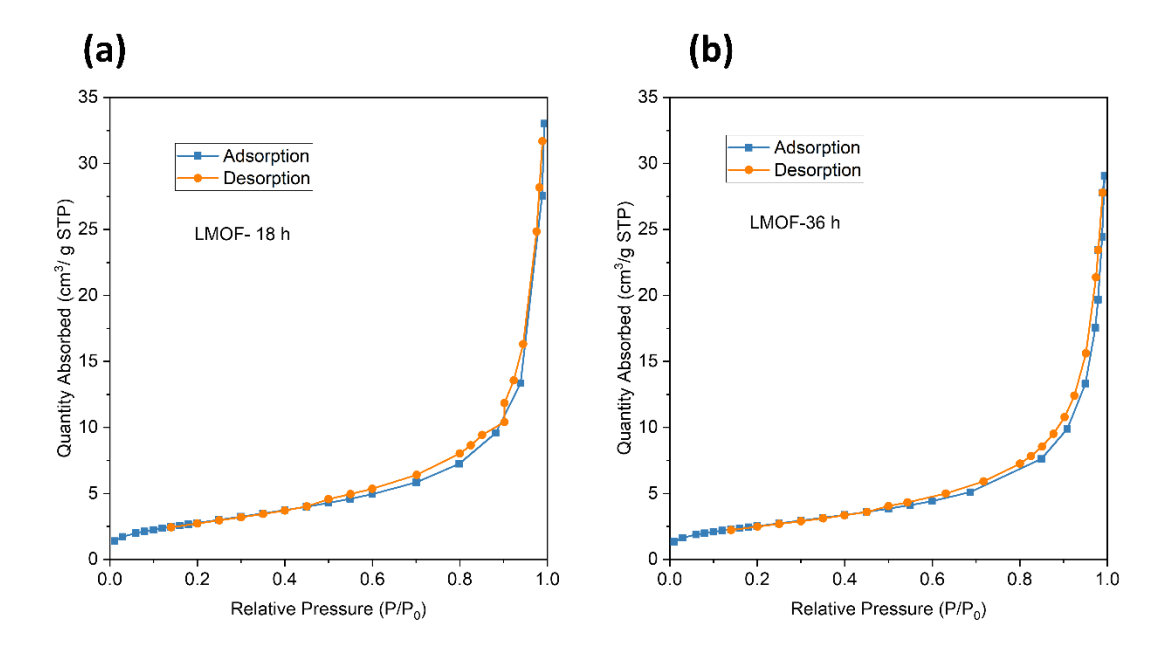


Figure 4.2 The nitrogen adsorption and desorption isotherms of Li₂MnO₂F samples at 77 K on (a) LMOF-18h, and (b) LMOF-36h were measured.

Traditional X-ray diffraction methods rely on an extended long-range order in the material under examination giving rise to Bragg reflections in the resulting patterns obtained. Given the lack of long range order in these disordered materials, traditional X-ray diffraction methods can be limited in assessing any local order which may persist. The atomic pair distribution function (PDF) can provide additional insights into local order, providing a weighted histogram of the atom-atom distances present in real space. These total scattering experiment were conducted, in collaboration with Dr Xiao Hua at Lancaster University, to examine the local structure for the obtained Li₂MnO₂F. Figure 4.3 shows the experimental and calculated atomic pair distribution function profiles, G(*r*), for Li₂MnO₂F samples obtained for 18, 24 and 36 hour ball-milling. The most satisfactory fit obtained was from using the *C2/m* space group to describe the local order in this disordered rock salt material. This is in good agreement with previous reports in literature for local ordering in Li₂MnO₃ [115].

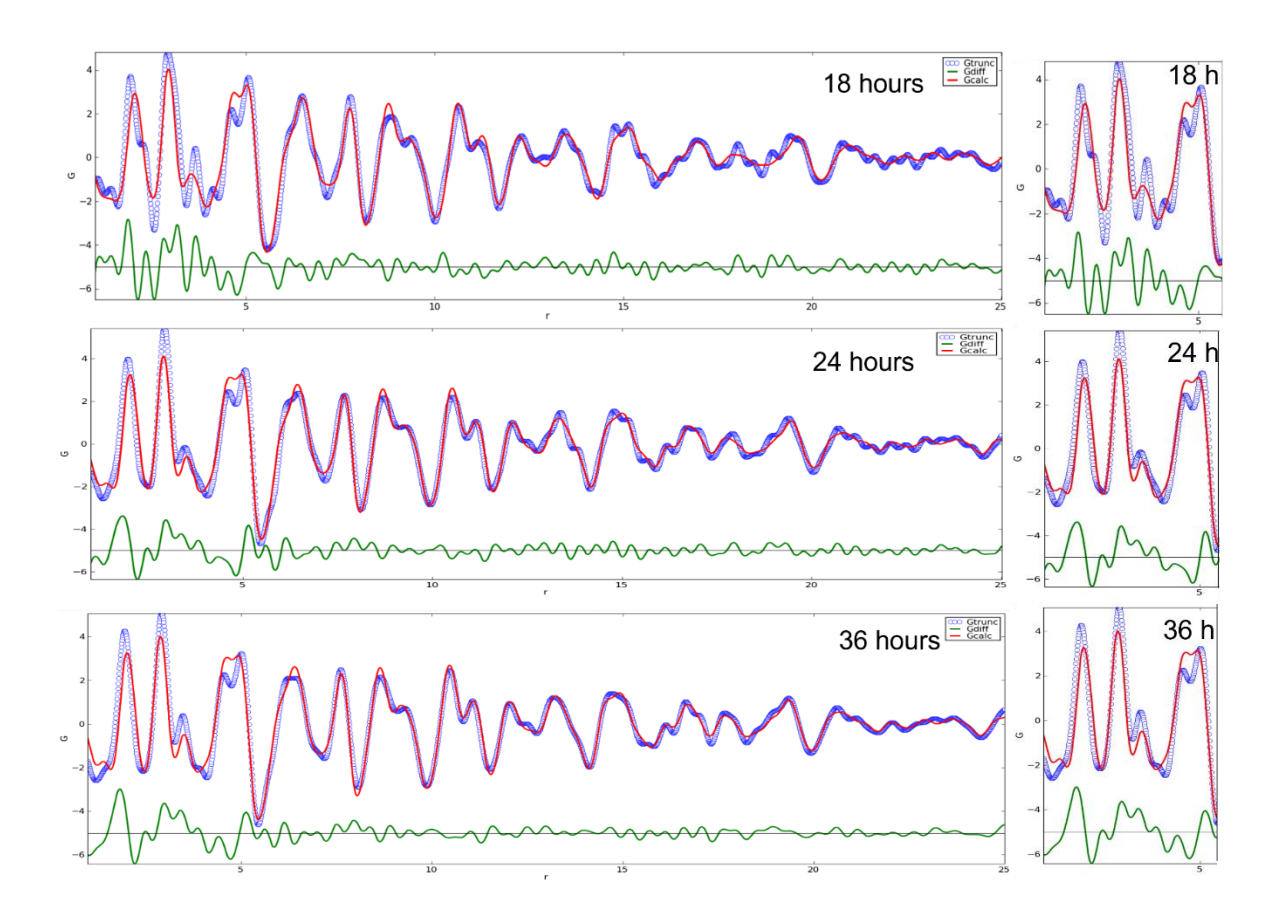


Figure 4.3 (Left) Experimental and calculated atomic pair distribution function profile, G(r), for Li₂MnO₂F samples obtained at 750 rpm for 18 hours, 24 hours and 36 hours. The refinement was performed using a monoclinic (C2/m) structure to describe the disordered rock salt phase. (Right) Highlighted low-r region of 1.5 – 6 Å

The effect of ball milling time on the electrochemical performance of Li₂MnO₂F, galvanostatic cycling experiments in half coin cells were conducted. To prepare the cathode pellets, each active cathode material was mixed with conductive carbon black and PTFE in a ratio of 70:20:10 (Active Material: Carbon Black: Binder). For this, the carbon milling method described in Chapter 2.5 was used. The mixture of Li₂MnO₂F active material and carbon black was ball milled for 3 hours at 300 rpm. Subsequently, PTFE binder (350 µm particle size) was added and mixed using a pestle and mortar for 10 minutes. As final step, the electrode sheets were calendered using a calendering roll pressure machine to minimize porosity on the electrode surface and enhance particle contact [83, 84].

2032-coin type cells were fabricated, with Li metal chips as the counter electrode and 1M LiPF₆ in EC: EMC (3:7 vol.%) as electrolyte in an Ar-filled glovebox. Coin cell

measurements were carried out on a Maccor Battery Tester at room temperature. The charge-discharge performance of each sample was evaluated at a constant current of C/10 rate and were tested within voltage window of 2.0 V to 4.8 V vs. Li/Li⁺. Figure 4.4 displays the charge and discharge capacity curves obtained over 100 cycles from galvanostatic cycling of the Li₂MnO₂F electrodes prepared at ball-milling times of (a) 18 hours, (b) 24 hours, and (c) 36 hours.

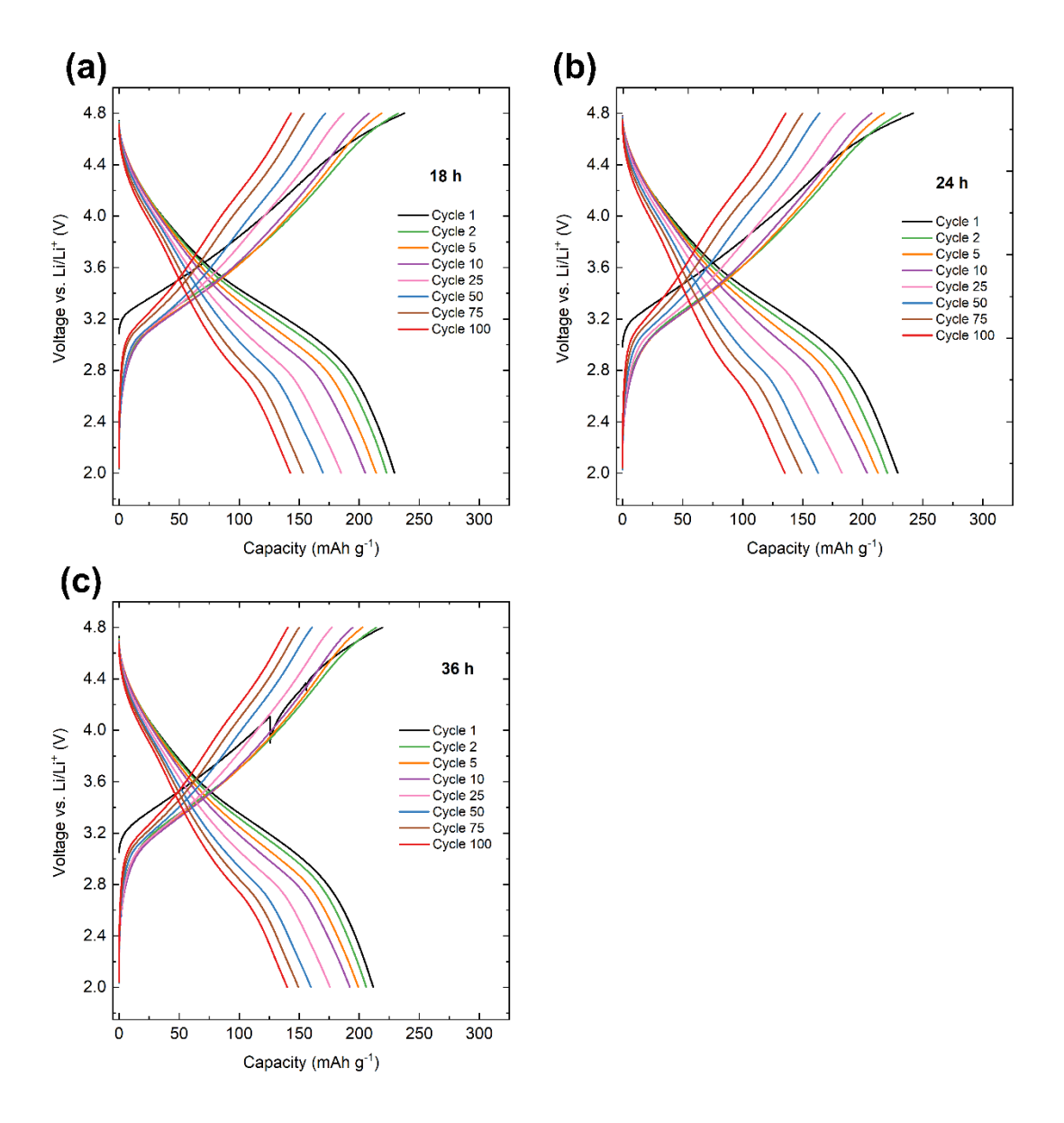


Figure 4.4 The charge-discharge capacity (mAh g⁻¹) vs. voltage (V) curves obtained from galvanostatic cycling over 100 cycles at room temperature of the Li_2MnO_2F pellets (active material: carbon black: 350 µm PTFE in a 70:20:10) (a) 18 hours, (b) 24 hours, (c) 36 hours. 2032-coin type cells were cycled between 2 – 4.8 V vs. Li/Li⁺ at a rate of C/10.

All samples, regardless of ball-milling time, show a reduction in capacity with increasing cycling. This decline in capacity may be partially explained by irreversible first cycle capacity loss due to factors such as electrode degradation, surface reactions, electrolyte decomposition and side reactions [99]. The voltage profile of LMOF-18h (Figure 4.4(a)) and LMOF-24h (Figure 4.4(b)) exhibit similar patterns. They display an initial charge capacity of 237 mAh g⁻¹ and 242 mAh g⁻¹, respectively, along with first-cycle discharge capacities of 229 mAh g⁻¹ for each. This indicates coulombic efficiencies of 96 % and 94 % respectively as shown in Figure 4.5 (a) and (b).

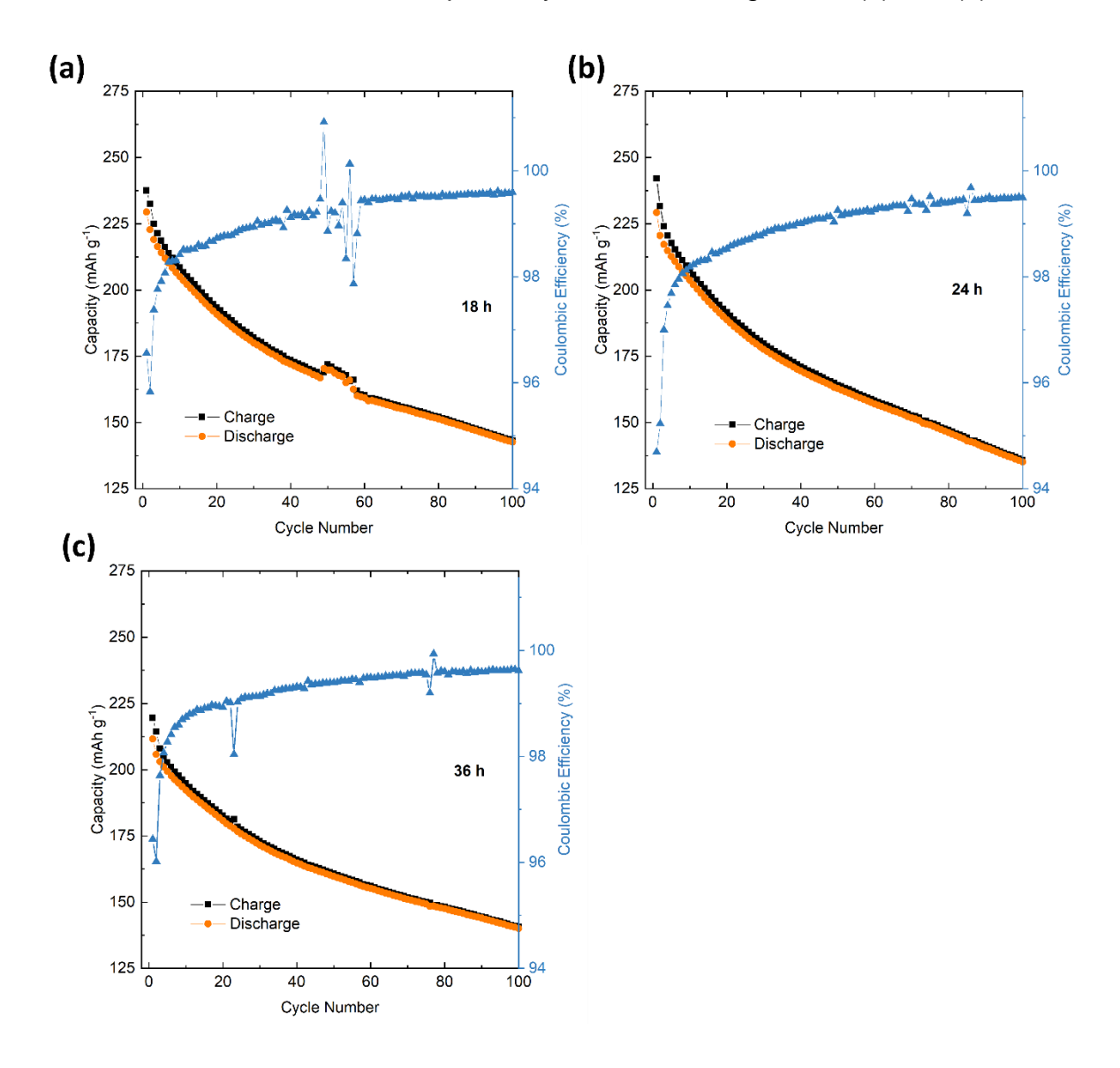


Figure 4.5 Capacity (mAh g⁻¹) and coulombic efficiency (%) vs. cycle number curves obtained over 100 cycles at room temperature of Li₂MnO₂F pellets (active material: carbon black: 350 μm PTFE in a 70:20:10) (a) 18 hours, (b) 24 hours, (c) 36 hours. 2032-coin type cells were cycled between 2 – 4.8 V vs. Li/Li⁺ at a rate of C/10.

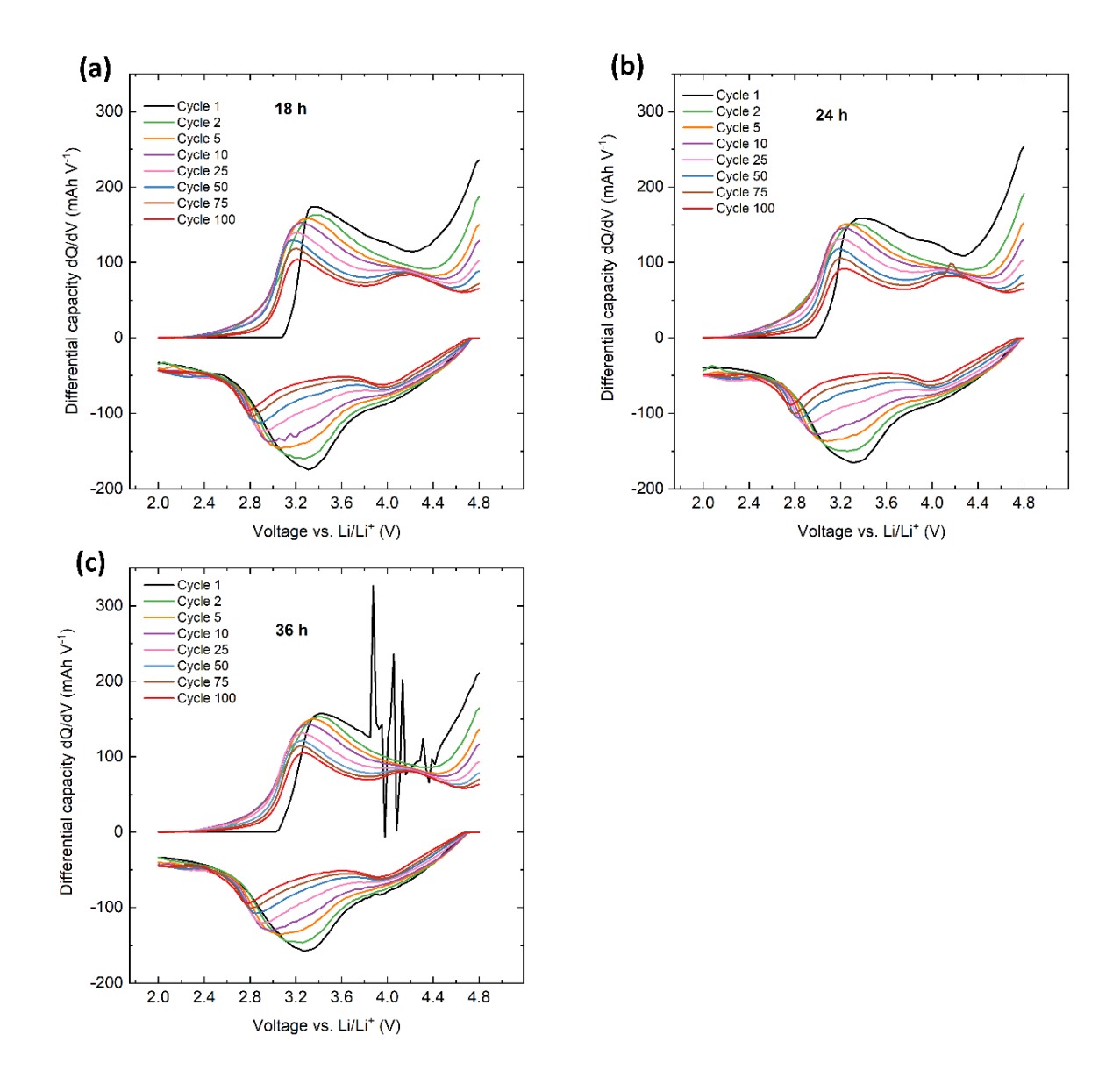


Figure 4.6 The differential capacity (mAh V⁻¹) vs. voltage (V) graph obtained from galvanostatic cycling over 100 cycles at room temperature of the Li_2MnO_2F pellets (active material: carbon black: 350 μ m PTFE in a 70:20:10) (a) 18 hours, (b) 24 hours, (c) 36 hours. 2032-coin type cells were cycled between 2 – 4.8 V vs. Li/Li⁺ at a rate of C/10.

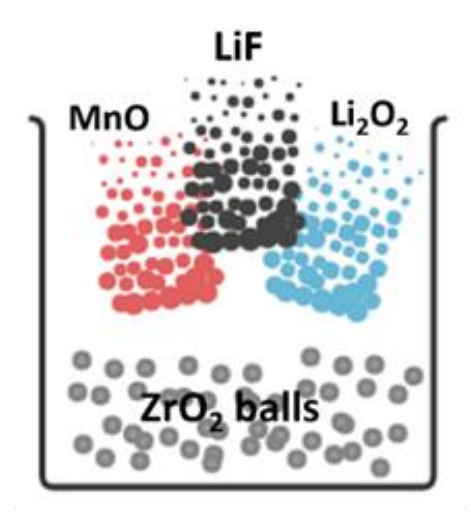
In subsequent cycles, the capacities consistently exhibited very close results. After 100 cycles, LMOF-18h displayed a discharge capacity of 143 mAh g⁻¹ and a capacity retention of 62 %, while LMOF-24h show a 135 mAh g⁻¹ discharge capacity, with a capacity retention of 59 %. Figure 4.4 (c) shows the charge-discharge profiles corresponding to LMOF-36h. This sample exhibited a lower initial charge capacity of 219 mAh g⁻¹ followed by a discharge capacity of 211 mAh g⁻¹. This gave an initial cycle

coulombic efficiency of 96 % as shown in Figure 4.5 (c). Compared to other samples, LMOF-36 hour ball-milled cathodes show much lower an initial charge and discharge capacity. While the LMOF-18h and LMOF-24h electrodes exhibited capacities of approximately 200 mAh g⁻¹ after 10 cycles, the LMOF-36h electrodes exhibits a 192 mAh g⁻¹ of discharge capacity delivered on 10th cycles. However, over the 100 cycles measured, LMOF-36 shows a 140 mAh g⁻¹ of discharge capacity, with a discharge capacity retention of 66 %.

Differential capacity plots (Figure 4.6 (a), (b) and (c)) for all samples show similar profiles, where broad peaks between 3.2 V and 3.6 V are attributed to Mn-redox and the second peak in the first charge cycle at higher voltage is attributed to oxygen redox. Over the 100 cycles, all samples display a development of a new peak at 4.2 V and reduction region peaks are shifting from 3.4 V to 2.8 V.

4.2.2. Optimising starting materials for Li₂MnO₂F synthesis

Having optimised the ball milling reaction time, attention was focused on applying different lithium (Li₂O₂ (lithium peroxide) and Li₂O (lithium oxide)) and manganese (MnO (manganese oxide) and Mn₂O₃ (manganese (III) oxide)) sources to examine the influence of starting materials on the final products. Figure 4.7 shows a schematic for the mechanochemical synthesis of Li₂MnO₂F, where two approaches were taken. In one set of reactions, all precursors were mixed in one step and ball milled at 750 rpm for 18 hours, similar to the synthesis conditions in section 2.3.2.2. In the second approach, a two-stage ball milling method was applied, where the transition metal oxide and lithium (per)oxide precursors were first mixed at 750 rpm for 9 hours before addition of the LiF precursor and mixing at 750 rpm for 9 hours, similar to the synthesis conditions in section 2.3.2.3.



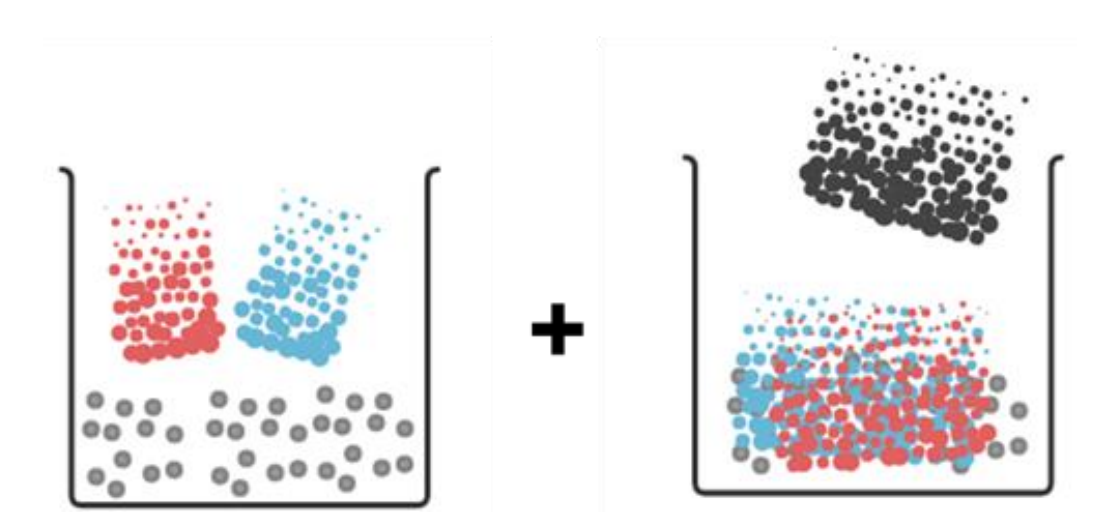


Figure 4.7 Reaction schematic for the mechanochemical synthesis of Li₂MnO₂F, **(a)** where the precursors mixed in one step and ball milled at 750 rpm for 18h. **(b)** where the transition metal oxide (red) and lithium (per)oxide (blue) precursor mixed at 750 rpm for 9 hours and the LiF precursor (black) added and mixed at 750 rpm for 9 hours. The grey colour shape represents ZrO₂ balls in ZrO₂ ball milling media.

Figure 4.8 shows the XRD patterns obtained of the products after mechanosynthesis of Li₂MnO₂F at 750 rpm for 18 hours (one-step ball milling) and 9 hours +9 hours (two-step ball milling). Sample "A" is prepared using Li₂O₂, MnO and LiF while sample B is prepared using Li₂O, Mn₂O₃, and LiF.

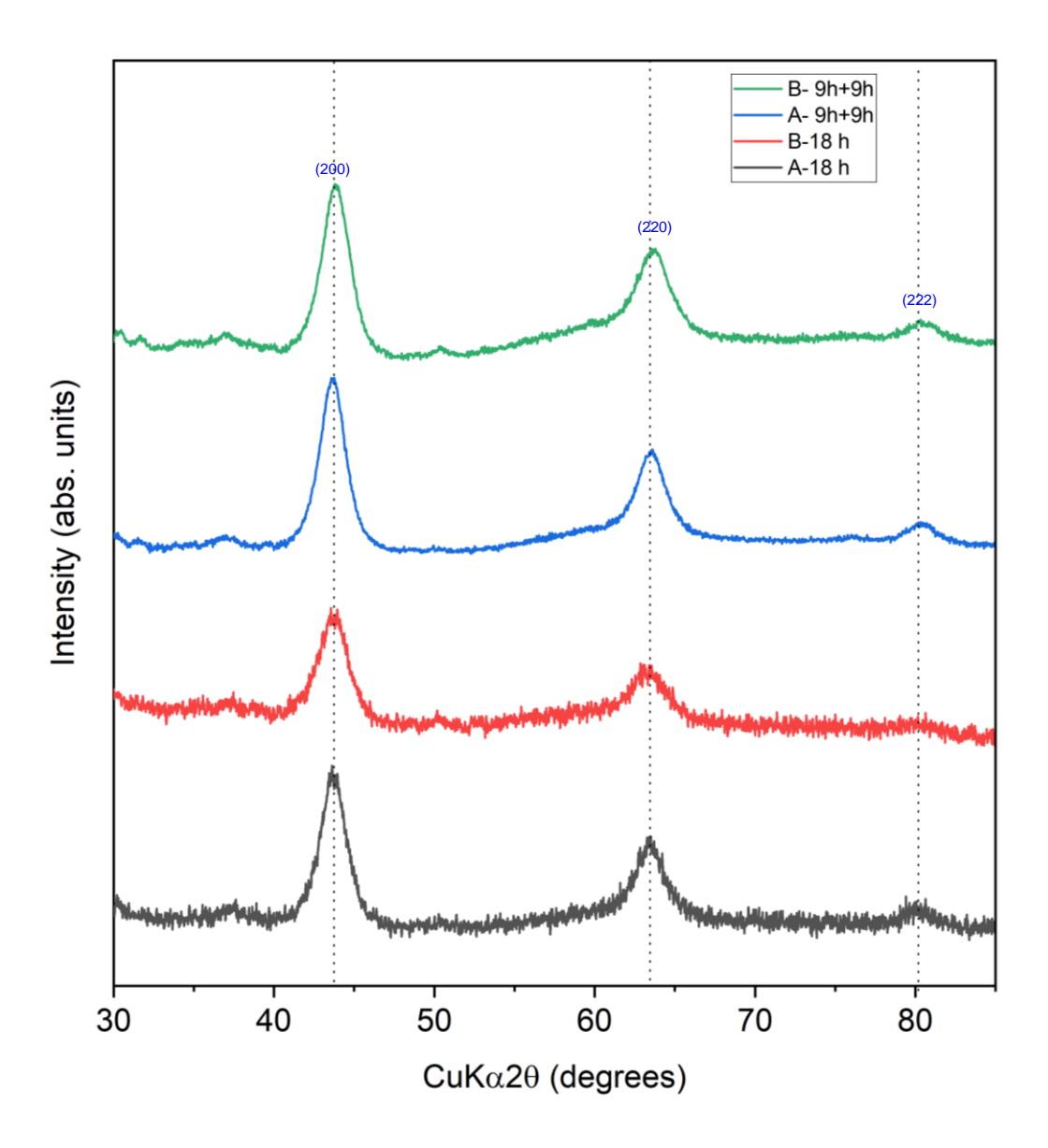


Figure 4.8 XRD patterns of the product during mechanosynthesis of Li₂MnO₂F at 750 rpm for one-step ball milling (18 hours) and two-step ball milling (9 hours +9 hours). Sample "A" is prepared using Li₂O₂, MnO and LiF, "A-18h" (black) refers one-step ball milling and "A-9h+9h" (blue) refers two-step ball milling. Sample "B" is prepared using Li₂O, Mn₂O₃, and LiF, "B-18h" (red) refers one-step ball milling and "B-9h+9h" (green) refers two-step ball milling.

The XRD patterns confirmed the presence of three main peaks for Li₂MnO₂F. Figure 4.8 reveals diffraction patterns for all samples display broad peaks with a noisy background, indicating low crystallinity and/or small samples sizes. From Bragg's law, a lattice parameter of 4.1106 Å is calculated.

For electrochemical evaluation, each active cathode material was mixed with conductive carbon black and 350 µm PTFE in a weight ratio of 70:20:10 (Active Material: Carbon Black: Binder) using a mortar and pestle for 30 minutes. Subsequently, the electrode sheets were calendered using a calendering roll pressure machine to minimize porosity [84]. 2032-coin type cells were fabricated, with Li metal chips as the counter electrode and 1M LiPF₆ in EC: EMC (3:7 vol.%) as electrolyte in an Ar-filled glovebox. Coin cell measurements were carried out on a Maccor Battery Tester at room temperature. The charge-discharge performance of each sample was evaluated at a constant current of C/10 rate and were tested within voltage window of 2.0 V to 4.8 V vs. Li/Li⁺. Galvanostatic cycling was examined over 50 cycles for Li₂O₂ and Li₂O produced Li₂MnO₂F cathodes, under both one-step ball milling (18 h) and two-step ball milling (9 h+9 h) conditions. Figure 4.9 displays the charge and discharge capacity curves obtained over 50 cycles from galvanostatic cycling of the Li₂MnO₂F electrodes (a) Li₂O₂-18 h, (b) Li₂O₂-9h+9h, (c) Li₂O-18 h, and (d) Li₂O-9h+9h.

The voltage profile of Li₂O₂-18h (Figure 4.9(a)) and Li₂O₂-9h+9h (Figure 4.9(b)) exhibit similar patterns. They display an initial charge capacity of 231 mAh g⁻¹ and 234 mAh g⁻¹, respectively, along with first-cycle discharge capacities of 227 mAh g⁻¹ and 225 mAh g⁻¹. This indicates coulombic efficiencies of 98% and 96% respectively as shown in Figure 4.10 (a) and (b). After the 10th cycle a noticeable difference was observed. Li₂O₂-18h exhibited a discharge capacity of 198 mAh g⁻¹ with capacity retention of 87 %, while Li₂O₂- 9h+9h exhibited a discharge capacity of 188 mAh g⁻¹ with capacity retention of 83 %. However, over 45th cycles measured, Li₂O₂-18h and Li₂O₂-9h+9h display again similar 162 mAh g-1 of discharge capacity, with a discharge capacity retention of 71% for each. The voltage profile of Li₂O-18h (Figure 4.9(c)) displays an initial charge capacity of 189 mAh g⁻¹ followed by a discharge capacity of 184 mAh g⁻¹ 1. It exhibits coulombic efficiency of 97 % as shown in Figure 4.10 (c). The Li₂O-9h+9h (Figure 4.9(d)) shows an initial charge capacity of 197 mAh g⁻¹ and discharge capacity of 190 mAh g⁻¹. This indicates coulombic efficiency of 96% as shown in Figure 4.10 (d). Although there were minor changes in the subsequently cycles, similar capacity results were obtained. Over 50th cycles, Li₂O-18h display a discharge capacity of 157 mAh g⁻¹ and Li₂O-9h+9h exhibit a discharge capacity of 155 mAh g⁻¹.

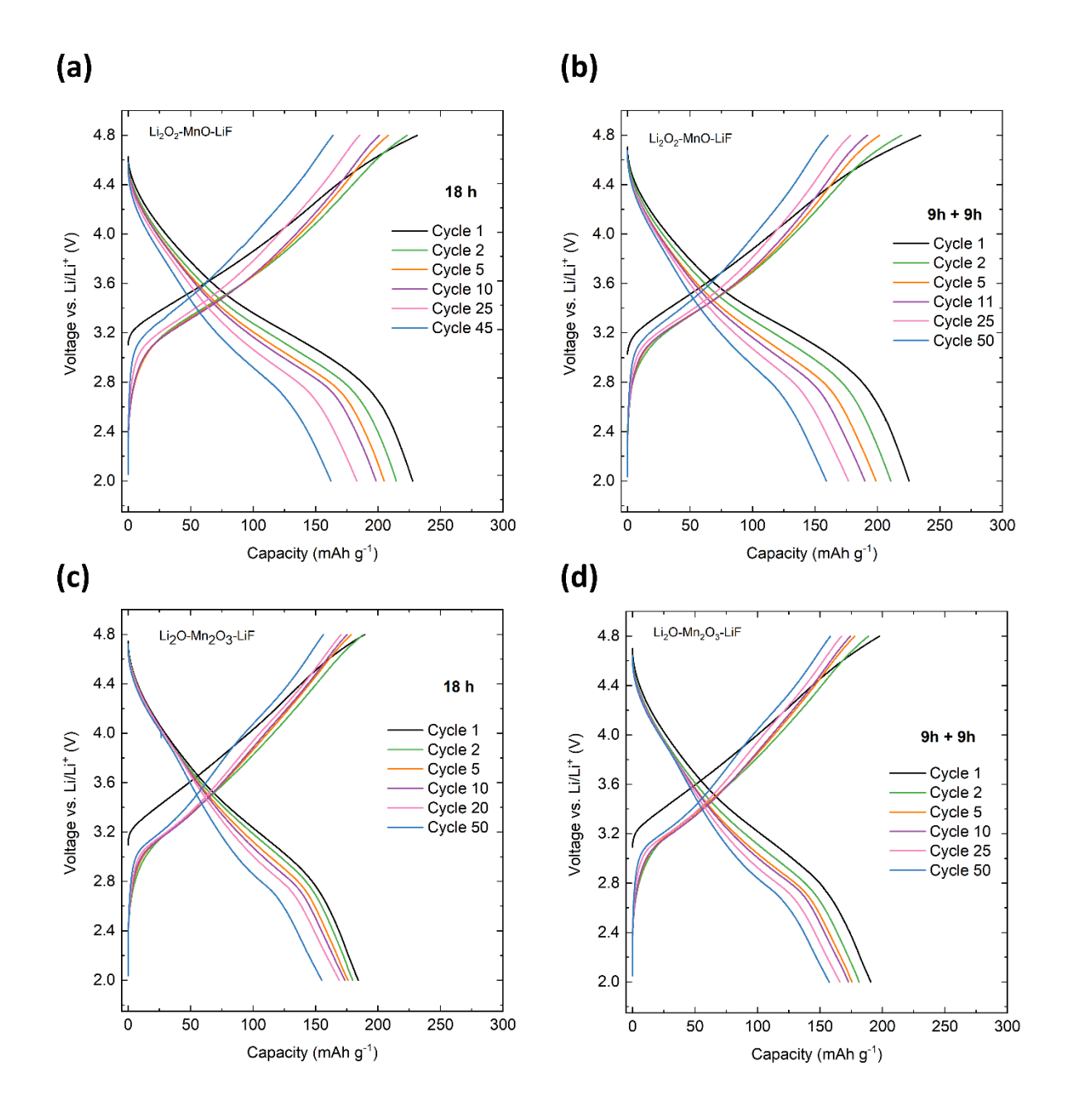


Figure 4.9 The charge-discharge capacity (mAh g^{-1}) vs. voltage (V) curves obtained from galvanostatic cycling over 50 cycles at room temperature of the Li₂MnO₂F pellets (active material: carbon black: PTFE in a 70:20:10) (a) (b) (c) (d). 2032-coin type cells were cycled between 2 – 4.8 V vs. Li/Li⁺ at a rate of C/10.

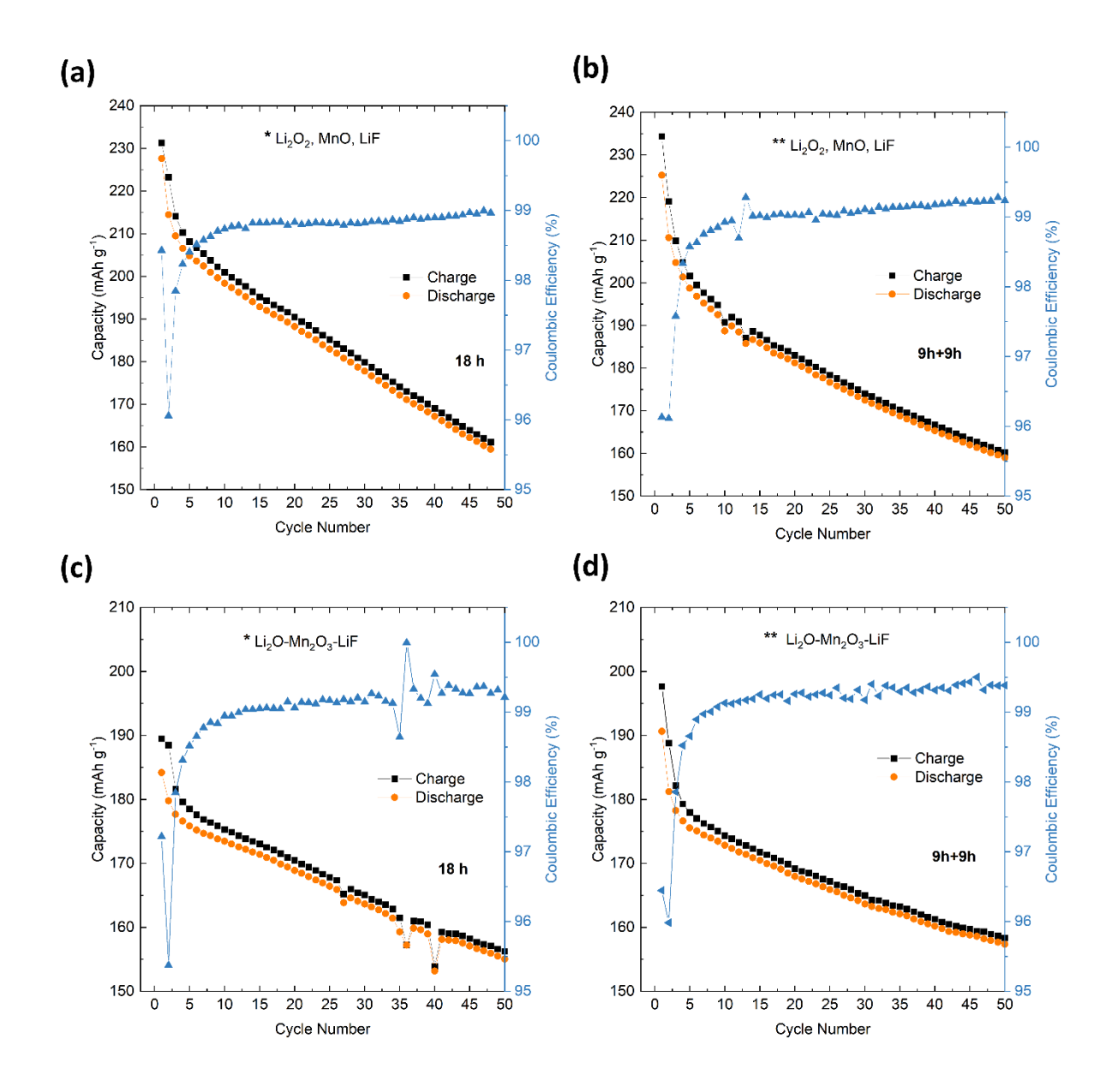


Figure 4.10 The charge-discharge capacity (mAh g^{-1}) and coulombic efficiency (%) vs. cycle number curves obtained from galvanostatic cycling over 50 cycles at room temperature of the Li₂MnO₂F pellets (active material: carbon black: PTFE in a 70:20:10) (a) (b) (c) (d). 2032-coin type cells were cycled between 2 – 4.8 V vs. Li/Li⁺ at a rate of C/10.

Differential capacity plots (Figure 4.11(a), (b), (c), and (d)) for all samples show similar profiles, where broad peaks between 3.2 V and 3.6 V are attributed to Mn-redox and the second peak in the first charge cycle at higher voltage is attributed to oxygen redox. The prolonged cycled for Li₂O₂-18h and Li₂O₂- 9h+9h, the reduction peak gradually

shifts from 3.2 V to 2.8 V. For Li₂O-18h and Li₂O-9h+9h samples, however, this change is immediately apparent in the second cycle, along with shifting from 3.2 V to 2.8 V.

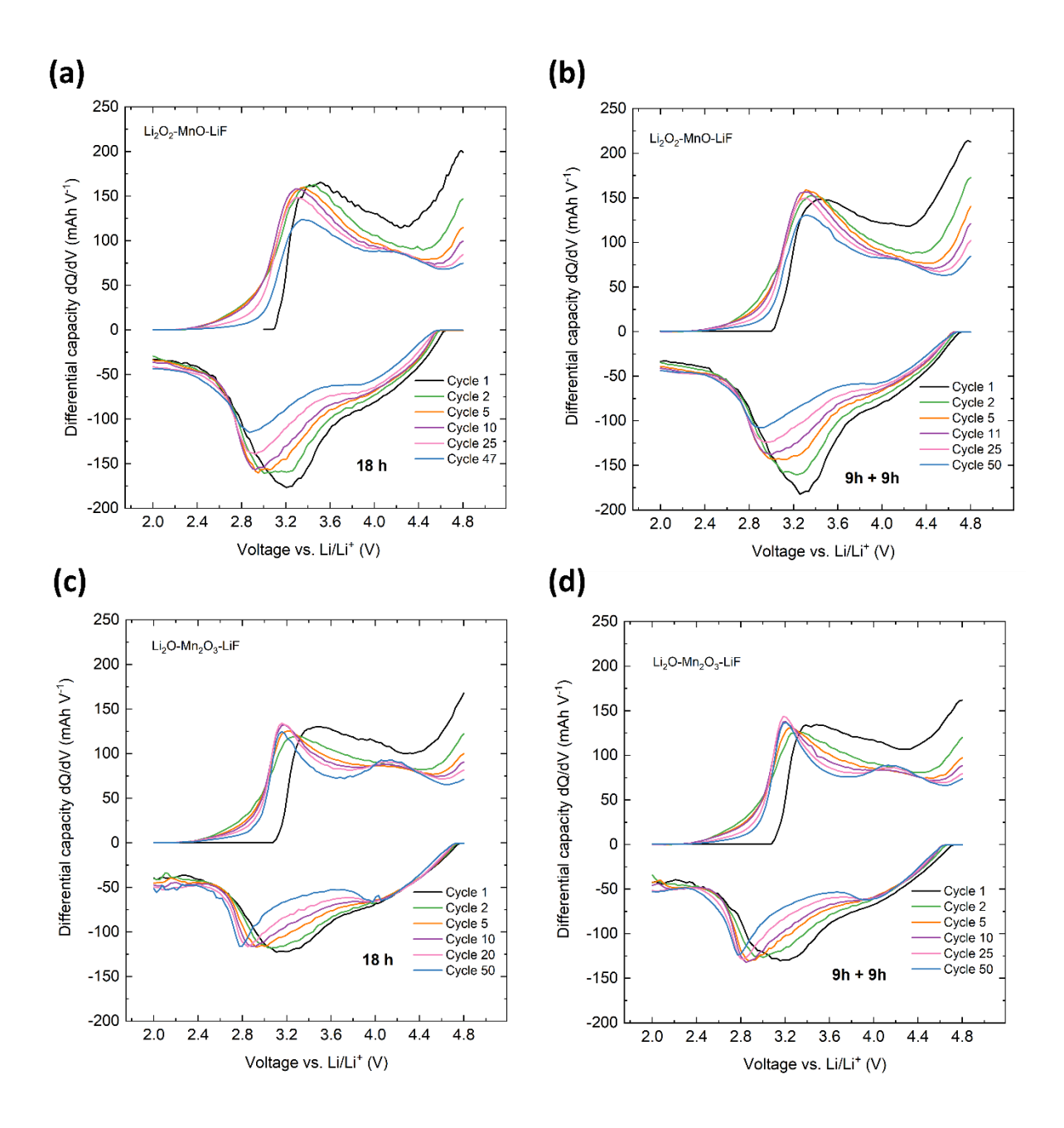


Figure 4.11 The differential capacity (mAh V⁻¹) vs. voltage (V) graph obtained from galvanostatic cycling over 50 cycles at room temperature of the Li₂MnO₂F pellets (active material: carbon black: PTFE in a 70:20:10) (a) (b) (c) (d). 2032-coin type cells were cycled between 2 − 4.8 V vs. Li/Li+ at a rate of C/10.

Previous studies have reported cation-disordered rock salt cathodes obtained from different transition metal oxide and lithium sources such as Li₂CO₃, Li₂O using high-

temperature solid state synthesis. These studies also showed that the long heat treatment causes Li evaporation under the high temperature experimental conditions depending on Li-source [116]. However, even without the need for heat treatment in the mechanochemical synthesis, some defects may be encountered due to mechanical grinding. These defects may vary depending on the precursor used, affecting the electrochemical performance. It is known that the different precursors directly effect on the phase and crystal structure of the synthesized material. Moreover, each precursor can cause different impurities, contamination issues and side reactions. The results demonstrate in this chapter demonstrate that differences in the synthesis methods (e.g. milling time, milling steps) and starting materials choices lead to differences in initial charge and discharge capacities.

4.2.3. Selecting binder particle size for optimising Li₂MnO₂F cycling performance

In addition to optimising the synthesis of the cathode powder, there is also the opportunity to optimise the polymer binder used in the cathode film. To investigate the effect of polymer binder particle size, Li₂MnO₂F, prepared by mechanosynthesis of Li₂O₂, MnO and LiF precursors at 750 rpm at 24 hours, was applied as the cathode powder and PTFE with 35µm, 350 µm and bead particle sizes were used as binder. To prepare the cathode pellets, the active cathode material was mixed with conductive carbon black and PTFE in a weight ratio of 70:20:10 (Active Material: Carbon Black: Binder) using a mortar and pestle for 30 minutes and the electrode sheets were calendered [83, 84]. 2032-coin type cells were fabricated, with Li metal chips as the counter electrode and 1M LiPF₆ in EC: EMC (3:7 vol.%) as electrolyte in an Ar-filled glovebox. Coin cell measurements were carried out on a Maccor Battery Tester at room temperature. The charge-discharge performance of each sample was evaluated at a constant current of C/10 rate and were tested within voltage window of 2.0 V to 4.8 V vs. Li/Li⁺.

Figure 4.12 exhibits the charge and discharge capacity curves obtained over 70 cycles from galvanostatic cycling of the Li_2MnO_2F electrodes prepared with PTFE particles of different size (a) 35 μ m, (b) 350 μ m, and (c) beads. The first charge cycle for LMOF-35 μ m is found to be 230 mAh g⁻¹, followed by a discharge capacity of 185 mAh g⁻¹. This indicates coulombic efficiency of 80 % as shown in Figure 4.12 (a). LMOF-350

μm PTFE and LMOF- beads PTFE show very similar capacity results. They exhibit an initial charge capacity of 225 mAh g⁻¹ and 224 mAh g⁻¹, respectively, along with first-cycle discharge capacities of 210 mAh g⁻¹ and 212 mAh g⁻¹. This indicates coulombic efficiencies of 93 % and 94 % as shown in Figure 4.12 (b) and (c).

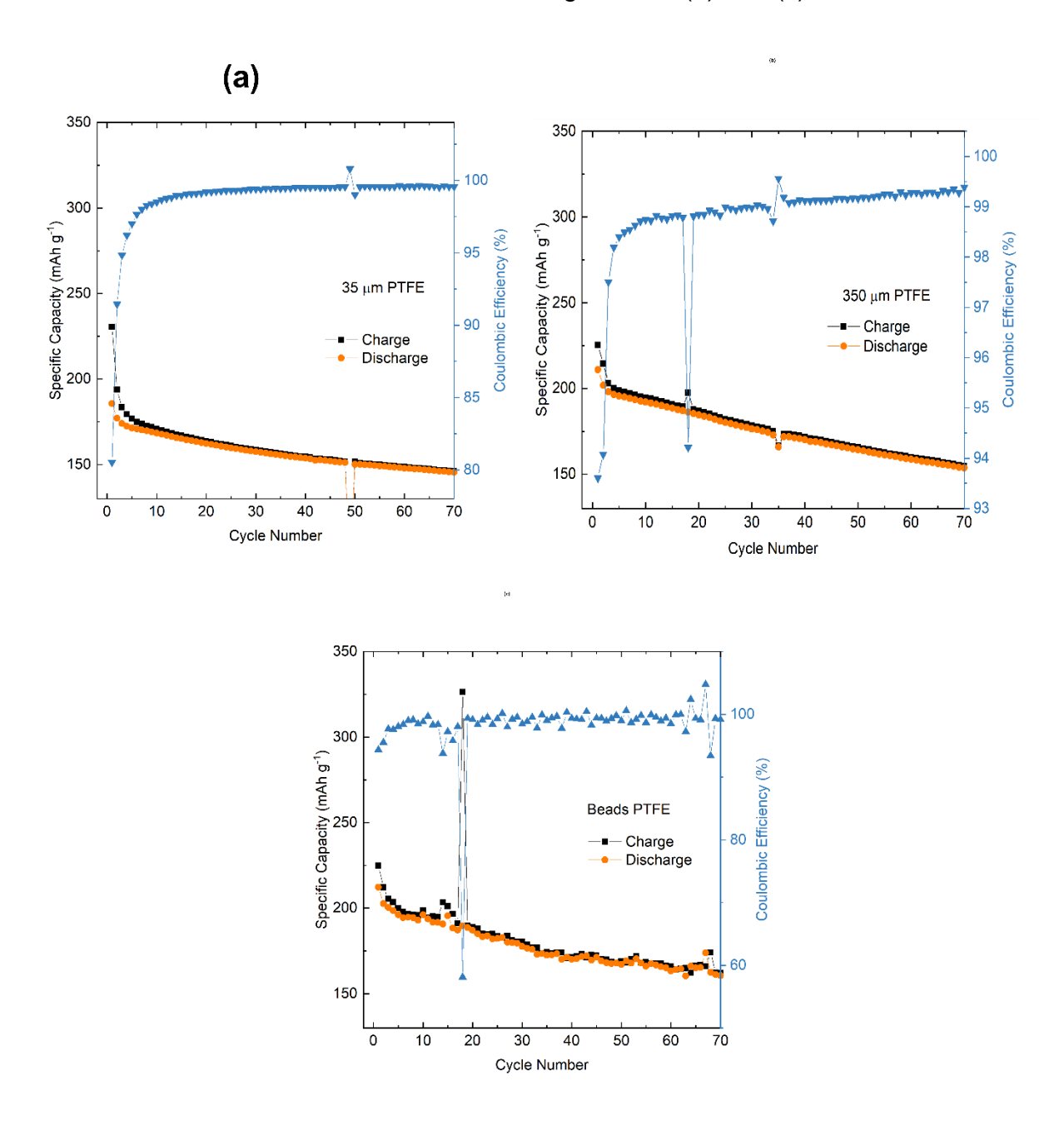


Figure 4.12 The charge-discharge capacity (mAh g⁻¹) and coulombic efficiency (%) vs. cycle number curves from galvanostatic cycling over 70 cycles at room temperature of Li₂MnO₂F pellets with different particle size PTFE (a) 35 μm PTFE (b) 350 μm PTFE (c) beads PTFE. 2032-coin type cells were cycled between 2-4.8 V vs. Li/Li⁺ at a rate of C/10.

SEM images were recorded of the electrode materials prior and post cycling and are shown in Figure 4.13. From these images, the cross-sections of electrodes prepared using 350 µm PTFE appear to better bind the active material with the conductive carbon. Post cycling, the cathodes prepared using 35 µm PFTE appear to have more evidence of gaps within the cathode film. The appearance of fibrous structures is observed for the 350 µm samples. Such fibres have been noted in the literature, where these can act as a matrix to support the active powder and carbon [117].

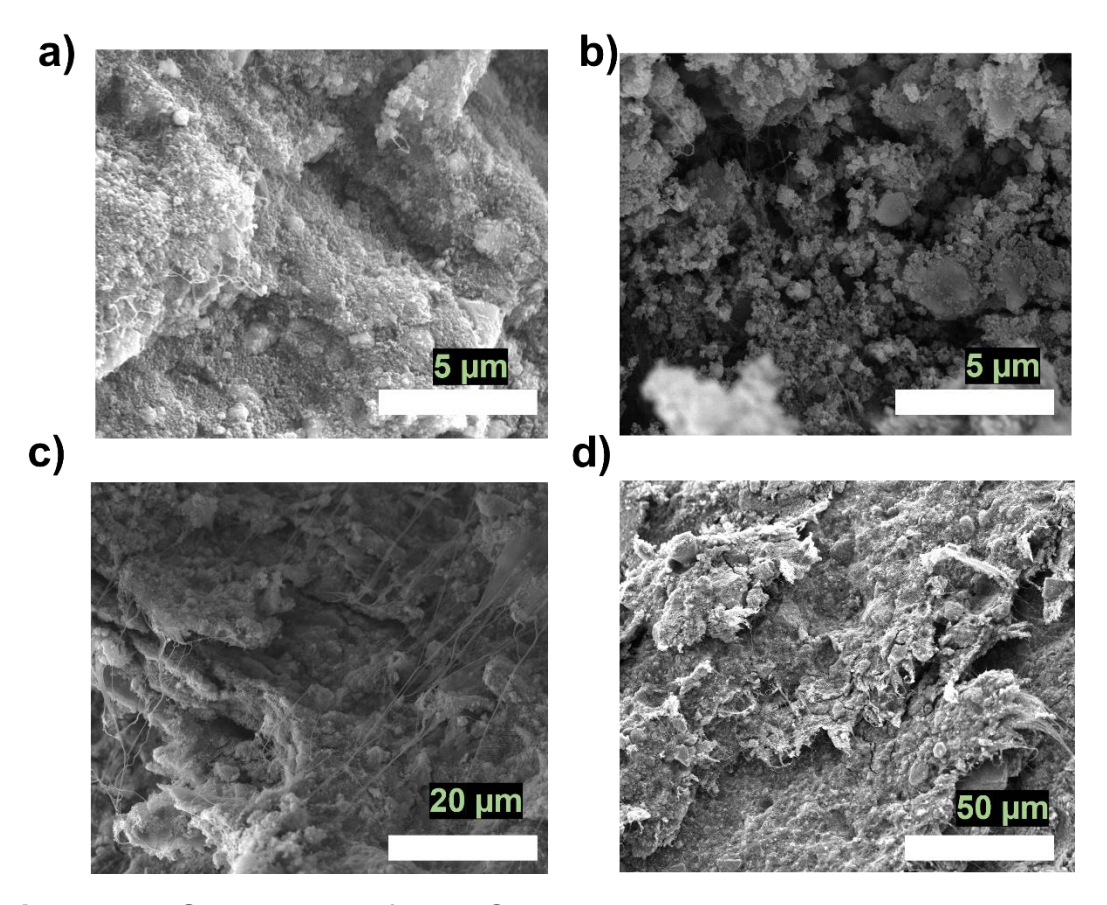


Figure 4.13 SEM images of Li₂MnO₂F electrode prepared using **35 μm PTFE** (a) precycling, (b) post-cycling and **350 μm PTFE** (c) pre-cycling (d) post-cycling.

4.2.4. Optimising carbon/binder/active material ratio for cycling performance of Li₂MnO₂F

A previous section has shown that Li₂MnO₂F has been successfully optimised using MnO, Li₂O₂ and LiF precursors at 750 rpm for 18h and that the best cycling performance is obtained using PTFE with a size of 350 µm. The next step was to optimise the active material: binder: conductive carbon ratio used in the cathode. The

previous section applied a ratio of 70:20:10, which is commonly applied in the literature. To examine the effect of cathode film content ratios, two further ratios were examined, 80:10:10 and 60:20:20 of active material: binder: carbon. Cathode pellets were prepared with active cathode material mixed with conductive carbon black and PTFE in a weight ratio of 80:10:10 or 60:20:20 using a mortar and pestle for 30 minutes. Subsequently, the electrode sheets were calendered using a calendering roll pressure machine to minimize porosity and enhanced particle contact [84]. The electrode sheet was cut using 7mm diameter punch and dried at 80°C overnight to remove any moisture or other volatile contamination before transferring the electrodes into a glovebox. The electrode sheets after calendaring are shown in Figure 4.14 and it is clear from these images that the electrodes prepared with ratios of 80:10:10 are very fragile.

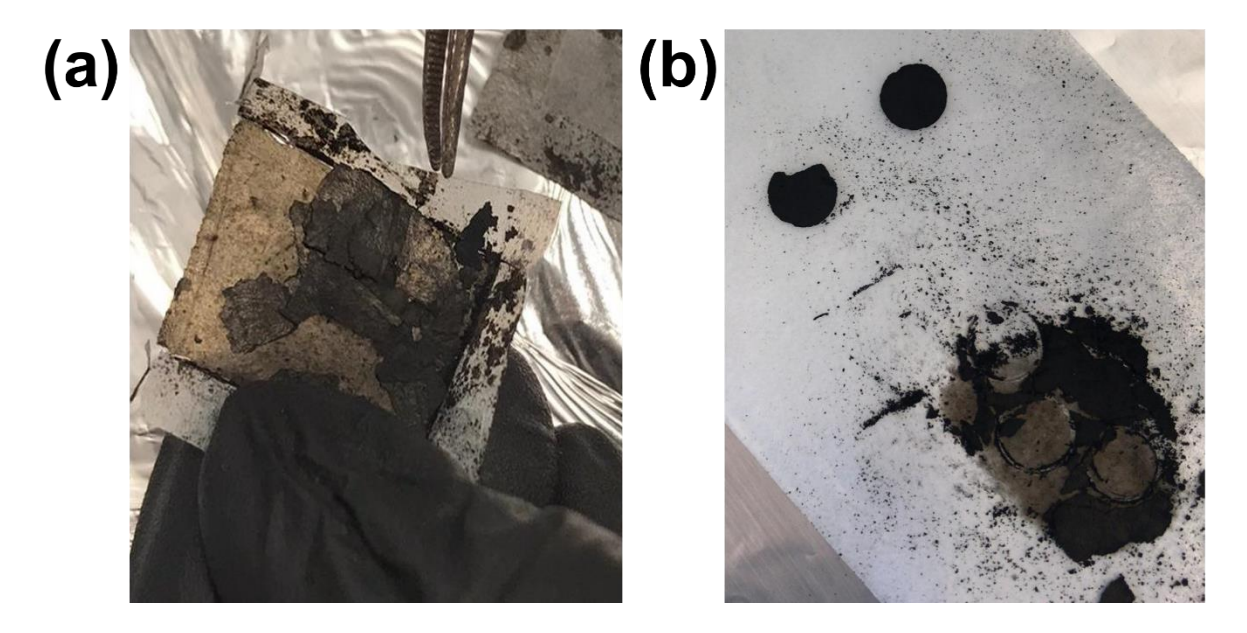


Figure 4.14 The Li₂MnO₂F electrode sheets after calendering a calendering roll pressure machine (a) the Li₂MnO₂F pellet prepared in a ratio of 80:10:10 (active material: carbon black: PTFE), (b) the Li₂MnO₂F pellet prepared in a ratio of 60:20:20 (active material: carbon black: PTFE).

2032-coin type cells were fabricated, with Li metal chips as the counter electrode and 1M LiPF6 in EC: DMC (50:50 vol.%) as electrolyte in an Ar-filled glovebox. Coin cell measurements were carried out on a Maccor Battery Tester at room temperature. The charge-discharge performance of each sample was evaluated at a constant current of C/10 rate and were tested within voltage window of 2.0 V to 4.8 V vs. Li/Li⁺. Figure

4.15 (a) displays the charge and discharge capacity curves obtained over five cycles from galvanostatic cycling for Li₂MnO₂F prepared with a ratio of 80:10:10.

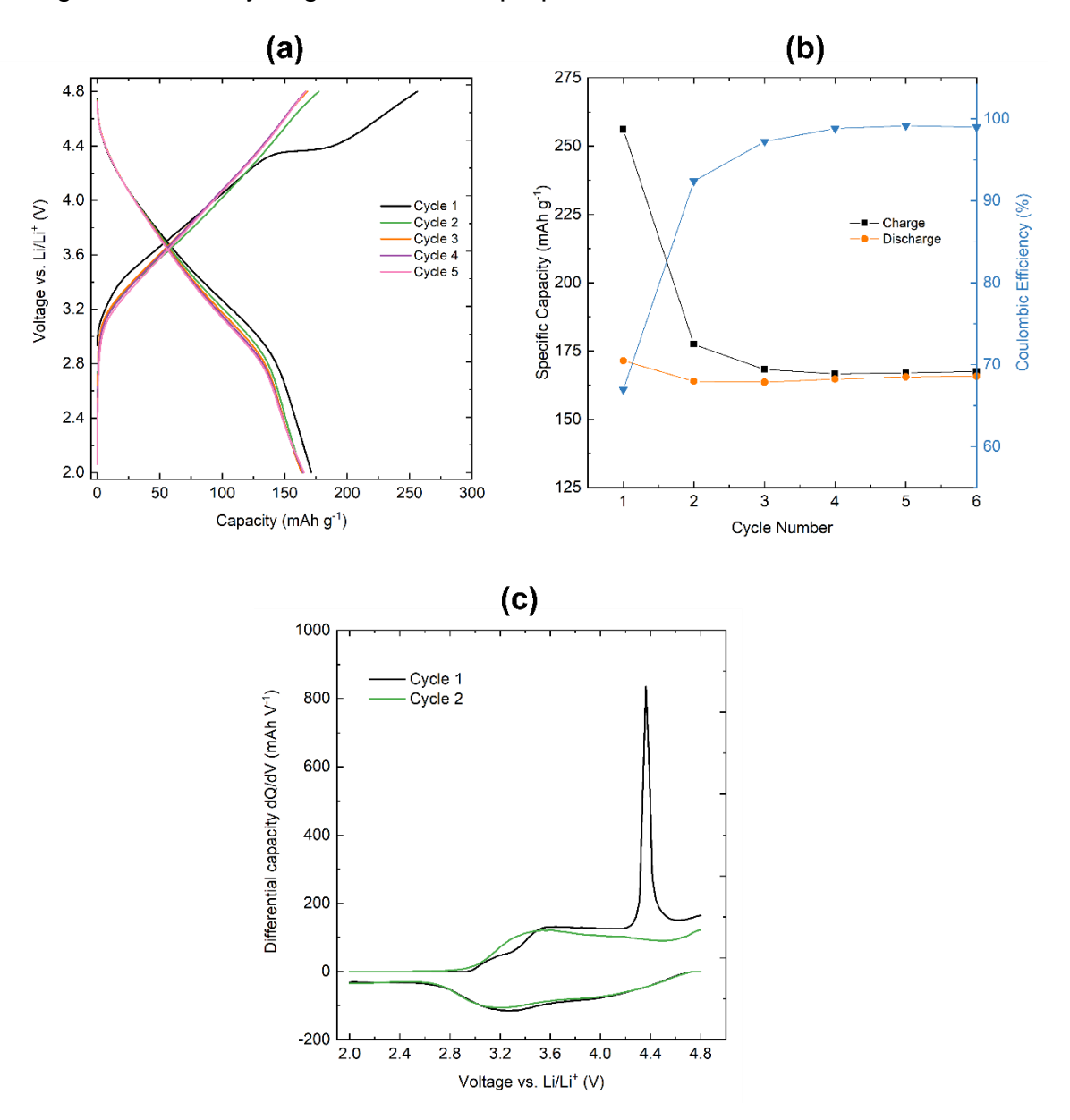


Figure 4.15 (a) The charge-discharge capacity vs. voltage curves, (b) the specific capacity and coulombic efficiency vs. cycle number, (c) the differential capacity vs. voltage graph obtained from galvanostatic cycling over 5 cycles at room temperature of the Li₂MnO₂F pellets (active material: carbon black: PTFE in a ratio of 80:10:10). 2032-coin type cells were cycled between 2 – 4.8 V vs. Li/Li⁺ at a rate of C/10.

The initial charge capacity observed was 256 mAh g⁻¹ with a subsequent discharge capacity of 171 mAh g⁻¹. A plateau region between 4.3 V and 4.4 V is also clearly visible during the first charge cycle. As shown in Figure 4.15 (b), the first cycle

coulombic efficiency was calculated to be approximately 67 %. A low coulombic efficiency (e.g., 88 %- 95 %) for the first cycle is a normal expected behaviour for Mn-based disordered rock salt cathodes [63]. This can be explained by the fact that these materials are operating at high voltages. The voltage range is higher than the operating range of commonly employed electrolytes, potentially resulting in electrolyte degradation [118]. Nevertheless, the coulombic efficiency in the Li₂MnO₂F electrode is considerably lower than would be expected. In the subsequent cycles, it displays stable cycling behaviour with charge and discharge capacity retentions above 92 %.

Figure 4.15 (c) presents the differential capacity vs. voltage graphs over the first cycle and second cycles. The initial charge cycle exhibited a broad oxidation peak between 3.2 V to 3.6 V and then there is a sharp oxidation peak at 4.4 V. This indicates that the partial substitution of fluorine with oxygen successfully lowers Mn oxidation state to Mn³⁺, making Mn^{3+/4+} redox possible [119]. Therefore, the first peak is typical of Mn^{3+/4+} redox process. In addition, the second sharp peak might explain the oxygen redox contribution to the capacity (ref). The high initial charge capacity value, higher than the expected theoretical capacity of the transition metal redox alone, can be explained because of this oxygen redox process. A reduction peak was observed during the first discharge cycle at ~3.2 V and can be related to the Mn^{4+/3+} reduction. The absence of a clear peak around 4.4 V for oxygen redox indicates a non-reversible process. Previous studies have shown that the oxygen redox process can lead to release of oxygen gas during the cycling process and can cause surface reconstructions [120], which may result in quicker capacity decay. Another explanation for the large oxygen redox peak observed here could be due to air exposure. Since these electrodes are air sensitive, oxygen and moisture in the air might cause them to degrade or modify their surface. Therefore, in order to overcome such issues, the Li₂MnO₂F electrode fabrication process should be conducted in an inert atmosphere. Preparing electrodes under inert conditions is very time-consuming and to find the optimised electrode component ratios, these electrodes were prepared on the bench (i.e. not in an inert atmosphere) initially.

The voltage profile of Li₂MnO₂F electrodes with prepared in a ratio of 60:20:20 (active material: carbon black: PTFE) is shown in Figure 4.16 (a). As in the previous example, LMOF-622 (Figure 4.16(a)) shows a large plateau between approximately 4.4 V and

4.7 during the first charge cycle. The initial charge capacity is 320 mAh g⁻¹, which decreases to 266 mAh g⁻¹ for the first cycle discharge capacity. The first cycle coulombic efficiency is obtained approximately 83%, as shown in Figure 4.16 (b).

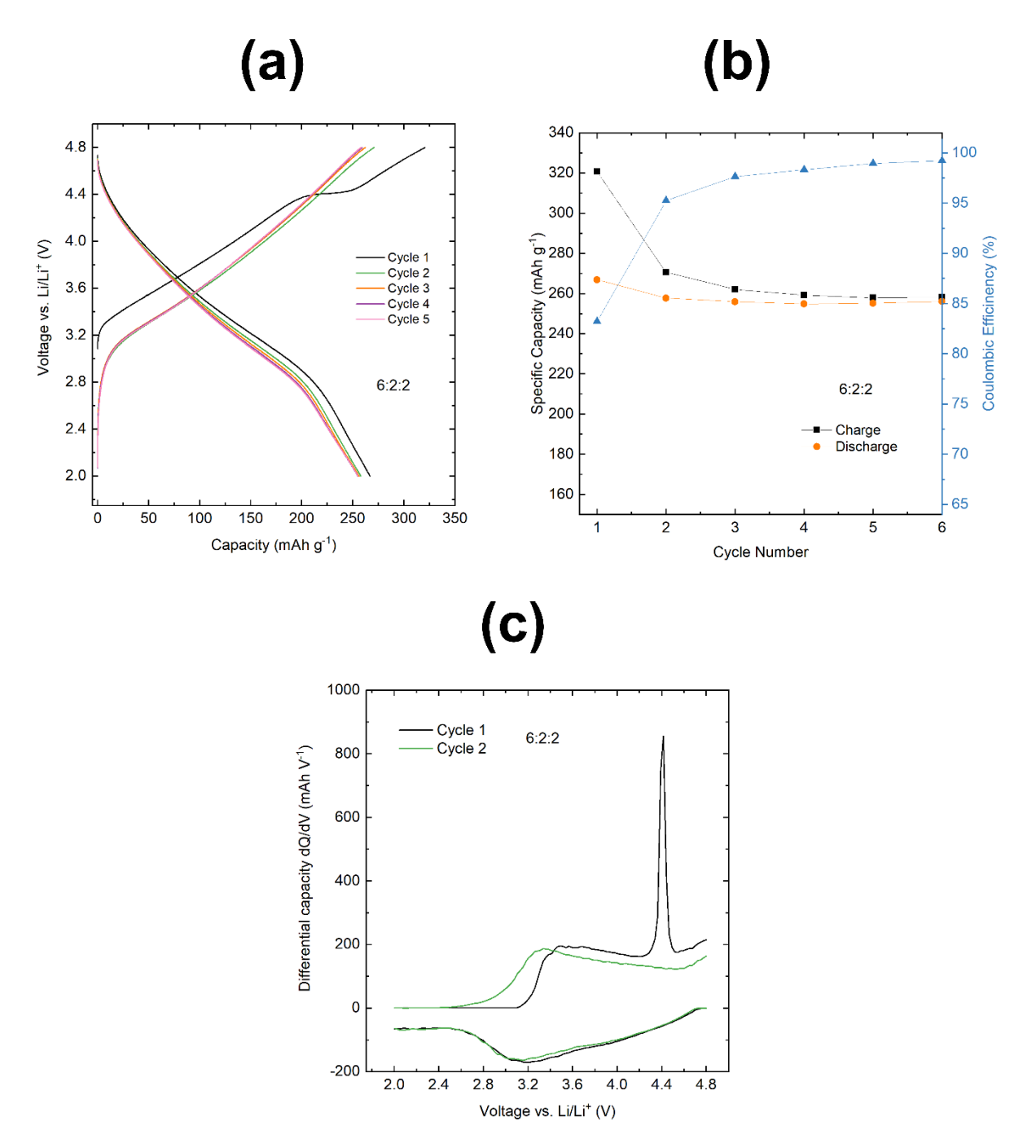


Figure 4.16 (a) Capacity vs. voltage curves, (b) the specific capacity and coulombic efficiency vs. cycle number, (c) the differential capacity vs. voltage graph obtained from galvanostatic cycling at room temperature of the Li₂MnO₂F pellets (active material: carbon black: PTFE in a ratio of 60:20:20). 2032-coin type cells were cycled between 2 – 4.8 V vs. Li/Li⁺ at a rate of C/10.

During all electrode preparations thus far, the active material and carbon black were initially mixed for a period, followed by the addition of the binder into the mixture of active materials and carbon black. Here, the mixing process was undertaken using the two different methods: the first method involved a pestle and mortar, while the second method utilized ball milling (Figure 4.17).

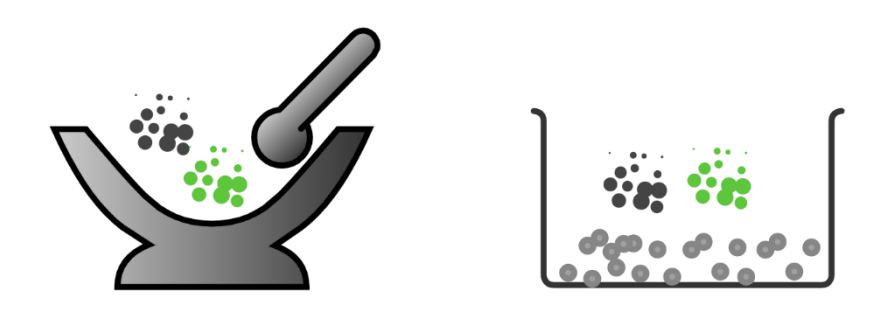


Figure 4.17 For electrode preparation process, while active material and carbon black are mixed **(a)** for 20 minutes using a pestle and mortar, **(b)** at 300 rpm for 3 hours via the high-energy ball milling method. The black colour sphere represents carbon black. The green colour sphere represents active material. The grey colour sphere represents zirconia balls.

For electrode sheet preparation via pestle and mortar, Li₂MnO₂F and carbon black were mixed for 20 minutes, after which the PTFE binder (350 µm size) was added to this mixture and further mixed by pestle and mortar for an additional 10 minutes. For preparation of electrode sheets via high energy ball milling, Li₂MnO₂F and carbon black ball milled for 3 hours at 300 rpm. Subsequently, the PTFE binder was added and mixed using a pestle and mortar for 10 minutes. Later, the electrode sheets were calendered using a calendering roll before cutting. 2032-coin type cells were fabricated, containing pellets of the cathode material mixed with conductive carbon black and PTFE (70:20:10 %wt. ratio) and Li metal chips as counter electrode and 1M LiPF₆ in EC: EMC (3:7 vol.%) as electrolyte. All mixtures and cell fabrication were done under an Ar-filled glovebox. Coin cell measurements were carried out on a Maccor Battery Tester at room temperature. The cells were subjected to a constant current of C/10 rate and were tested within voltage window of 2.0 V to 4.8 V vs. Li/Li⁺. Figure 4.18 shows the voltage vs. capacity profiles, and differential capacity (dQ/dV) plots for Li₂MnO₂F electrodes prepared via hand grinding and ball milling.

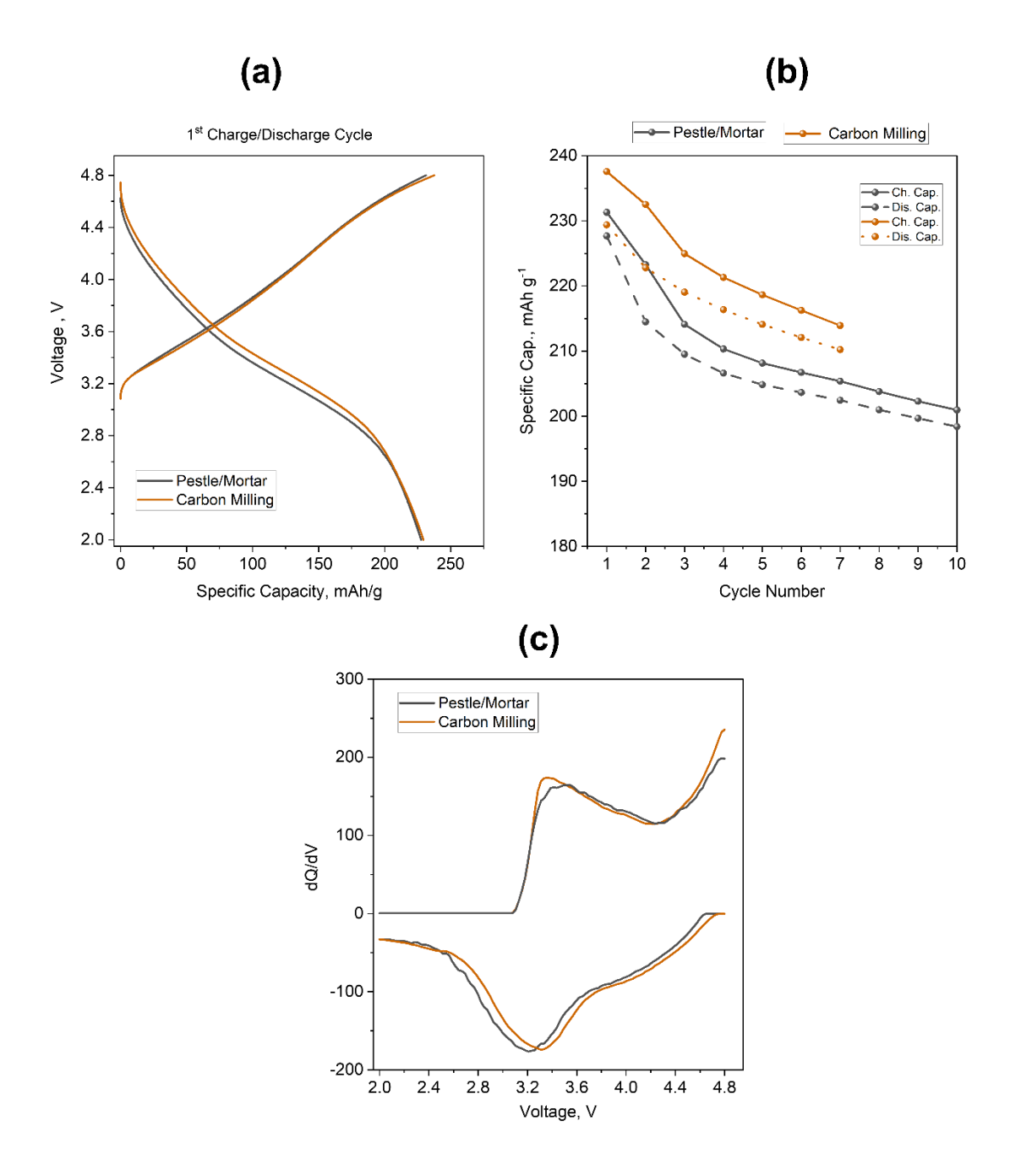


Figure 4.18 (a) The charge-discharge capacity vs. voltage curves, **(b)** the specific capacity vs. cycle number, **(c)** the differential capacity vs. voltage graph obtained from galvanostatic cycling at room temperature of the Li₂MnO₂F pellets. (active material: carbon black: PTFE in a ratio of 70:20:10). 2032-coin type cells were cycled between 2 – 4.8 V vs. Li/Li⁺ at a rate of C/10. The orange colour represents carbon milling methods, active material and carbon black are mixed at 300 rpm for 3 hours via the high-energy ball milling method. The grey colour represents active material and carbon black are mixed for 20 minutes using a pestle and mortar.

The cycling results in Figure 4.18 (a) and the differential capacity plots shown in Figure 4.18 (c) show that the first charge/discharge cycle and redox behaviour for both electrodes are very similar. Interestingly, the capacity retention over seven cycles is found to be higher for the electrodes prepared using ball milling, with a capacity of >200 mAh g⁻¹ maintained.

4.3. Conclusion

In this chapter, a systematic approach was taken to optimise the eventual electrochemical performance of the Li₂MnO₂F cathode. Key parameters in achieving this was the mechanochemical synthesis parameters, the electrode component ratio, the nature of the PTFE binder and the process for mixing the electrode components. By carefully optimising each of these parameters, this chapter has demonstrated excellent capacity retention in comparison to some of the best performance LMOF cathodes in the literature.

Chapter 5: Targeting electrochemical stability through Zrcation doping in Li₂MnO₂F (Li₂Mn_{1-v}Zr_vO₂F)

5.1. Introduction

Despite their advantages capacities, the cation disordered rock salt cathode still suffers from fading capacity during long-term cycling. Fluorination has been a partially effective way to overcome these difficulties, as demonstrated by the optimisation work presented in the previous chapters. Recently studies suggest that cathodes with disordered rock salt structures can become more stable in the presence of d⁰ ions such as Nb⁵⁺, Ti⁴⁺, W⁺⁶, Zr⁴⁺[121]. These d⁰ transition metal dopants are selected to remain redox-inactive (such as AI in NCA cathodes or Mn in NMC layered cathodes) and the high valency they exhibit has been reported to stabilise O-O bonds in rock salt oxides [122].

The objective of this chapter is to demonstrate the mechanochemical synthesis of Li₂Mn_{1-y}Zr_yO₂F, doping the Zr-cation in place of some manganese. The mechanochemical synthesis of the Li₂Mn_{1-y}Zr_yO₂F (y=0.03, 0.06, 0.10, 0.15) compositions were examined, including optimising ball milling time for Li₂Mn_{0.97}Zr_{0.03}O₂F samples, and optimising mechanosynthesis conditions for Li₂Mn_{0.97}Zr_{0.03}O₂F and Li₂Mn_{0.90}Zr_{0.10}O₂F. The crystal structure was studied by X-ray diffraction (XRD) prior to electrochemical analysis where coin cells were assembled and galvanostatic cycling performed.

5.2. Results and Discussion

5.2.1. Synthesis of Zr-doped Li₂MnO₂F

To examine the effect of Zr-cation doping on the electrochemical properties of disordered rock salt cathodes, a series of Li₂Mn_{1-y}Zr_yO₂F compounds were prepared by mechanosynthesis, in a similar approach to previous chapters. For this synthesis, Li₂O₂, MnO, ZrO₂, and LiF precursors were employed to obtain Li₂Mn_{1-y}Zr_yO₂F by mechanochemical synthesis at 750 rpm for 18 h.

Figure 5.1 shows the XRD patterns obtained of Li₂Mn_{0.97}Zr_{0.03}O₂F (red), Li₂Mn_{0.94}Zr_{0.06}O₂F (blue), Li₂Mn_{0.90}Zr_{0.10}O₂F (black), and Li₂Mn_{0.85}Zr_{0.15}O₂F (green), prepared by mechanochemical synthesis at 750 rpm for 18 hours. As with previous

chapters, each XRD pattern is characterised by the three main peaks for the Li₂MnO₃ cubic rock salt structure consistent with literature results. As shown in Figure 5.1, the XRD patterns obtained from all samples possess broad peaks with a noisy background, indicating these samples show low crystallinity with small crystallite size. The lattice parameters for Li₂Mn_{0.97}Zr_{0.03}O₂F, Li₂Mn_{0.94}Zr_{0.06}O₂F, Li₂Mn_{0.90}Zr_{0.10}O₂F, and Li₂Mn_{0.85}Zr_{0.15}O₂F samples are calculated from Bragg's law as 4.1481 Å, 4.1261 Å, 4.1262 Å, and 4.1212 Å, respectively. This decrease in lattice constant is reflected in the diffraction data where, for example, for x=0.15 there is a clear shift to higher angles in the pattern observed which indicates the Zr⁴⁺ dopant is incorporated in the crystal structure.

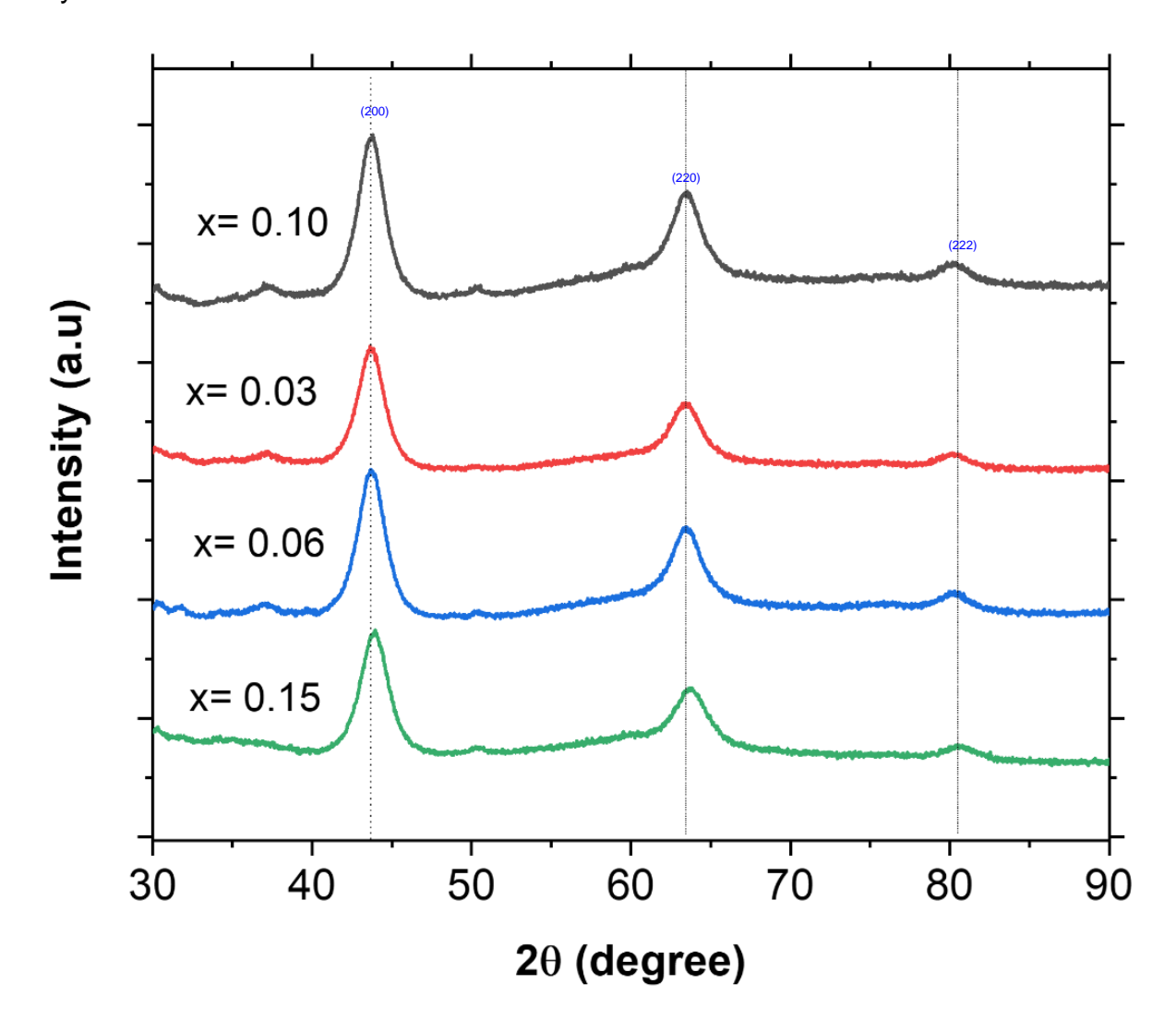


Figure 5.1 XRD patterns of Li₂Mn_{0.97}Zr_{0.03}O₂F (red), Li₂Mn_{0.94}Zr_{0.06}O₂F (blue), Li₂Mn_{0.90}Zr_{0.10}O₂F (black), and Li₂Mn_{0.85}Zr_{0.15}O₂F (green) prepared by mechanochemical synthesis at 750 rpm for 18 hours.

Scanning electron microscopy (SEM) was used to examine the morphologies and particle size prepared for Li₂Mn_{0.94}Zr_{0.06}O₂F and Li₂Mn_{0.85}Zr_{0.15}O₂F. Figure 5.2 reveals particles with a broad size distribution and quasi-spherical morphology. EDX mapping, while not a quantitative measurement, reveals a uniform distribution of all elements (shown for one sample below, but observed for other samples studied also), indicating a lack of secondary impurity phases or clustering of a dopant-rich phase in the sample (Figure 5.3).

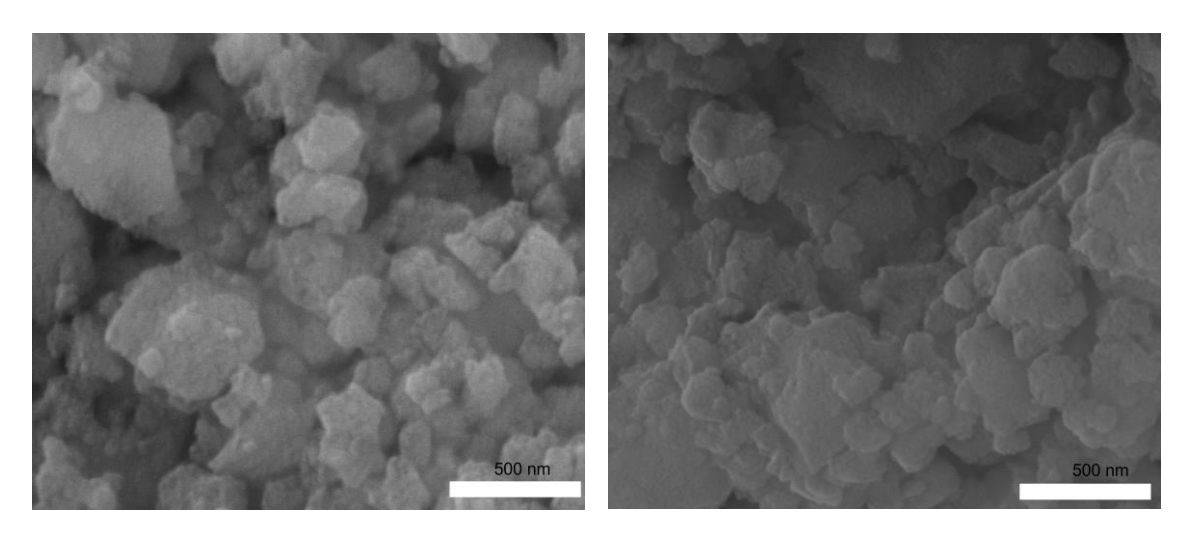


Figure 5.2 SEM images of (left) $Li_2Mn_{0.94}Zr_{0.06}O_2F$ and (right) $Li_2Mn_{0.85}Zr_{0.15}O_2F$ samples synthesised at 750 rpm for 18 hours via mechanosynthesis. The scale bar represents 500 nm.

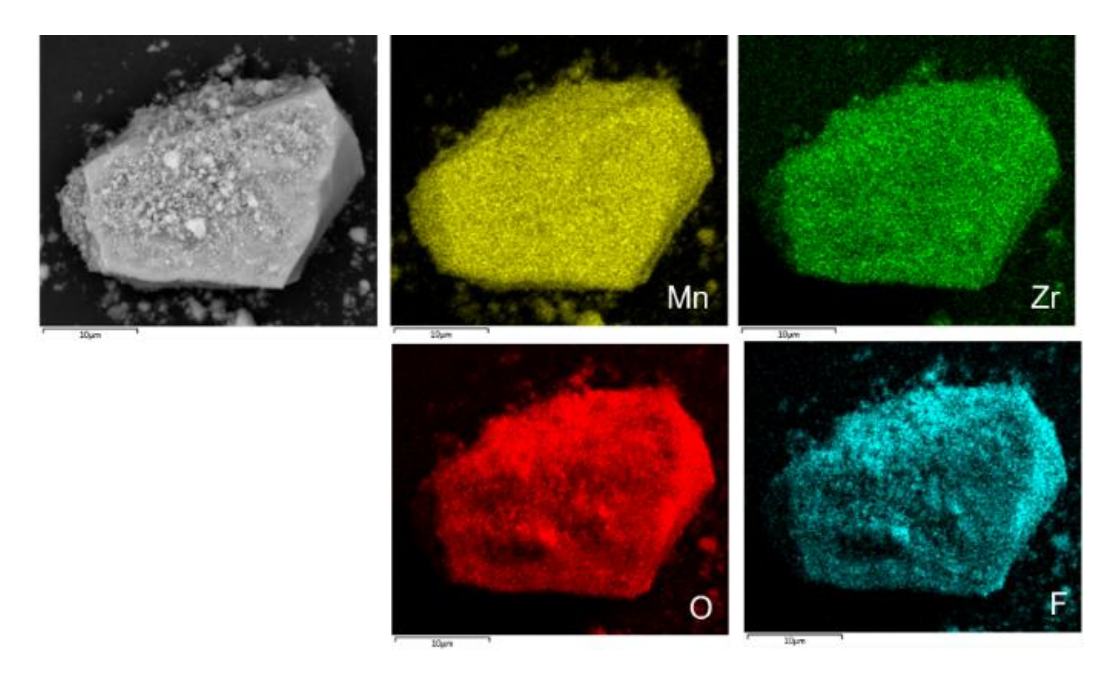


Figure 5.3 Elemental mapping images for Mn, Zr, O and F from SEM-EDX of $\text{Li}_2\text{Mn}_{0.94}\text{Zr}_{0.06}\text{O}_2\text{F}$ prepared by mechanosynthesis. The scale bar represents 5 μm .

5.2.2. Electrochemical testing of $Li_2Mn_{1-y}Zr_yO_2F$ (y=0.3, 0.6, 0.10, 0.15) cathodes

Galvanostatic cycling with potential limitation (GCPL) was performed on the Li₂Mn_{0.97}Zr_{0.03}O₂F, Li₂Mn_{0.94}Zr_{0.06}O₂F, Li₂Mn_{0.90}Zr_{0.10}O₂F, and Li₂Mn_{0.85}Zr_{0.15}O₂F cation-disordered rock salt phases to examine the effect of dopant on cathode performance prior to optimisation of the best performance phase. To prepare the cathode pellets, each active cathode material was mixed with conductive carbon black and PTFE in a ratio of 60:20:20 (Active Material: Carbon Black: 35 µm PTFE binder) using a mortar and pestle for 30 minutes. Subsequently, the electrode sheets were calendered before drying in a vacuum oven at 80°C overnight to remove any moisture or other volatiles before transferring into an argon glovebox. 2032-coin type cells were fabricated, with Li metal chips as the counter electrode and 1 M LiPF₆ in EC: EMC (3:7 vol.%) as electrolyte in an Ar-filled glovebox. Coin cell measurements were carried out on a Maccor Battery Tester at the room temperature. The charge-discharge performance of each sample was evaluated at a constant current of C/10 rate and were tested within voltage window of 2.0 V to 4.8 V vs. Li/Li⁺.

Figure 5.4 displays the charge and discharge curves obtained over 50 cycles from galvanostatic cycling for (a) $\text{Li}_2\text{Mn}_{0.97}\text{Zr}_{0.03}\text{O}_2\text{F}$, (b) $\text{Li}_2\text{Mn}_{0.94}\text{Zr}_{0.06}\text{O}_2\text{F}$, (c) $\text{Li}_2\text{Mn}_{0.90}\text{Zr}_{0.10}\text{O}_2\text{F}$, and (d) $\text{Li}_2\text{Mn}_{0.85}\text{Zr}_{0.15}\text{O}_2\text{F}$. All samples show a short plateau region between approximately 4.4 V and 4.7 V during the first charge cycle. For $\text{Li}_2\text{Mn}_{0.97}\text{Zr}_{0.03}\text{O}_2\text{F}$ (Figure 5.4(a)), the initial charge capacity is 198 mAh g⁻¹, which decreased to 183 mAh g⁻¹ for the first cycle discharge capacity. As a result, the first cycle coulombic efficiency is calculated to approximately 92 %, as depicted in Figure 5.5 (a). Subsequent cycles displayed rapid capacity fading with no apparent plateau. Over 50 cycles, $\text{Li}_2\text{Mn}_{0.97}\text{Zr}_{0.03}\text{O}_2\text{F}$ affords a discharge capacity of 117 mAh g⁻¹, with a discharge capacity retention of 63 %. The differential capacity profile for $\text{Li}_2\text{Mn}_{0.97}\text{Zr}_{0.03}\text{O}_2\text{F}$ is presented in Figure 5.6 (a), where the peak at 3.4 V is attributed to Mn-redox and the second peak in the first charge cycle observed at higher voltage is attributed to oxygen redox.

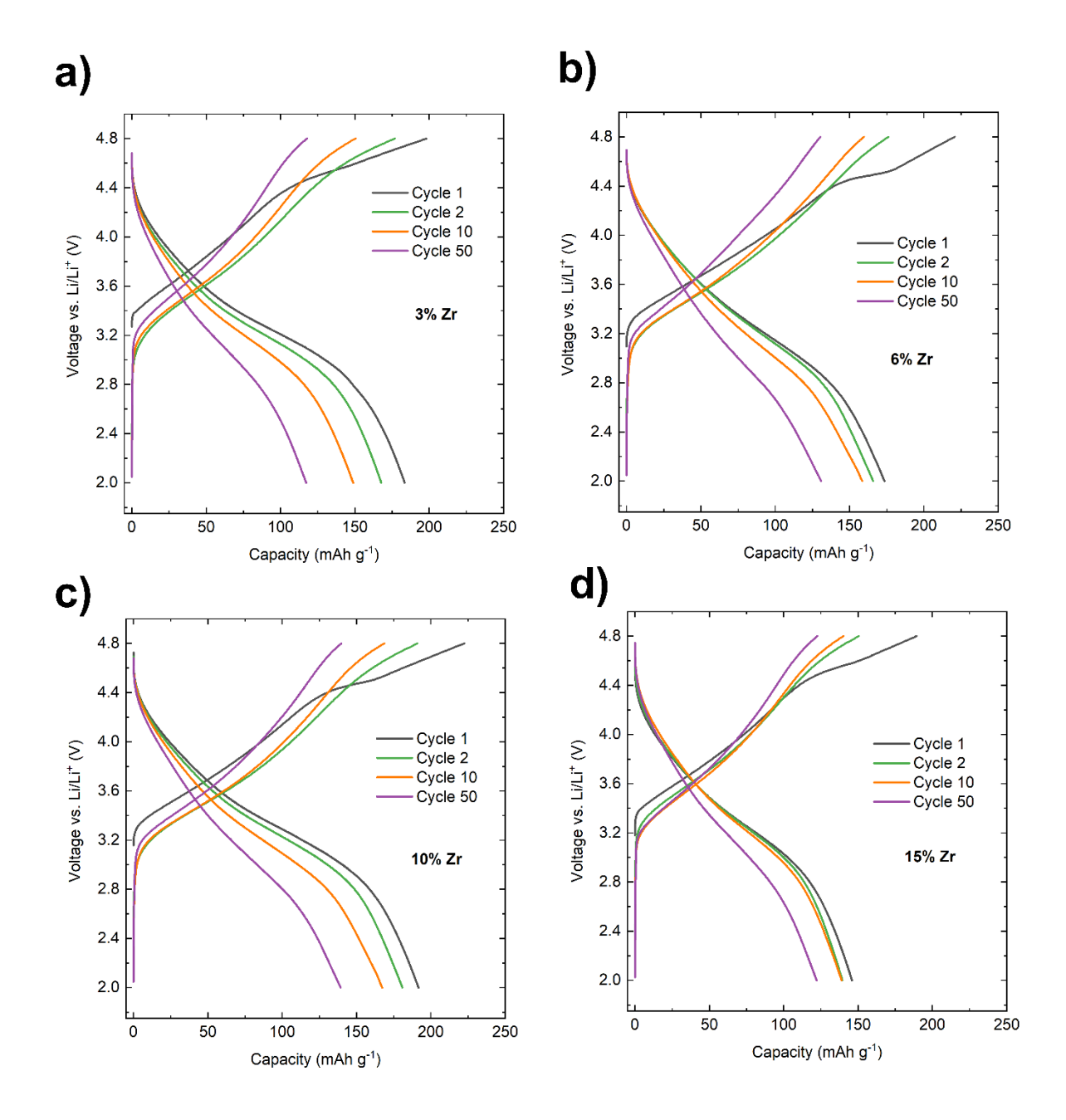


Figure 5.4 Capacity (mAh g⁻¹) vs. voltage (V) curves from galvanostatic cycling over 50 cycles at room temperature between 2-4.8 V vs. Li/Li⁺ at a C/10 rate of Li₂Mn₁₋yZr_yO₂F electrodes (active material:carbon:PTFE, 60:20:20). (a) Li₂Mn_{0.97}Zr_{0.03}O₂F, (b) Li₂Mn_{0.94}Zr_{0.06}O₂F, (c) Li₂Mn_{0.90}Zr_{0.10}O₂F, and (d) Li₂Mn_{0.85}Zr_{0.15}O₂F.

For Li₂Mn_{0.94}Zr_{0.06}O₂F (Figure 5.4(b)), the initial charge capacity was found to be 220 mAh g⁻¹ and followed by a discharge capacity of 173 mAh g⁻¹. Even though the initial charge capacity was greater than the 3% Zr sample, the sample prepared with 6% Zr dopant displayed a lower coulombic efficiency of 78 %, as shown in Figure 5.5 (b). In subsequent cycles, this coulombic efficiency increases above 95 %. The second cycle

exhibited a charge capacity of 176 mAh g⁻¹ and a discharge capacity of 165 mAh g⁻¹. Over 50 cycles, the 6% doped sample displays a discharge capacity of 130 mAh g⁻¹, with a discharge capacity retention of 75 %. The differential capacity graph of Li₂Mn_{0.94}Zr_{0.06}O₂F is presented in Figure 5.6 (b), where again a peak at 3.4 V is attributed to Mn-redox and the sharp second in the first charge cycle at higher voltage is attributed to oxygen redox.

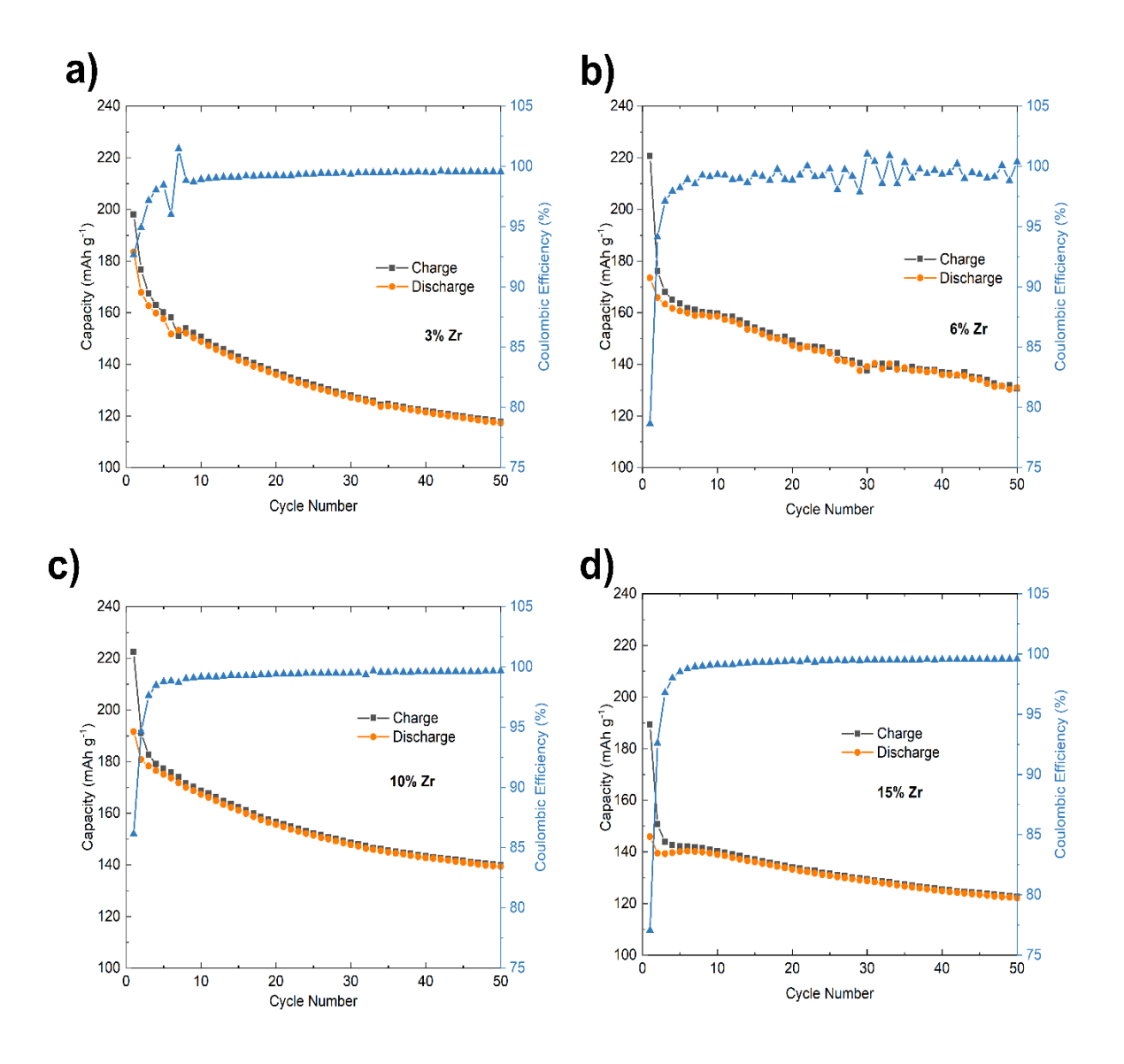


Figure 5.5 Capacity (mAh g⁻¹) and coulombic efficiency (%) vs. cycle number curves obtained from galvanostatic cycling over 50 cycles at room temperature of the Li₂Mn₁₋yZr_yO₂F electrodes (active material: carbon black: PTFE in a 60:20:20). (a) Li₂Mn_{0.97}Zr_{0.03}O₂F, (b) Li₂Mn_{0.94}Zr_{0.06}O₂F, (c) Li₂Mn_{0.90}Zr_{0.10}O₂F, and (d) Li₂Mn_{0.85}Zr_{0.15}-O₂F. 2032-coin type cells were cycled between 2-4.8 V vs. Li/Li⁺ at a rate of C/10.

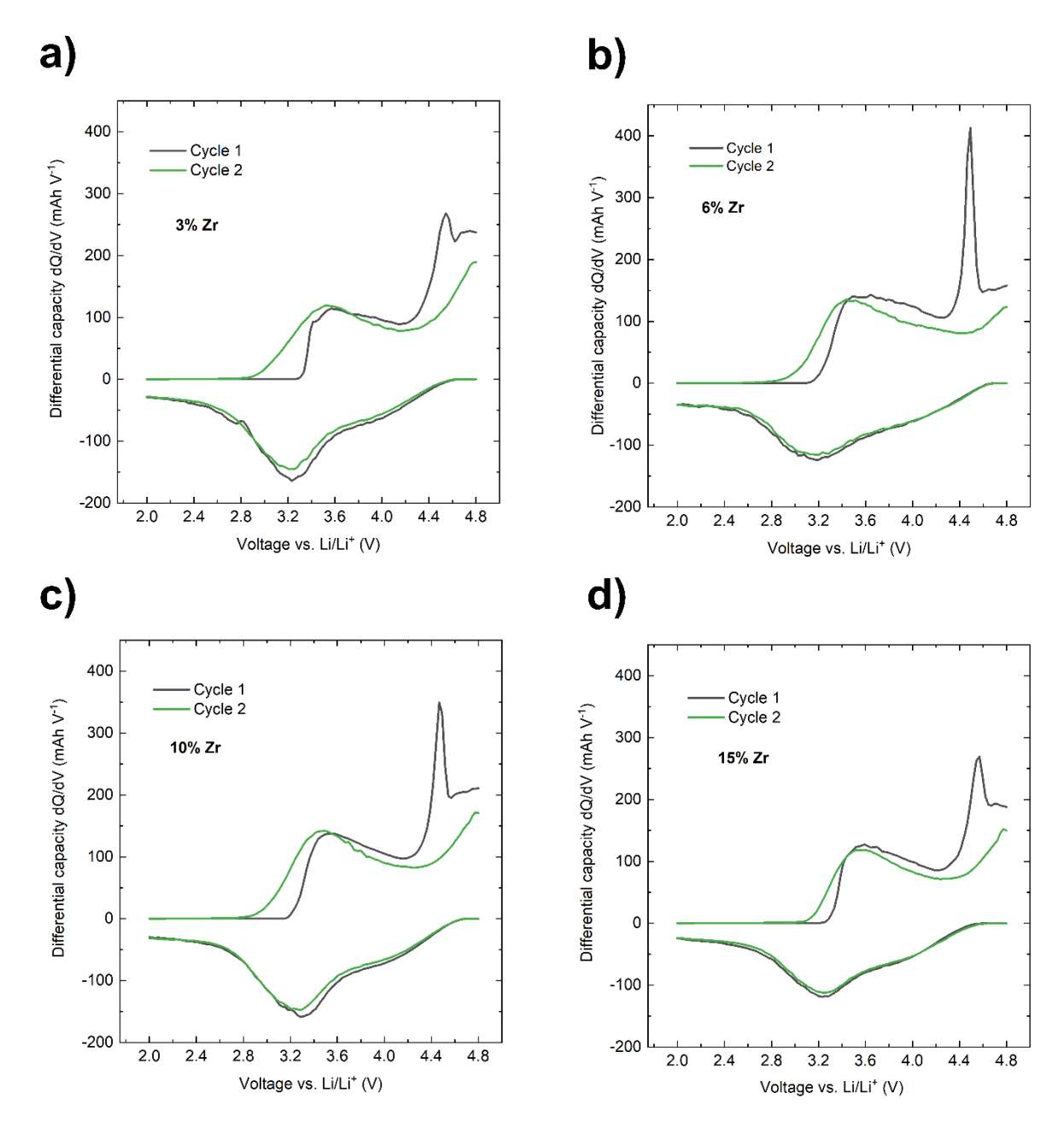


Figure 5.6 The differential capacity (mAh V⁻¹) vs. voltage (V) graph obtained from galvanostatic cycling over 2 cycles at room temperature of the $Li_2Mn_{1-y}Zr_yO_2F$ electrodes (active material: carbon black: PTFE in a 60:20:20). (a) $Li_2Mn_{0.97}Zr_{0.03}O_2F$, (b) $Li_2Mn_{0.94}Zr_{0.06}O_2F$, (c) $Li_2Mn_{0.90}Zr_{0.10}O_2F$, and (d) $Li_2Mn_{0.85}Zr_{0.15}O_2F$. 2032-coin type cells were cycled between 2-4.8 V vs. Li/Li^+ at a rate of C/10.

On moving to 10% Zr dopant, the voltage profile of Li₂Mn_{0.90}Zr_{0.10}O₂F exhibits an initial charge capacity of 222 mAh g⁻¹, with a first cycle coulombic efficiency of 86 %, as shown in Figure 5.4 (c). These initial charge and discharge results are the best

performance for this series. For the subsequent cycle, a charge capacity of 191 mAh g⁻¹ was observed, following which a discharge capacity of 180 mAh g⁻¹ was obtained. Over 50 cycles, the samples delivered a discharge capacity of 139 mAh g⁻¹, with a discharge capacity retention of 72 %. The differential capacity graph of Li₂Mn_{0.90}Zr_{0.10}O₂F is presented in Figure 5.6 (c), where peak at 3.4 V is attributed to Mn-redox and the second in the first charge cycle at higher voltage is attributed to oxygen redox. Despite the increased amount of Zr, no change in the differential capacity profile was observed.

For the highest dopant level of 15% Zr, the voltage profile of Li₂Mn_{0.85}Zr_{0.15}O₂F reveals an initial charge capacity of 189 mAh g⁻¹ and a discharge capacity of 145 mAh g⁻¹, indicating a first cycle coulombic efficiency of 77 %, as shown in Figure 5.4 (d). Although this has a similar initial charge capacity as noted for the 3 % Zr sample, it displays a lower initial discharge capacity performance. However, in long cycle performance, 15 % Zr sample exhibited a higher discharge capacity with increasing Zr amount. Over 50 cycles, Li₂Mn_{0.85}Zr_{0.15}O₂F displays a 122 mAh g⁻¹ of discharge capacity, with a discharge capacity retention of 84 %. The differential capacity graph of, Li₂Mn_{0.85}Zr_{0.15}O₂F is presented in Figure 5.4 (d), revealing similar peaks are observed as in the other samples.

5.2.3. Optimising mechanochemical synthesis time for Li₂Mn_{0.97}Zr_{0.03}O₂F

While the optimised mechanochemical synthesis parameters which were identified in Chapter 4 for Li₂MnO₂F were initially used here, the introduction of a small amount of dopant can affect the reaction pathway. Therefore, the effect of the ball milling time on the synthesis of Li₂Mn_{0.97}Zr_{0.03}O₂F was investigated. For this synthesis, Li₂O₂, MnO, ZrO₂ and LiF precursors were employed to obtain Li₂Mn_{0.97}Zr_{0.03}O₂F by mechanosynthesis at 750 rpm during three different ball milling times: 12 hours, 18 hours, and 36 hours. The effect of ball milling time on the electrochemical performance of Li₂Mn_{0.97}Zr_{0.03}O₂F was investigated with galvanostatic cycling. To prepare the cathode pellets, each active cathode materials was mixed conductive carbon black and PTFE in a ratio of 70:20:10 (Active material: Carbon Black: Binder). The mixture of Li₂Mn_{0.97}Zr_{0.03}O₂F active materials and carbon black was ball milled for 3 hours at 30rpm. Subsequently, PTFE binder (350 µm particle size) was added and mixed using a pestle and mortar for 10 minutes. As a final step, the electrode sheets were

calendered using a calendaring roll pressure machine to minimize porosity on the electrode surface. 2032-coin type cells were fabricated, with Li metal chips as the counter electrode and 1 M LiPF₆ in EC: EMC (3:7 vol.%) as electrolyte in an Ar-filled glovebox. Coin cell measurements were carried out on a Maccor Battery Tester at the room temperature. The charge-discharge performance of each sample was evaluated at a constant current of C/10 rate and were tested within voltage window of 2.0 V to 4.8 V vs. Li/Li⁺.

Figure 5.7 shows the charge and discharge capacity curves obtained during five cycles from galvanostatic cycling of the Li₂Mn_{0.97}Zr_{0.03}O₂F (LMZOF) prepared after (a) 12 hours, (b) 18 hours, and (c) 36 hours of ball milling. The LMZOF-12h (Figure 5.7 (a)) exhibits a large initial charge capacity of 243 mAh g⁻¹ and followed by a discharge capacity of 208 mAh g⁻¹. This indicates a low first cycle columbic efficiency of 85 %, as shown in Figure 5.8 (a). The second cycle delivers a higher coulombic efficiency of 96 %, with a charge capacity of 213 mAh g⁻¹ and a discharge capacity of 205 mAh g⁻¹. Although the discharge capacity decreases between first and second cycle, during seven cycles the discharge capacity remains approximately 200 mAh g⁻¹ with discharge capacity retention of 96 %.

The differential capacity graph of LMZOF-12 h is presented in Figure 5.9 (a), where the peak at 3.4 V is attributed to Mn-redox and the second in the first charge cycle at higher voltage is attributed to oxygen redox. Interestingly, a small peak was observed at 4.2 V. This peak disappeared in the second cycle and reappeared in the fourth cycles as a broad peak. The nature of this peak is not completely understood, but future experiments using X-ray absorption spectroscopy to probe oxidation state changes *operando* would be helpful in gaining further insight. The LMZOF-18h shows an initial charge capacity of 249 mAh g⁻¹ and a discharge capacity of 251 mAh g⁻¹, as shown in Figure 5.7 (b). The second cycle exhibits a charge capacity of 244 mAh g⁻¹ and discharge capacity of 230 mAh g⁻¹. The indicates a columbic efficiency of 97 %, as shown in Figure 5.8 (c). Over seven cycles, the discharge capacity remains approximately 219 mAh g⁻¹ with discharge capacity retention of 87 %. With the result, LMZOF-18h example was the best performing example for the first seven cycles. The differential capacity graph of LMZOF-18h is presented in Figure 5.8 (b), where peak at 3.4 V is attributed to Mn-redox and the second in the first charge cycle at higher

voltage is attributed to oxygen redox. Unlike LMZOF-12h samples, no peak at 4.2 V point was observed here.

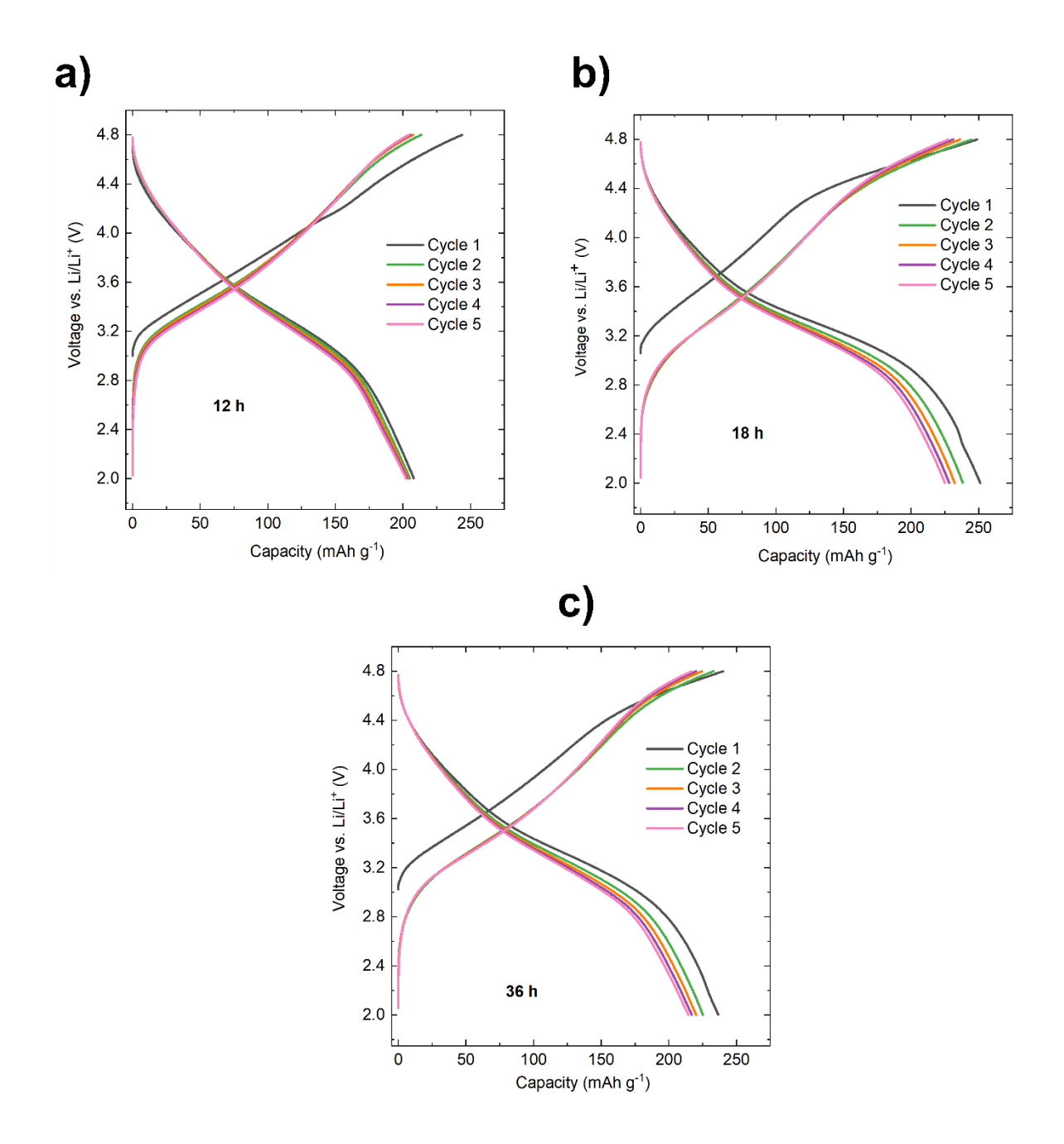


Figure 5.7 The charge-discharge capacity (mAh g⁻¹) and coulombic efficiency (%) vs. cycle number curves obtained from galvanostatic cycling over 7 cycles at room temperature of the Li₂Mn_{0.97}Zr_{0.03}O₂F electrodes (active material: carbon black: PTFE in a 70:20:10). a) 12 hours, b) 18 hours, and c) 36 hours. 2032-coin type cells were cycled between 2-4.8 V vs. Li/Li⁺ at a rate of C/10.

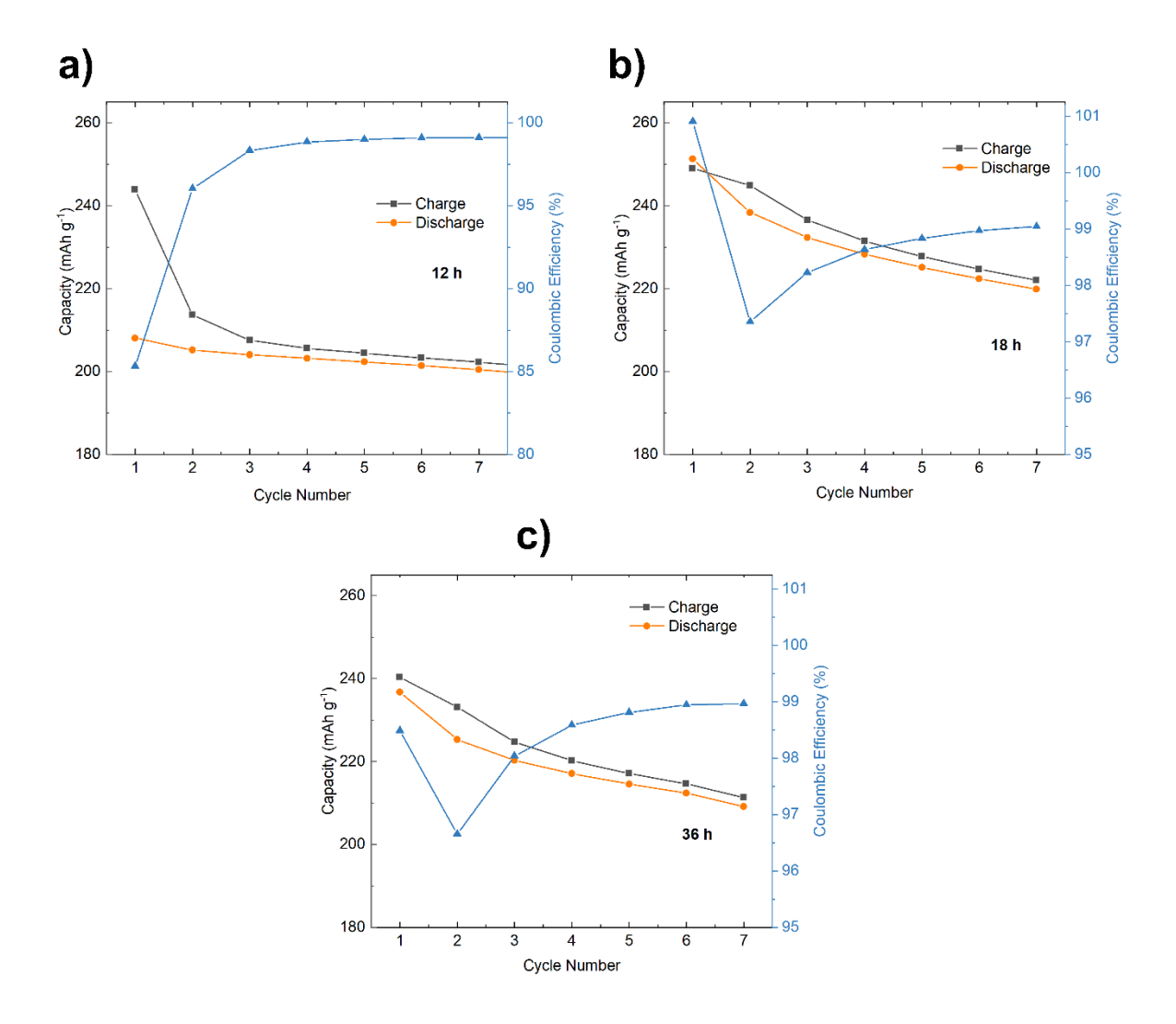


Figure 5.8 The charge-discharge capacity (mAh g⁻¹) and coulombic efficiency (%) vs. cycle number curves obtained from galvanostatic cycling over 7 cycles at room temperature of the Li₂Mn_{0.97}Zr_{0.03}O₂F electrodes (active material: carbon black: PTFE in a 70:20:10). a) 12 hours, b) 18 hours, and c) 36 hours. 2032-coin type cells were cycled between 2-4.8 V vs. Li/Li⁺ at a rate of C/10.

In Figure 5.7 (c), the LMZOF-36h displays an initial charge capacity of 240 mAh g⁻¹ and a discharge capacity of 236 mAh g⁻¹. This indicates a columbic efficiency of 98 %, as shown in Figure 5.8 (c). The second cycle delivers a charge capacity of 233 mAh g⁻¹ and discharge capacity of 225 mAh g⁻¹, along with a coulombic efficiency of 96 %. Over seven cycles, the discharge capacity 209 mAh g⁻¹ with a discharge capacity retention of 88 %. The differential capacity graph of LMZOF-36h is presented in Figure 5.9 (c). It shows a similar pattern to that of LMZOF-18h, where peak at 3.4 V is

attributed to Mn-redox and the second in the first charge cycle at higher voltage is attributed to oxygen redox.

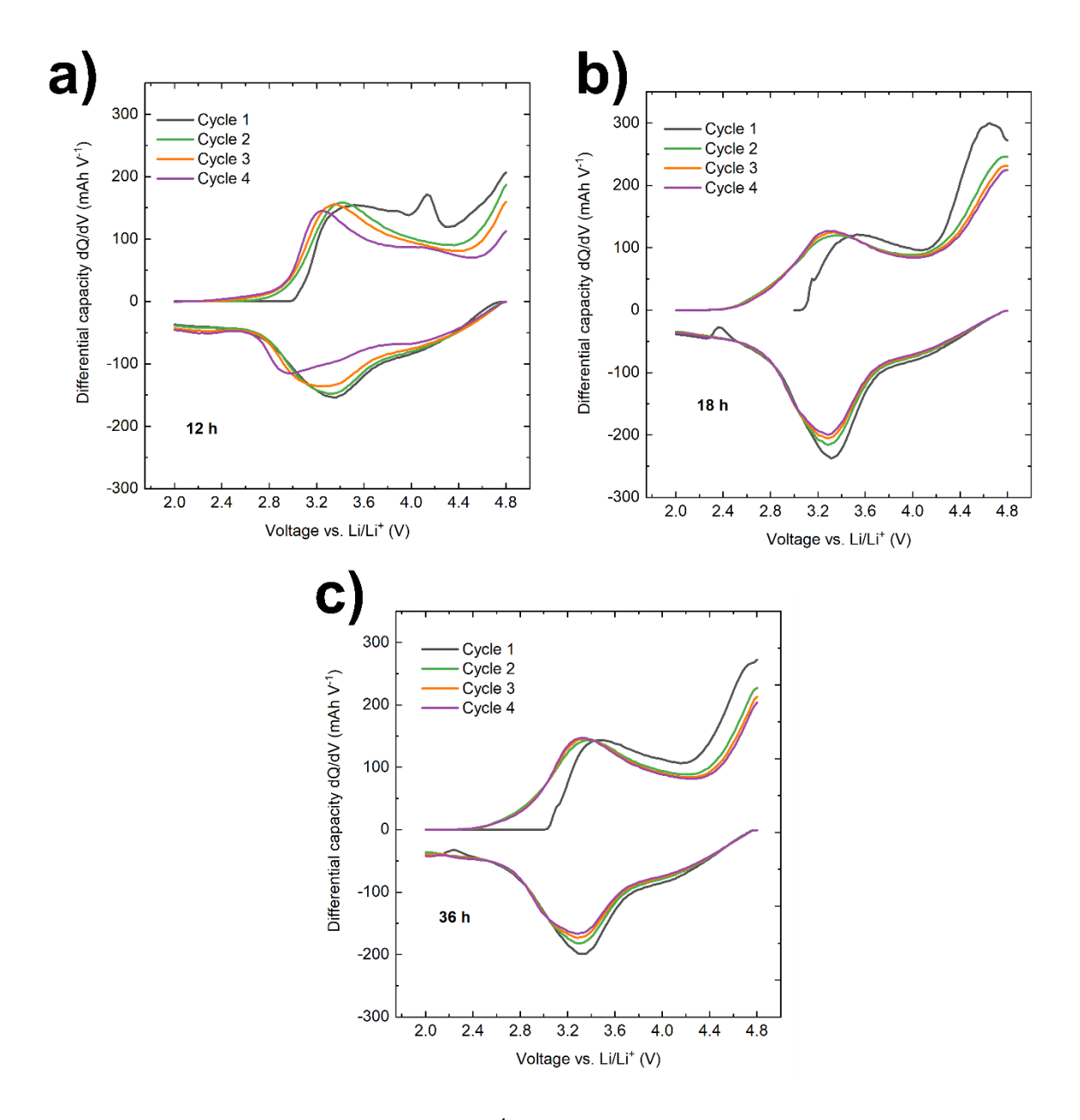


Figure 5.9 Differential capacity (mAh V⁻¹) vs. voltage (V) obtained from galvanostatic cycling over 5 cycles at room temperature of the Li₂Mn_{0.97}Zr_{0.03}O₂F electrodes (active material: carbon black: PTFE in a 70:20:10)). a) 12 hours, b) 18 hours, and c) 36 hours. 2032-coin type cells were cycled between 2-4.8 V vs. Li/Li+ at a rate of C/10.

5.2.4. Optimising mechanochemical synthesis for Li₂Mn_{1-y}Zr_yO₂F (y=0.03 and 0.10)

In a similar manner to the optimisation steps taken in Chapter 4, a two-step mechanochemical synthesis method was applied for the preparation of Li₂Mn_{1-y}Zr_yO₂F (y=0.03 and 0.10) to explore any influence this had on the final electrochemical performance. All samples were prepared using 750 rpm ball milling and two different synthesis time as (9h+9h) and (12h+12h). Figure 5.10 shows the XRD patterns obtained of the products after two-step mechanosynthesis of Li₂Mn_{0.97}Zr_{0.03}O₂F at 750 rpm for 9h+9h and 12h+12h. The XRD patterns confirmed the successful synthesis of the compounds in a cubic rock salt structure and the patterns are consistent with the previous section results. As with previous diffraction patterns, there are broad peaks observed indicating low crystallinity. Figure 5.11 shows the XRD patterns obtained of the products after two-step mechanosynthesis of Li₂Mn_{0.90}Zr_{0.10}O₂F at 750 rpm for 9h+9h and 12h+12h. Again, similar XRD patterns, consistent with previous observations for Li₂MnO₂F, are obtained.

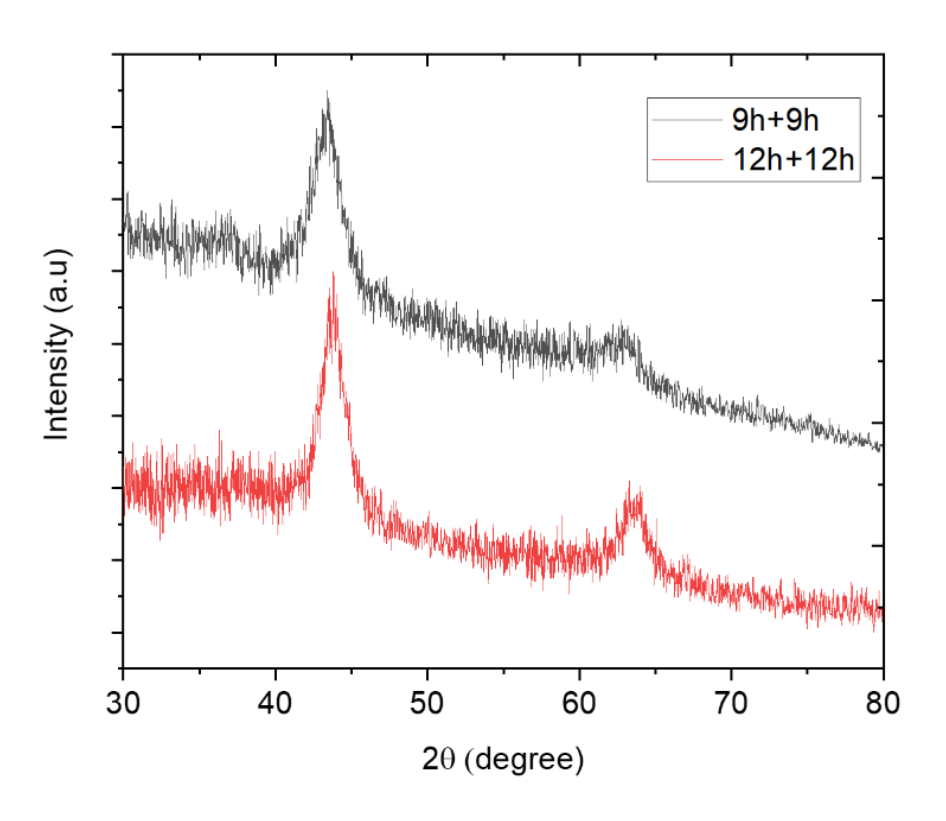


Figure 5.10 XRD patterns of the obtained during two-step mechanosynthesis of Li₂Mn_{0.97}Zr_{0.03}O₂F at 750 rpm for 9h+9h (black) and 12h+12h (red).

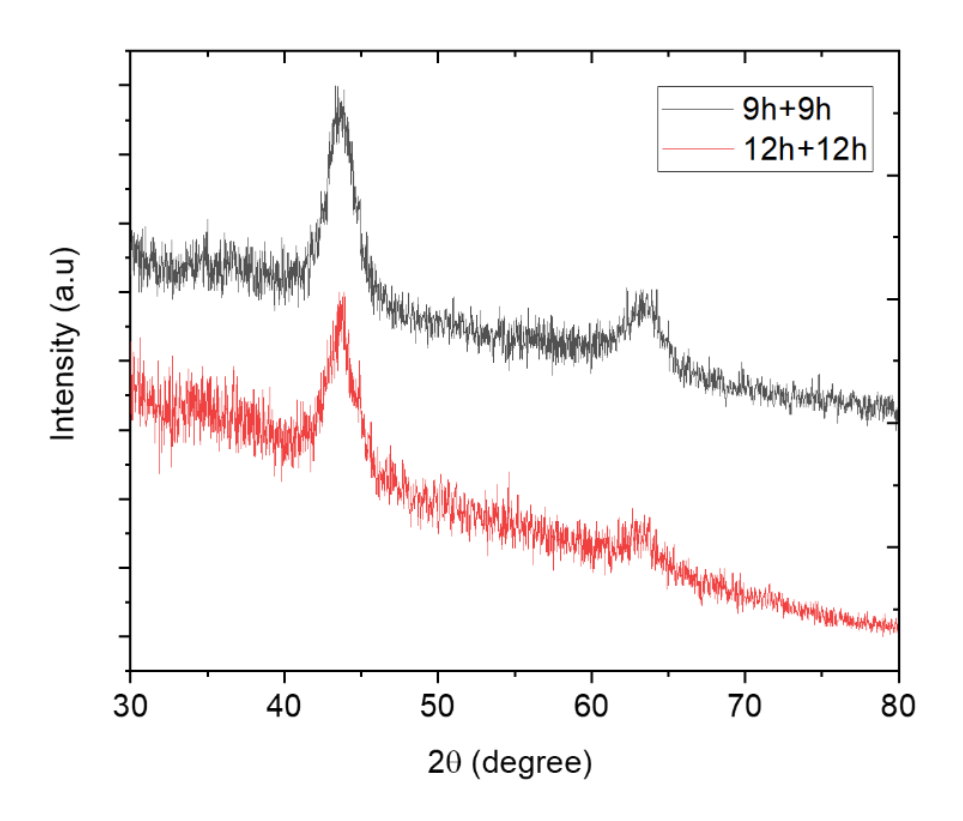


Figure 5.11 XRD pattern of the obtained during two-step mechanosynthesis of Li₂Mn_{0.90}Zr_{0.10}O₂F at 750 rpm for 9h+9h (black) and 12h+12h (red).

To prepare the cathode pellets, each active cathode materials was mixed conductive carbon black and PTFE in a ratio of 70:20:10 (Active material: Carbon Black: Binder). The mixture of Li₂Mn_{1-y}Zr_yO₂F (y=0.03 and 0.10) active material and carbon black was ball milled for 3 hours at 30rpm. Subsequently, PTFE binder (350 µm particle size) was added and mixed using a pestle and mortar for 10 minutes. As final step, the electrode sheets were calendered using a calendaring roll pressure machine to minimize porosity on the electrode surface. 2032-coin type cells were fabricated, with Li metal chips as the counter electrode and 1 M LiPF₆ in EC: EMC (3:7 vol.%) as electrolyte in an Ar-filled glovebox. Coin cell measurements were carried out on a Maccor Battery Tester at the room temperature. The charge-discharge performance of each sample was evaluated at a constant current of C/10 rate and were tested within voltage window of 2.0 V to 4.8 V vs. Li/Li⁺.

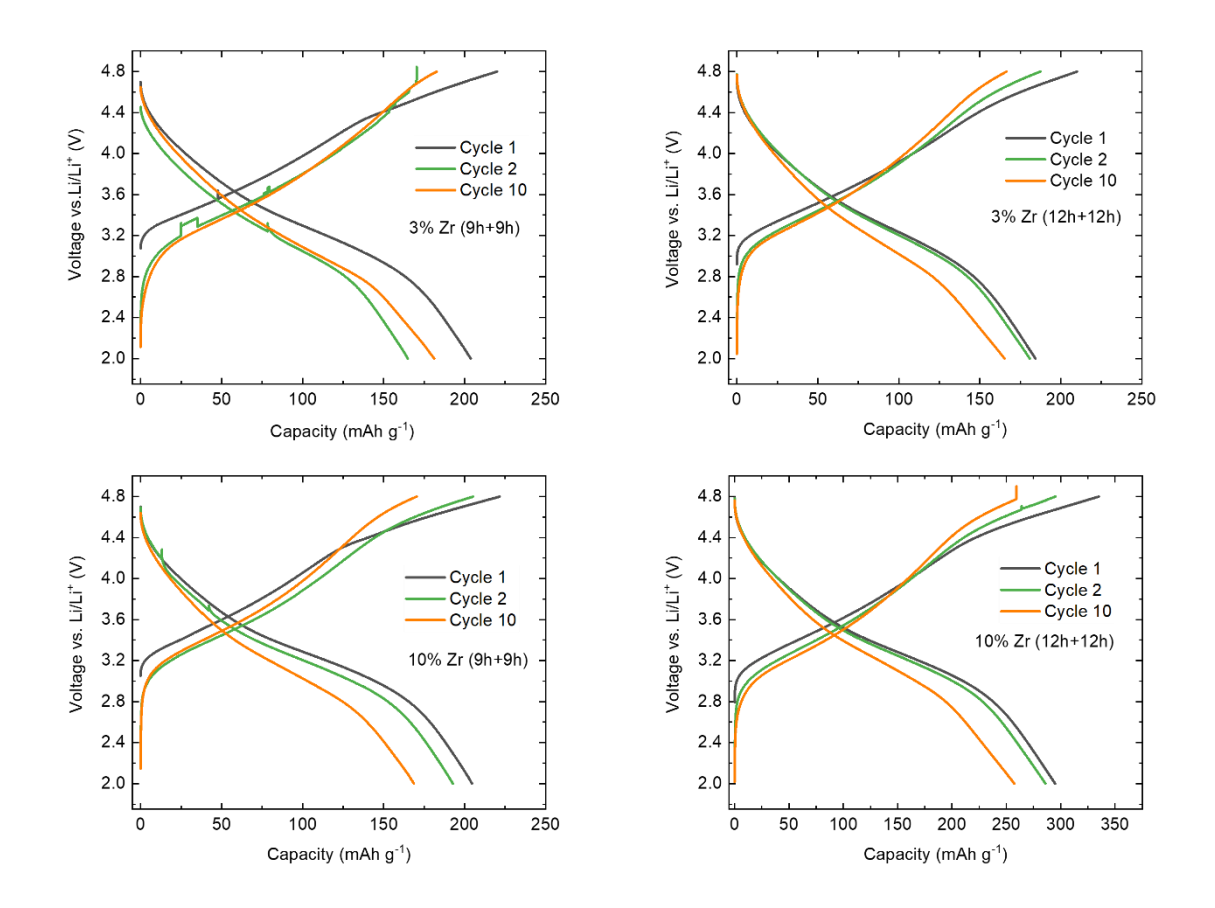


Figure 5.12 The charge-discharge capacity (mAh g⁻¹) vs. voltage (V) curves obtained from galvanostatic cycling over 10 cycles at room temperature of the Li₂Mn_{0.97}Zr_{0.03}O₂F (a) 9h+9h, (b) 12h+12h and Li₂Mn_{0.90}Zr_{0.10}O₂F (c) 9h+9h, (d) 12h+12h electrodes (active material: carbon black: PTFE in a 70:20:10)). 2032-coin type cells were cycled between 2-4.8 V vs. Li/Li⁺ at a rate of C/10.

Figure 5.12 (a) exhibits an initial charge capacity of 220 mAh g⁻¹ and discharge capacity of 203 mAh g⁻¹ for 3% Zr (9h+9h), resulting in a columbic efficiency of 92 %, as shown in Figure 5.13 (a). The second cycle displays low-capacity retention of 80 %, along with a discharge capacity of 164 mAh g⁻¹ before recovering in the third cycle to deliver a charge capacity of 200 mAh g⁻¹, with a discharge capacity of 193 mAh g⁻¹. This anomalous result may be related to cell assembly issues and future work will examine this in more detail. Over 10 cycles, this sample delivered a discharge capacity of 181 mAh g⁻¹, with a discharge capacity retention of 89 %. With increasing ball milling time 3 % Zr (12h+12h) samples show a lower initial charge capacity of 210 mAh g⁻¹ and followed by a discharge capacity of 184 mAh g⁻¹, as shown in Figure 5.12 (b). This

results in a first cycle coulombic efficiency of 87 % in Figure 5.13 (b). In subsequent cycles, the coulombic efficiency increases and remains above 96 %. Discharge capacities of 165 mAh g⁻¹ over 10 cycles are observed. The differential capacity plots of all samples are shown in Figure 5.14, where the peak observed at 3.4 V is attributed to Mn-redox and the second in the first charge cycle at higher voltage is attributed to oxygen redox.

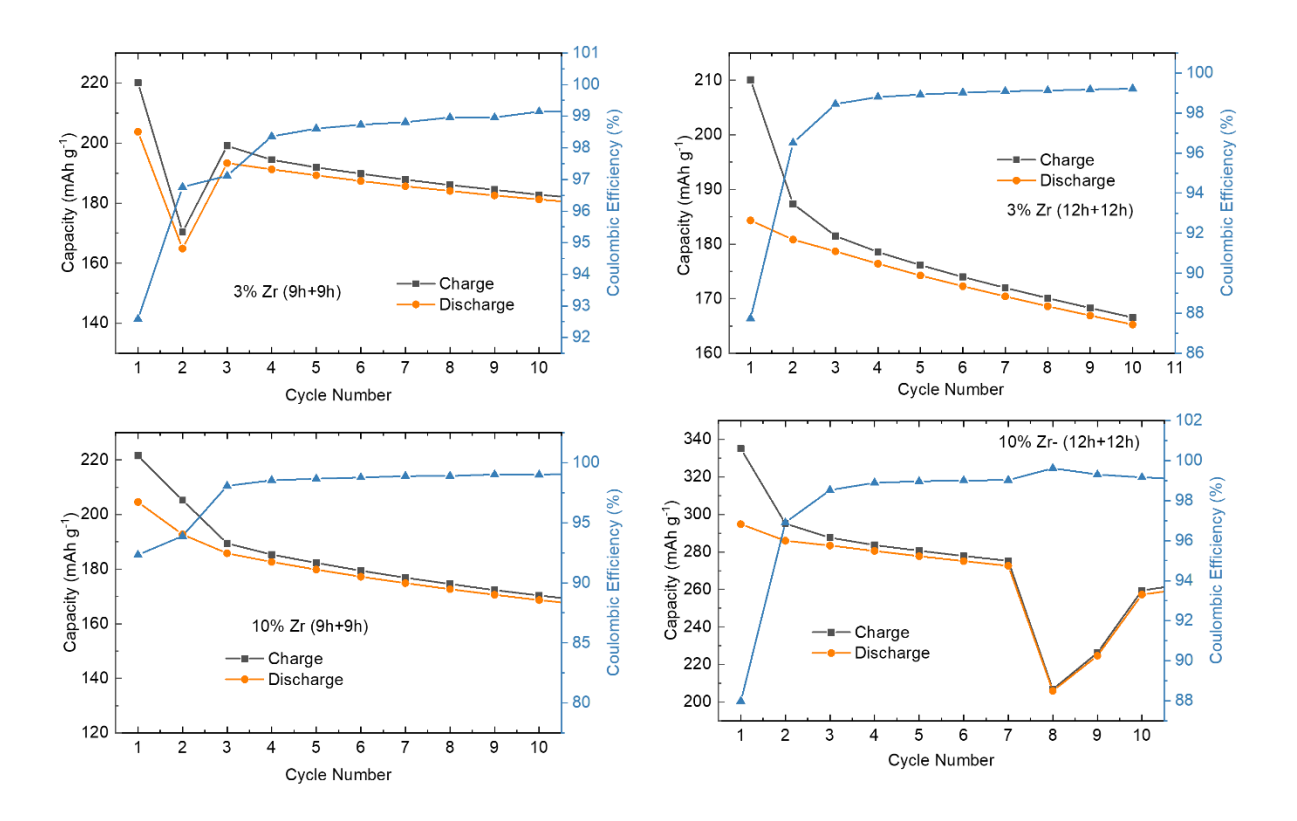


Figure 5.13 The charge-discharge capacity (mAh g⁻¹) and coulombic efficiency (%) vs. cycle number curves obtained from galvanostatic cycling over 10 cycles at room temperature of the Li₂Mn_{0.97}Zr_{0.03}O₂F (a) 9h+9h, (b) 12h+12h and Li₂Mn_{0.90}Zr_{0.10}O₂F (c) 9h+9h, (d) 12h+12h electrodes (active material: carbon black: PTFE in a 70:20:10). 2032-coin type cells were cycled between 2-4.8 V vs. Li/Li⁺ at a rate of C/10. Li₂Mn_{0.97}Zr_{0.03}O₂F

The cycling results for the 10 % Zr (9h+9h) sample are shown in Figure 5.12 (c). The voltage curve of the samples exhibits an initial charge capacity of 221 mAh g⁻¹ and a discharge capacity of 204 mAh g⁻¹. While this shows the same initial capacity as the 3

% Zr (9h+9h) sample, a higher discharge capacity is noted. With increasing amount of Zr-cation doping, stabilisation of the disordered structure may be provided, protecting it against degradation and providing a more effective Li diffusion.

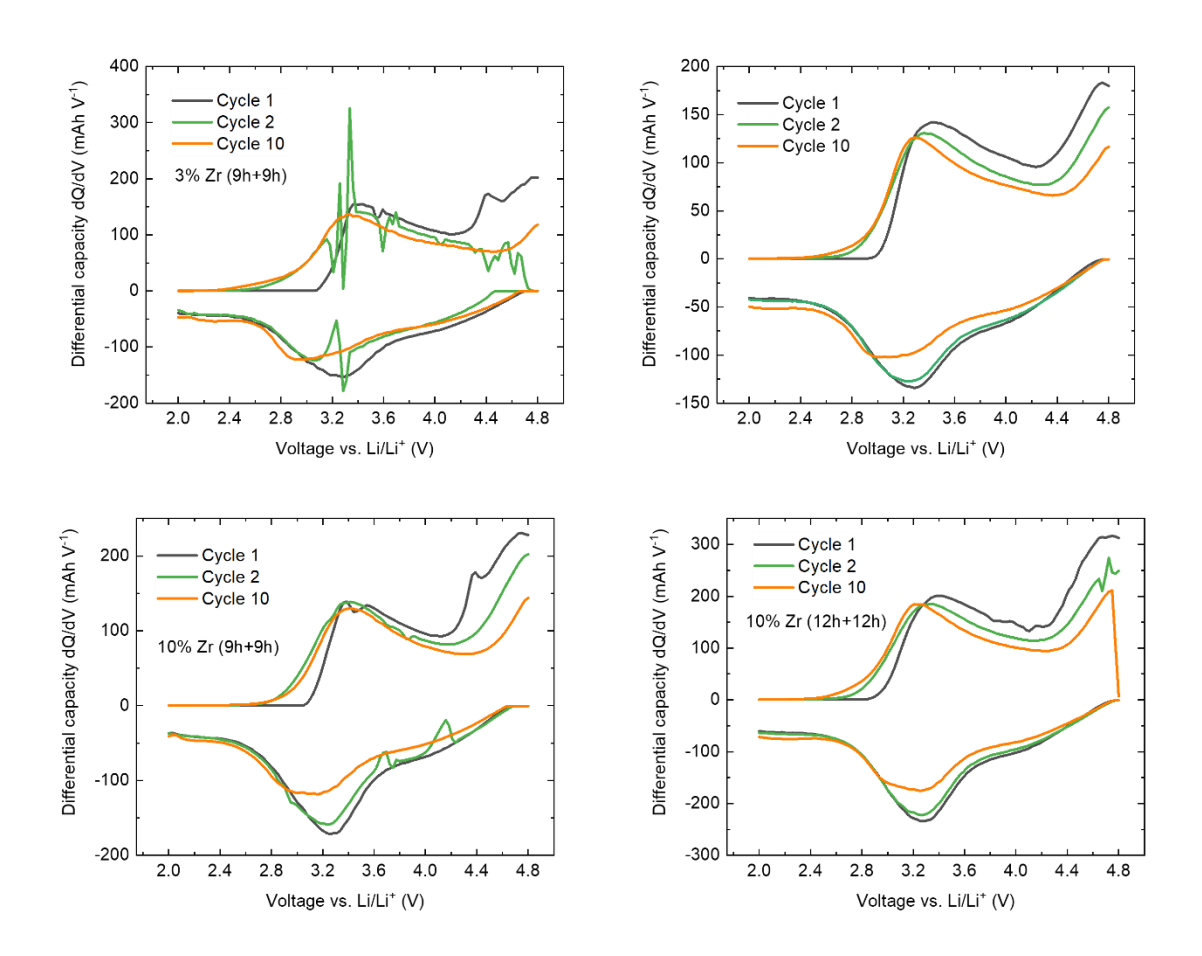


Figure 5.14 The differential capacity (mAh V⁻¹) vs. voltage (V) graph obtained from galvanostatic cycling over 10 cycles at room temperature of the Li₂Mn_{0.97}Zr_{0.03}O₂F (a) 9h+9h, (b) 12h+12h and Li₂Mn_{0.90}Zr_{0.10}O₂F (c) 9h+9h, (d) 12h+12h electrodes (active material: carbon black: PTFE in a 70:20:10)). 2032-coin type cells were cycled between 2-4.8 V vs. Li/Li⁺ at a rate of C/10.

In comparison to the 3% Zr samples, with increasing the ball milling time 10 % Zr (12h+12h) samples delivered excellent first charge and discharge capacities. The 10 % Zr (12h+12h) samples (Figure 5.6 (d)) exhibits a large initial charge capacity of 335 mAh g⁻¹ and followed by a discharge capacity of 294 mAh g⁻¹. The second cycle coulombic efficiency is found to be 96 %, with a charge capacity of 295 mAh g⁻¹ and a

discharge capacity of 285 mAh g⁻¹. Over 10 cycles, this sample delivers 257 mAh g⁻¹ of discharge capacity, with a discharge capacity retention of 87 %. Although the discharge capacity decreases between the first and second cycle, over seven cycles the discharge capacity remains approximately 200 mAh g⁻¹ with discharge capacity retention of 96 %. These are amongst some of the highest reports for these materials and demonstrate the effectiveness of the Zr⁴⁺ cation dopant in stabilising electrochemical performance.

5.3. Conclusion

In this work, cation disordered manganese-based rock salt Li₂Mn_{1-y}Zr_yO₂F (y=0.03, 0.06, 0.10, 0.15) oxyfluoride cathodes for Li-ion batteries were prepared using a mechanochemical synthesis method. The structural and morphological characterisation were analysed using XRD, SEM and EDX. All samples showed a broadened peak with a noisy background, indicating these samples show low crystallinity. The electrochemical performance of these samples was then measured by galvanostatic cycling at C/10 between 2-4.8V. 3% Zr, 6% Zr, and 10% Zr samples showed an increase in discharge capacity with Zr content, along with a discharge capacity of 183 mAh g⁻¹, 173 mAh g⁻¹, and 191 mAh g⁻¹, respectively. Further optimisation of the ball milling approach delivered and Li₂Mn_{0.90}Zr_{0.10}O₂F with discharge capacities of >200 mAh g⁻¹ after seven cycles, indicating this is a promising route to optimising high capacity disordered cathodes.

Chapter 6: Overall Conclusion and Future Work

High capacity cathodes based on disordered rock salt lithium manganese oxyfluorides represent a promising class of cathode materials for high energy density Li-ion batteries. In addition to delivering high initial specific capacities, they also offer an alternative to more mature cathode chemistries which rely heavily on non-earth abundant, expensive and toxic elements such as cobalt and nickel. However, considerable challenges remain in retaining that high capacity with long term cycling and overcoming the issues with severe capacity fade.

This thesis investigated the mechanochemical synthesis of a series of lithium manganese oxyfluorides and further optimisation of the cathode formulation with the objective of improving the electrochemical cycling performance. Initial experiments were carried out on a series of Li₂MnO_{3-x}F_x (x=0, 0.2, 0.8, 1, 1.2), where the partial substitution of fluorine in place of oxygen can permit access to the manganese redox activity through charge balancing. These materials were characterised by X-ray diffraction, electrochemical cycling in half coin cells and muon spin spectroscopy (µ+-SR). This represents the first study of this series of materials by µ+-SR and interestingly shows a reduction in the activation barrier for Li⁺ ion diffusion with fluorine substitution. The results here indicate that the addition of fluorine permits easier passage of Li⁺ ions in these materials. Future work will include investigating how this behaviour changes as a function of state of charge. Recently, our group have developed an operando muon spectroscopy cell and our plans include submission of a new proposal to the ISIS Neutron and Muon source to investigate how ion mobility in these oxyfluorides changes during battery operation. From this first results chapter, the best electrochemical performance is observed for Li₂MnO₂F and this sample was selected for further optimisation.

The reaction conditions for high energy ball milling can significantly affect the final material morphology, structure and electrochemical performance. There is a strong synthesis-structure-property relationship and to arrive at a better performing cathode material, it is necessary to consider how the choice of synthesis parameters affects the final material morphology and structure. Chapter 4 has explored this in detail and

found that optimising the ball milling time as well as the starting materials used can have a significant effect on electrochemical performance. The work presented in this chapter also investigates the selection of binder used to prepare the final cathode film. Traditionally, a PTFE polymer is employed but there is little detail in the literature as to the nature of this binder. By studying different PTFE particle sizes and optimising the active material/carbon/binder ratio, Chapter 4 has shown that the electrode capacity can be enhanced and further improvements to cycling stability have been observed for Li₂MnO₂F. The results here show that by careful consideration of these experimental parameters, we can arrive at a cathode which demonstrates excellent capacity retention in comparison to some of the best performance LMOF cathodes in the literature.

Following on from this, the hypothesis of d⁰ high valent dopants stabilising oxygen redox was tested in Li₂MnO₂F. For this, Zr⁴⁺ was selected and a series of cation disordered manganese-based rock salt Li₂Mn_{1-y}Zr_yO₂F (y=0.03, 0.06, 0.10, 0.15) oxyfluoride cathodes prepared via mechanochemical synthesis. By following a similar methodical approach to optimisation, it was observed that Li₂Mn_{0.90}Zr_{0.10}O₂F could deliver discharge capacities in excess of 200 mAh g⁻¹, indicating this is a promising route to optimising high capacity disordered cathodes.

It was possible to carry out some total scattering experiments on a few samples in this thesis. Future work will include further total scattering investigations to link local order with ion diffusion insights from muon spectroscopy. Preliminary work was also carried out using X-ray absorption spectroscopy to examine cycled cathodes to understand how the transition metal oxidation state may change at different states of charge (results not included in this thesis). Future work will include full analysis of these results.

The observation that Zr⁴⁺ doping can result in highest discharge capacity and better capacity retention is exciting and opens the door for further examination of other d0 cation dopants in these materials. The results from this thesis take an important step in improving performance and stability of disordered rock salt cathodes.

7. References

- 1. United Nations/Framework Convention on Climate Change (2015) Adoption of the Paris Agreement, 21st Conference of the Parties, Paris: United Nations.
- 2. Commission, E., *Transport 2050: Commission outlines ambitious plan to increase mobility and reduce emissions.* online.
- 3. Albuquerque, F.D.B., et al., *Greenhouse gas emissions associated with road transport projects: current status, benchmarking, and assessment tools.*Transportation Research Procedia, 2020. **48**: p. 2018-2030.
- 4. Mentes, M., Sustainable development economy and the development of green economy in the European Union. Energy, Sustainability and Society, 2023. **13**(1): p. 32.
- 5. Sacchi, R., et al., When, where and how can the electrification of passenger cars reduce greenhouse gas emissions? Renewable and Sustainable Energy Reviews, 2022. **162**: p. 112475.
- 6. Pancaldi, G., Volta: Science and Culture in the Age of Enlightenment. 2003.
- 7. Sistrunk, T.O., *John Frederic Daniell.* Journal of Chemical Education, 1952. **29**(1): p. 26.
- 8. Sprague, R., *An analysis of current battery technology and electric vehicles.* Journal of Undergraduate Research, 2015. **5**(1): p. 70-75.
- 9. Cove, G., *Batteries-past, present and future*. Physics in Technology, 1988. **19**(4): p. 141.
- Nitin Kotkunde, K.V., et al., Life Cycle Assessment of Nickel Cadmium Battery. IOP Conference Series: Materials Science and Engineering, 2021. 1123(1): p. 012022.
- 11. Smithrick, J.J. and P.M. O'Donnell, *Nickel-hydrogen batteries-An overview.* Journal of propulsion and power, 1996. **12**(5): p. 873-878.
- 12. Whittingham, M.S., *Electrical Energy Storage and Intercalation Chemistry*. Science, 1976. **192**(4244): p. 1126-1127.
- 13. Mizushima, K., et al., *LixCoO2* (0<*x*≤1): A new cathode material for batteries of high energy density. Solid State Ionics, 1981. **3-4**: p. 171-174.
- 14. Tarascon, J.M. and M. Armand, *Issues and challenges facing rechargeable lithium batteries*. Nature, 2001. **414**(6861): p. 359-367.

- 15. Scrosati, B. and J. Garche, *Lithium batteries: Status, prospects and future.* Journal of Power Sources, 2010. **195**(9): p. 2419-2430.
- 16. Armand, M. and J.M. Tarascon, *Building better batteries*. Nature, 2008. **451**(7179): p. 652-657.
- 17. Company-, M., Battery 2030: Resilient, sustainable, and circular. 2023.
- 18. Liu, C., Z.G. Neale, and G. Cao, *Understanding electrochemical potentials of cathode materials in rechargeable batteries*. Materials Today, 2016. **19**(2): p. 109-123.
- 19. Goodenough, J.B. and Y. Kim, *Challenges for rechargeable Li batteries.* Chemistry of materials, 2010. **22**(3): p. 587-603.
- 20. Liu, W., et al., Enhancing ionic conductivity in composite polymer electrolytes with well-aligned ceramic nanowires. Nature Energy, 2017. **2**(5): p. 17035.
- 21. Zheng, F., et al., *Review on solid electrolytes for all-solid-state lithium-ion batteries*. Journal of Power Sources, 2018. **389**: p. 198-213.
- 22. Li, M., et al., 30 years of lithium-ion batteries. Advanced Materials, 2018. **30**(33): p. 1800561.
- 23. Lyu, Y., et al., *An Overview on the Advances of LiCoO2 Cathodes for Lithium-Ion Batteries*. Advanced Energy Materials, 2021. **11**(2): p. 2000982.
- 24. Murdock, B.E., K.E. Toghill, and N. Tapia-Ruiz, *A Perspective on the Sustainability of Cathode Materials used in Lithium-Ion Batteries.* Advanced Energy Materials, 2021. **11**(39): p. 2102028.
- 25. Julien, C.M., et al., *Comparative Issues of Cathode Materials for Li-lon Batteries*. Inorganics, 2014. **2**(1): p. 132-154.
- 26. Manthiram, A., *A reflection on lithium-ion battery cathode chemistry.* Nature Communications, 2020. **11**(1): p. 1550.
- 27. M.M. Thackeray, W.I.F.D., P.G. Bruce, and J.B. Goodenough, *Lithium Insertion Into Manganese Spinels*. Mat. Res. Bull., 1983. **Vol. 18**: p. 461-472.
- 28. Chemelewski, K.R., et al., *High-voltage spinel cathodes for lithium-ion batteries: controlling the growth of preferred crystallographic planes through cation doping.* Journal of Materials Chemistry A, 2013. **1**(48): p. 15334-15341.
- 29. Padhi, A., et al., *Effect of Structure on the Fe3 + / Fe2 + Redox Couple in Iron Phosphates.* Journal of The Electrochemical Society, 1997. **144**: p. 1609-1613.
- 30. Manthiram, A., *A reflection on lithium-ion battery cathode chemistry.* Nat Commun, 2020. **11**(1): p. 1550.

- 31. Ohsaki, T., et al., *Overcharge reaction of lithium-ion batteries*. Journal of Power Sources, 2005. **146**(1): p. 97-100.
- 32. Manthiram, A., et al., *Nanostructured electrode materials for electrochemical energy storage and conversion.* Energy & Environmental Science, 2008. **1**(6): p. 621-638.
- 33. Dahn, J.R., U. von Sacken, and C.A. Michal, *Structure and electrochemistry of Li1±yNiO2 and a new Li2NiO2 phase with the Ni (OH)2 structure.* Solid State Ionics, 1990. **44**(1): p. 87-97.
- 34. Wang, L., T. Maxisch, and G. Ceder, *A first-principles approach to studying the thermal stability of oxide cathode materials.* Chemistry of materials, 2007. **19**(3): p. 543-552.
- 35. Liu, H., et al., *Intergranular Cracking as a Major Cause of Long-Term Capacity Fading of Layered Cathodes.* Nano Lett, 2017. **17**(6): p. 3452-3457.
- 36. Zhou, Y.-N., et al., *Tuning charge–discharge induced unit cell breathing in layer-structured cathode materials for lithium-ion batteries.* Nature Communications, 2014. **5**(1): p. 5381.
- 37. Watanabe, S., et al., Capacity fading of LiAlyNi1-x-yCoxO2 cathode for lithium-ion batteries during accelerated calendar and cycle life tests (effect of depth of discharge in charge-discharge cycling on the suppression of the micro-crack generation of LiAlyNi1-x-yCoxO2 particle). Journal of Power Sources, 2014. **260**: p. 50-56.
- 38. Choi, S. and A. Manthiram, Factors Influencing the Layered to Spinel-like Phase Transition in Layered Oxide Cathodes. Journal of The Electrochemical Society, 2002. **149**(9): p. A1157.
- 39. Reimers, J.N., et al., *Synthesis and Electrochemical Studies of LiMnO2 Prepared at Low Temperatures.* Journal of The Electrochemical Society, 1993. **140**(12): p. 3396.
- 40. Delmas, C. and I. Saadoune, *Electrochemical and physical properties of the LixNi1-yCoyO2 phases*. Solid State Ionics, 1992. **53-56**: p. 370-375.
- 41. Rougier, A., et al., *Effect of cobalt substitution on cationic distribution in LiNi1 y CoyO2 electrode materials.* Solid State Ionics, 1996. **90**(1): p. 83-90.
- 42. Li, W. and J.C. Currie, *Morphology Effects on the Electrochemical Performance of LiNi1 x Cox O 2.* Journal of The Electrochemical Society, 1997. **144**(8): p. 2773.
- 43. Yabuuchi, N. and T. Ohzuku, *Novel lithium insertion material of LiCo1/3Ni1/3Mn1/3O2 for advanced lithium-ion batteries.* Journal of Power Sources, 2003. **119-121**: p. 171-174.

- 44. Moses, A.W., et al., *Surface properties of LiCoO2, LiNiO2 and LiNi1- xCoxO2.* Applied surface science, 2007. **253**(10): p. 4782-4791.
- 45. Liu, W., et al., *Nickel-Rich Layered Lithium Transition-Metal Oxide for High-Energy Lithium-Ion Batteries.* Angewandte Chemie International Edition, 2015. **54**(15): p. 4440-4457.
- 46. Booth, S.G., et al., *Perspectives for next generation lithium-ion battery cathode materials.* APL Materials, 2021. **9**(10).
- 47. Song, J., et al., Building Better Full Manganese-Based Cathode Materials for Next-Generation Lithium-Ion Batteries. Electrochemical Energy Reviews, 2023. **6**(1): p. 20.
- 48. Clément, R.J., Z. Lun, and G. Ceder, *Cation-disordered rocksalt transition metal oxides and oxyfluorides for high energy lithium-ion cathodes.* Energy & Environmental Science, 2020. **13**(2): p. 345-373.
- 49. Urban, A., J. Lee, and G. Ceder, *The Configurational Space of Rocksalt-Type Oxides for High-Capacity Lithium Battery Electrodes.* Advanced Energy Materials, 2014. **4**(13): p. 1400478.
- 50. Van der Ven, A., J. Bhattacharya, and A.A. Belak, *Understanding Li Diffusion in Li-Intercalation Compounds*. Accounts of Chemical Research, 2013. **46**(5): p. 1216-1225.
- 51. Kan, W.H., et al., *Understanding the Effect of Local Short-Range Ordering on Lithium Diffusion in Li1.3Nb0.3Mn0.4O2 Single-Crystal Cathode.* Chem, 2018. **4**(9): p. 2108-2123.
- 52. Jones, M.A., et al., *Short-range ordering in a battery electrode, the 'cation-disordered' rocksalt Li1.25Nb0.25Mn0.5O2.* Chemical Communications, 2019. **55**(61): p. 9027-9030.
- 53. Ji, H., et al., *Hidden structural and chemical order controls lithium transport in cation-disordered oxides for rechargeable batteries.* Nature Communications, 2019. **10**(1): p. 592.
- 54. Liu, C., et al., *Advanced Materials for Energy Storage*. Advanced Materials, 2010. **22**(8): p. E28-E62.
- 55. Wang, Y. and G. Cao, *Developments in Nanostructured Cathode Materials for High-Performance Lithium-Ion Batteries*. Advanced Materials, 2008. **20**(12): p. 2251-2269.
- 56. Wright, K., *The Origins and development of ground stone assemblages in Late Pleistocene Southwest Asia.* Paléorient, 1991: p. 19-45.
- 57. Takacs, L., *M. Carey Lea, the first mechanochemist.* Journal of Materials Science, 2004. **39**(16): p. 4987-4993.

- 58. Lea, M.C., Disruption of the silver haloid molecule by mechanical force. American Journal of Science, 1892. **s3-43**(258): p. 527-531.
- 59. (1) Die chemische Literatur und die Organisation der Wissenschaft (2) The Foundations of Chemical Theory (3) Inorganic Chemistry. Nature, 1921. **107**(2698): p. 613-615.
- 60. Šepelák, V., et al., *Mechanochemical reactions and syntheses of oxides.* Chemical Society Reviews, 2013. **42**(18): p. 7507-7520.
- 61. Baláž, P., et al., *Hallmarks of mechanochemistry: from nanoparticles to technology.* Chemical Society Reviews, 2013. **42**(18): p. 7571-7637.
- 62. Kozawa, T., et al., *Effect of ball collision direction on a wet mechanochemical reaction.* Scientific Reports, 2021. **11**(1): p. 210.
- 63. Lee, J., et al., Reversible Mn(2+)/Mn(4+) double redox in lithium-excess cathode materials. Nature, 2018. **556**(7700): p. 185-190.
- 64. Freire, M., et al., *A new active Li-Mn-O compound for high energy density Li-ion batteries.* Nat Mater, 2016. **15**(2): p. 173-7.
- 65. Chen, D., J. Ahn, and G. Chen, *An Overview of Cation-Disordered Lithium-Excess Rocksalt Cathodes*. ACS Energy Letters, 2021. **6**(4): p. 1358-1376.
- 66. Zhang, H., et al., Recent Progress and Perspective of Cation Disordered Rock-salt Material for Advanced Li-ion Batteries. Journal of Materials Chemistry A, 2023.
- 67. Lee, G.-H., et al., *Towards commercialization of fluorinated cation-disordered rock-salt Li-ion cathodes.* Frontiers in Chemistry, 2023. **11**.
- 68. Lee, J., et al., A new class of high capacity cation-disordered oxides for rechargeable lithium batteries: Li–Ni–Ti–Mo oxides. Energy & Environmental Science, 2015. **8**(11): p. 3255-3265.
- 69. Seo, D.H., et al., *The structural and chemical origin of the oxygen redox activity in layered and cation-disordered Li-excess cathode materials.* Nat Chem, 2016. **8**(7): p. 692-7.
- 70. Clément, R.J., et al., Short-range order and unusual modes of nickel redox in a fluorine-substituted disordered rocksalt oxide lithium-ion cathode. Chemistry of Materials, 2018. **30**(19): p. 6945-6956.
- 71. Croguennec, L., et al., Synthesis of "Li1. 1 (Ni0. 425Mn0. 425Co0. 15) 0.9 O1. 8F0. 2" materials by different routes: is there fluorine substitution for oxygen? Journal of the Electrochemical Society, 2009. **156**(5): p. A349.

- 72. Ménétrier, M., et al., *NMR evidence of LiF coating rather than fluorine substitution in Li (Nio. 425Mno. 425Coo. 15)* O2. Journal of Solid State Chemistry, 2008. **181**(12): p. 3303-3307.
- 73. Chen, R., et al., *Li+ intercalation in isostructural Li 2 VO 3 and Li 2 VO 2 F with* O 2- and mixed O 2-/F- anions. Physical Chemistry Chemical Physics, 2015. **17**(26): p. 17288-17295.
- 74. Ren, S., et al., *Improved voltage and cycling for Li+ intercalation in high-capacity disordered oxyfluoride cathodes.* Advanced science, 2015. **2**(10): p. 1500128.
- 75. Lee, J., et al., *Mitigating oxygen loss to improve the cycling performance of high capacity cation-disordered cathode materials.* Nature communications, 2017. **8**(1): p. 981.
- 76. Ouyang, B., et al., Effect of Fluorination on Lithium Transport and Short-Range Order in Disordered-Rocksalt-Type Lithium-Ion Battery Cathodes. Advanced Energy Materials, 2020. **10**(10): p. 1903240.
- 77. Röntgen, W.C., On a new kind of rays. Science, 1896. **3**(59): p. 227-231.
- 78. Phillips, G., *XRayView: a teaching aid for X-ray crystallography.* Biophysical journal, 1995. **69**(4): p. 1281-1283.
- 79. Dinnebier, R. and S. Billinge, *Overview and principles of powder diffraction*. 2019.
- 80. Månsson, M. and J. Sugiyama, *Muon-spin relaxation study on Li- and Nadiffusion in solids*. Physica Scripta, 2013. **88**(6): p. 068509.
- 81. Blundell, S., *Spin-polarized muons in condensed matter physics.* Contemporary Physics, 1999. **40**(3): p. 175-192.
- 82. McClelland, I., et al., *Muon spectroscopy for investigating diffusion in energy storage materials.* Annual Review of Materials Research, 2020. **50**: p. 371-393.
- 83. Abdollahifar, M., et al., *Insights into Influencing Electrode Calendering on the Battery Performance*. Advanced Energy Materials, 2023: p. 2300973.
- 84. Primo, E.N., M. Touzin, and A.A. Franco, Calendering of Li (Nio. 33Mno. 33Coo. 33) O2-based cathodes: analyzing the link between process parameters and electrode properties by advanced statistics. Batteries & Supercaps, 2021. **4**(5): p. 834-844.
- 85. Paterson, A.J., A.R. Armstrong, and P.G. Bruce, *Stoichiometric LiMnO2 with a Layered Structure: Charge/Discharge Capacity and the Influence of Grinding.*Journal of the Electrochemical Society, 2004. **151**(10): p. A1552.

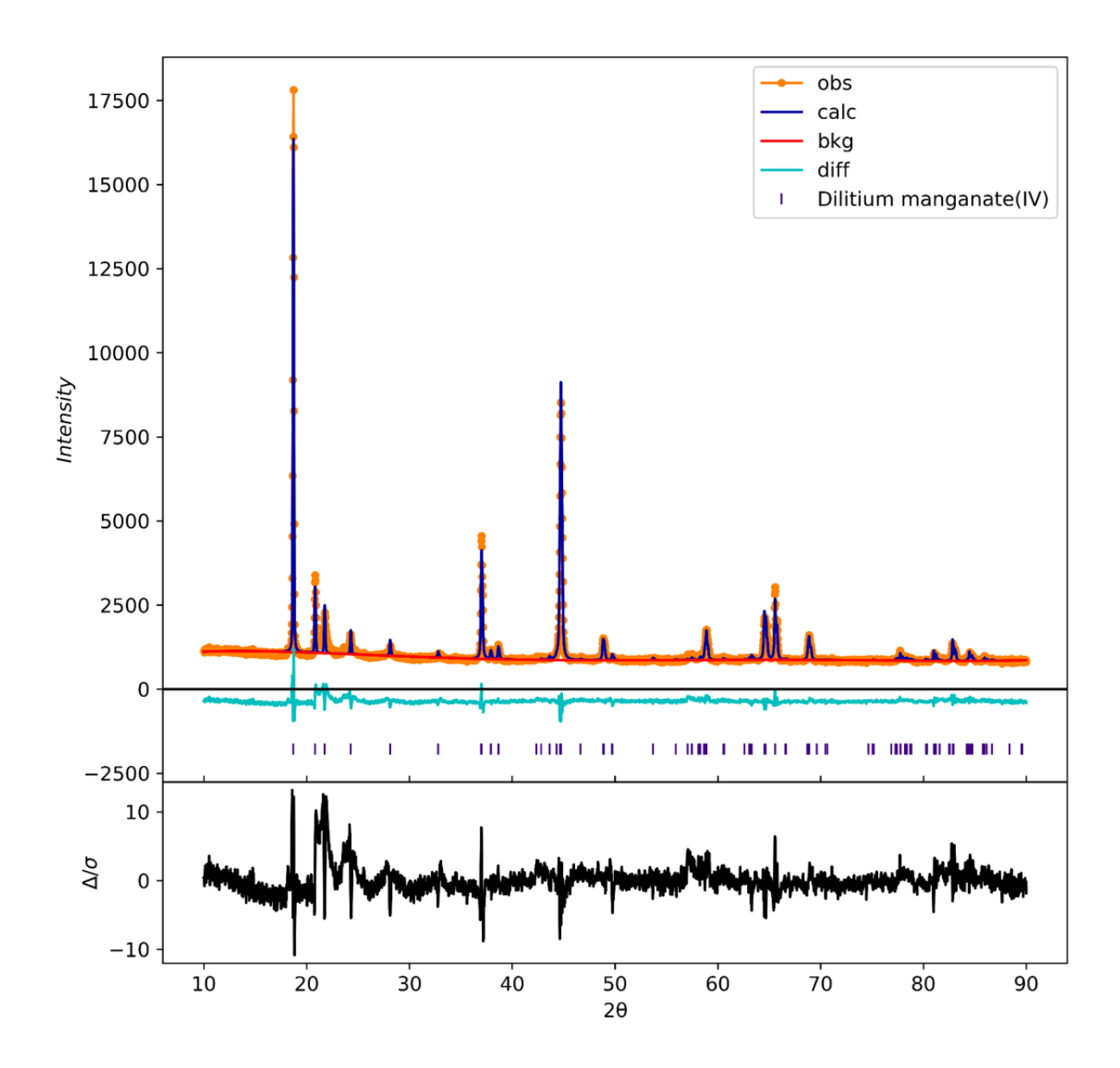
- 86. Reed, J., G. Ceder, and A. Van Der Ven, *Layered-to-spinel phase transition in Li x MnO2*. Electrochemical and Solid-State Letters, 2001. **4**(6): p. A78.
- 87. Robertson, A.D. and P.G. Bruce, *Mechanism of Electrochemical Activity in Li2MnO3*. Chemistry of Materials, 2003. **15**(10): p. 1984-1992.
- 88. Rossouw, M. and M. Thackeray, *Lithium manganese oxides from Li2MnO3 for rechargeable lithium battery applications.* Materials research bulletin, 1991. **26**(6): p. 463-473.
- 89. Li, M., et al., *Cationic and anionic redox in lithium-ion based batteries.* Chemical Society Reviews, 2020. **49**(6): p. 1688-1705.
- 90. Gou, X., et al., In Situ Surface Self-Reconstruction Strategies in Li-Rich Mn-Based Layered Cathodes for Energy-Dense Li-Ion Batteries. Advanced Functional Materials, 2022. **32**(18): p. 2112088.
- 91. Kim, S.-W., et al., Structure stabilization by mixed anions in oxyfluoride cathodes for high-energy lithium batteries. ACS nano, 2015. **9**(10): p. 10076-10084.
- 92. Jiang, Y.-s., et al., Surface modification by fluorine doping to increase discharge capacity of Li 1.2 Ni 0.2 Mn 0.6 O 2 cathode materials. Ionics, 2020. **26**: p. 151-161.
- 93. Lee, J., et al., Reversible Mn2+/Mn4+ double redox in lithium-excess cathode materials. Nature, 2018. **556**(7700): p. 185-190.
- 94. House, R.A., et al., *Lithium manganese oxyfluoride as a new cathode material exhibiting oxygen redox.* Energy & Environmental Science, 2018. **11**(4): p. 926-932.
- 95. Ji, H., et al., *Ultrahigh power and energy density in partially ordered lithium-ion cathode materials.* Nature Energy, 2020. **5**(3): p. 213-221.
- 96. Lun, Z., et al., Design principles for high-capacity Mn-based cation-disordered rocksalt cathodes. Chem, 2020. **6**(1): p. 153-168.
- 97. Matsunaga, T., et al., *Dependence of Structural Defects in Li2MnO3 on Synthesis Temperature.* Chemistry of Materials, 2016. **28**(12): p. 4143-4150.
- 98. Diaz-Lopez, M., et al., Reversible densification in nano-Li2MnO3 cation disordered rock-salt Li-ion battery cathodes. Journal of Materials Chemistry A, 2020. **8**(21): p. 10998-11010.
- 99. Hausbrand, R., et al., Fundamental degradation mechanisms of layered oxide Li-ion battery cathode materials: Methodology, insights and novel approaches. Materials Science and Engineering: B, 2015. **192**: p. 3-25.

- 100. Rana, J., et al., *Quantifying the capacity contributions during activation of Li2MnO3*. ACS Energy Letters, 2020. **5**(2): p. 634-641.
- Blundell, K.M., S. Rawlings, and C.J. Willott, The nature and evolution of classical double radio sources from complete samples. The Astronomical Journal, 1999. 117(2): p. 677.
- 102. Johnston, B.I.J., et al., *Elucidating local diffusion dynamics in nickel-rich layered oxide cathodes*. Physical Chemistry Chemical Physics, 2023. **25**(37): p. 25728-25733.
- 103. McClelland, I., et al., *Muon Spectroscopy for Investigating Diffusion in Energy Storage Materials*. Annual Review of Materials Research, 2020. **50**(1): p. 371-393.
- 104. Lun, Z., et al., *Improved cycling performance of Li-excess cation-disordered cathode materials upon fluorine substitution.* Advanced Energy Materials, 2019. **9**(2): p. 1802959.
- 105. Nitta, N. and G. Yushin, *High-capacity anode materials for lithium-ion batteries:* choice of elements and structures for active particles. Particle & Particle Systems Characterization, 2014. **31**(3): p. 317-336.
- 106. Armand, M., et al., *Lithium-ion batteries–Current state of the art and anticipated developments*. Journal of Power Sources, 2020. **479**: p. 228708.
- 107. Weiss, M., et al., Fast charging of lithium-ion batteries: a review of materials aspects. Advanced Energy Materials, 2021. **11**(33): p. 2101126.
- 108. Chen, D., W.H. Kan, and G. Chen, *Understanding performance degradation in cation-disordered rock-salt oxide cathodes*. Advanced Energy Materials, 2019. **9**(31): p. 1901255.
- 109. Geng, F., et al., Anionic redox reactions and structural degradation in a cation-disordered rock-salt Li 1.2 Ti 0.4 Mn 0.4 O 2 cathode material revealed by solid-state NMR and EPR. Journal of Materials Chemistry A, 2020. **8**(32): p. 16515-16526.
- 110. Zheng, Y., et al., Effects of Ball Milling Processes on the Microstructure and Rheological Properties of Microcrystalline Cellulose as a Sustainable Polymer Additive. Materials (Basel), 2018. **11**(7).
- 111. Cuccu, F., et al., *Mechanochemistry: new tools to navigate the uncharted territory of "impossible" reactions.* ChemSusChem, 2022. **15**(17): p. e202200362.
- 112. Çuvalcı, O., et al., Effect of ball mill time and wet pre-milling on the fabrication of Ti powders by recycling Ti machining chips by planetary milling. Powder Technology, 2023. **426**: p. 118637.

- 113. Zhi, X. and A.R. West, *Mechanosynthesis of Disordered Rock Salt Structures: Thermodynamic and Kinetic Considerations.* Chemistry of Materials, 2023. **35**(17): p. 6790-6798.
- 114. Do, J.-L. and T. Friščić, *Mechanochemistry: A Force of Synthesis.* ACS Central Science, 2017. **3**(1): p. 13-19.
- 115. Freire, M., et al., *Nanostructured Li2MnO3: a disordered rock salt type structure for high energy density Li ion batteries.* Journal of Materials Chemistry A, 2017. **5**(41): p. 21898-21902.
- 116. Chung, H., et al., Experimental considerations to study Li-excess disordered rock salt cathode materials. Journal of Materials Chemistry A, 2021. **9**(3): p. 1720-1732.
- 117. Hong, S.-B., et al., *All-Solid-State Lithium Batteries: Li+-Conducting Ionomer Binder for Dry-Processed Composite Cathodes.* ACS Energy Letters, 2022. **7**(3): p. 1092-1100.
- Zhan, C., et al., Dissolution, migration, and deposition of transition metal ions in Li-ion batteries exemplified by Mn-based cathodes—a critical review. Energy & Environmental Science, 2018. 11(2): p. 243-257.
- 119. Richards, W.D., et al., Fluorination of lithium-excess transition metal oxide cathode materials. Advanced Energy Materials, 2018. **8**(5): p. 1701533.
- 120. Luo, M., et al., *Identifying the anionic redox activity in cation-disordered Li 1.25 Nb 0.25 Fe 0.50 O 2/C oxide cathodes for Li-ion batteries.* Journal of Materials Chemistry A, 2020. **8**(10): p. 5115-5127.
- 121. Urban, A., et al., *Electronic-structure origin of cation disorder in transition-metal oxides.* Physical review letters, 2017. **119**(17): p. 176402.
- 122. Taylor, Z.N., et al., Stabilization of O–O Bonds by d0 Cations in Li4+xNi1-xWO6 (0 $\le x \le 0.25$) Rock Salt Oxides as the Origin of Large Voltage Hysteresis. Journal of the American Chemical Society, 2019. **141**(18): p. 7333-7346.

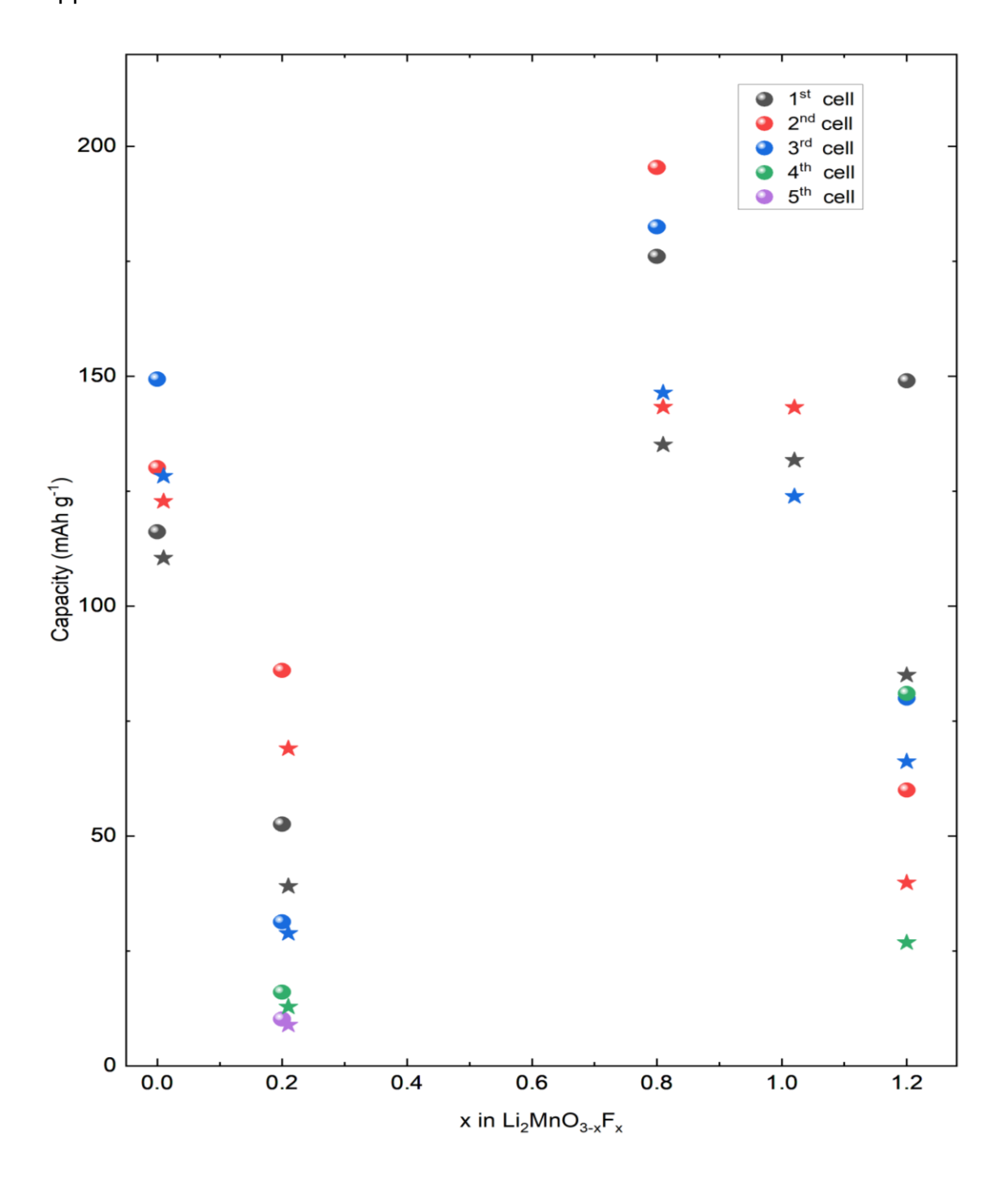
8. Appendices

Appendix 3.1



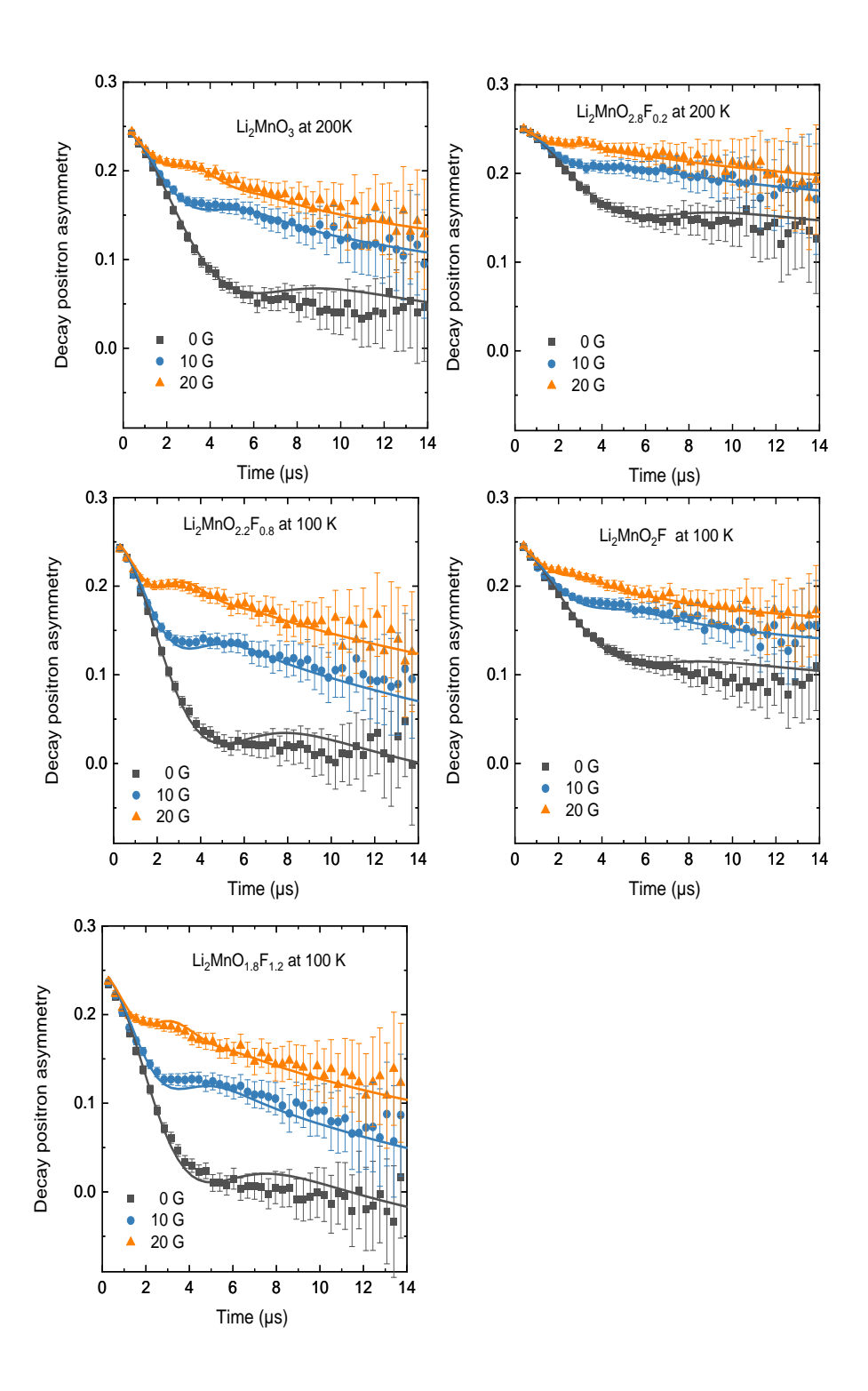
Rietveld analysis of LMO- 1000 °C product obtained at 1000 °C after 48 hours.

Appendix 3.2:



The initial charge- discharge capacities for x in Li₂MnO_{3-x}F_x (where x is x=0 represent Li₂MnO₃; x=0.2 represent Li₂MnO_{2.8}F_{0.2}; x=0.8 represent Li₂MnO_{2.2}F_{0.8}; x=1 represent Li₂MnO₂F; x=1.2 represent Li₂MnO_{1.8}F_{1.2}. The colours indicate how many coin cells were prepared for each sample. The round shape in each colour represents the initial charge capacity results, while the star shape in each colour represents the first discharge capacity results. All 2032-coin type cells were cycled between 2 – 4.8 V vs. Li/Li⁺ at a rate of 1 C.

Appendix 3.3:



The raw data for the μ^+ -SR measurement shows the time evolution of the decay positron asymmetry under zero field 0 Gauss (black), longitudinal fields of 10 Gauss (blue), and 20 Gauss (orange) for (a) Li₂MnO₃ at 200 K (b) Li₂MnO_{2.8}F_{0.2} at 200 K (c) Li₂MnO_{2.2}F_{0.8} at 100 K, (d) Li₂MnO₂F at 100 K, and (e) Li₂MnO_{1.8}F_{1.2} at 100 K.